IONOSPHERIC DELAY CORRECTION FOR SINGLE-FREQUENCY GPS RECEIVERS

Damien J. Allain
A thesis submitted for the degree of Doctor of Philosophy
University of Bath
Department of Electronic and Electrical Engineering
July 2009

COPYRIGHT

Damien J. Allain

---

[1] as per University of Bath Ordinance 22.3(c): `http://www.bath.ac.uk/ordinances/22.pdf`

[2] e.g. for the purposes of an examination, as per the Copyright, Designs and Patents Act 1988 (c. 48) §32(3): `http://www.opsi.gov.uk/acts/acts1988/ukpga_19880048_en_3#pt1-ch3-pb3`

Contents

List of Figures and Tables

Acknowledgements

This work used data made widely available by the IGS, EUREF, UNAVCO and NGDC. I acknowledge the financial support from the EPSRC.

I would like to thank my supervisors, Professor Cathryn N Mitchell and Professor Andrew D Brown for their wide ranging support during this project. I am grateful to Dr Bettina Zapfe, Dr Robert Meggs and to my supervisors for their help and advice in writing and proof-reading this thesis or the transfer report on which a large part of this thesis is based. The help I received from Dr Paul Spencer, Duncan Hodges and Matthew Foster in using the computing resources made available to me and their advice, especially as I settled in and as I started writing, saved me valuable time. I deeply appreciate the welcome and knowledge I received from my other colleagues, mainly from the Invert group, in particular inputs on the ionosphere from Dr Ping Yin and Zama Katamzi, on electronics from Dr Robert Watson and on mathematics from Dr Manucher Solemani, Dr Nathan Smith and Dr Adrian Evans. I also completed my PhD thanks to the emotional support and advice from my friends, especially fellow members of Christian societies of the University of Bath, and from my family, especially my parents and above all my wife Anne-Laure.

Abstract

The majority of navigation satellite receivers operate on a single frequency and experience an error due to the ionospheric delay. They compensate for the ionospheric delay using an ionospheric model which typically only corrects for 50% of the delay. An alternative approach is to map the ionosphere with a network of real-time measurements, with either a thin shell approximation or a full 3D map. Here, a time-dependent 3D tomographic imaging technique is used to map the free electron density over the full-height of the ionosphere during solar maximum. The navigation solutions computed using corrections based upon models and thin-shell and full-height maps are compared in this project.

The models and maps are used to calculate the excess propagation delay on the L1 frequency experienced by GPS receivers at selected locations across Europe and North America. The excess delay is applied to correct the pseudo-range single frequency observations at each location and the improvements to the resulting positioning are calculated. It is shown that the thin-shell and full-height maps perform almost as well as a dual-frequency carrier-smoothed benchmark and for most receivers better than the unfiltered dual-frequency benchmark. It is also shown that the unfiltered dual-frequency method is not reliable, which is of concern as it is a proposed upgrade to current positioning systems. The improvements in positioning accuracy vary from day to day depending on ionospheric conditions but can be up to 25 m during mid-day at solar maximum conditions at European mid-latitudes. The full-height corrections perform well under all geomagnetic conditions and are considerably better than thin-shell corrections under extreme storm conditions.

The transmission of the navigation correction requires a forecast, an image compression and a system of distribution across a local region. The feasibility of this is demonstrated for regions of land and near-land coastal regions across Europe.

Acronyms

MART	Multiplicative Algebraic Reconstruction Technique
CODE	Center for Orbit Determination in Europe
DCT	Discrete Cosine Transform
ED	Free Electrons Density
DIT	Discrete Inverse Theory
DOP	Dilution Of Precision
PDOP	Positioning DOP
TDOP	Time DOP
ECEF	Earth-Centred Earth-Fixed
ECI	Earth-Centred Inertial
EGNOS	European Geostationary Navigation Overlay System
EUV	Extreme Ultra-Violet
EOF	Empirical Orthogonal Function
GNSS	Global Navigation Satellite System
GPS	Global Positioning System
IDA3D	Ionospheric Data Assimilation 3D
IGS	International GNSS Service
ISR	Incoherent Scatter Radar
EISCAT	European Incoherent Scatter Radar
IRI	International Reference Ionosphere
JPEG	Joint Photographic Experts Group
LEO	Low Earth Orbit
MIDAS	Multi Instrument Data Analysis System
MSAS	Multi-functional Satellite Augmentation System
NNSS	Navy Navigational Satellite System
NPL	National Physics Laboratory
PAN	Performance Analysis Report
QP	Quadratic Programming
RINEX	Receiver Independent Exchange Format

RMS	Root Mean Square
SBAS	Satellite Based Augmentation System
SD	Standard Deviation
SVD	Singular Values Decomposition
TDOA	Time-Difference-Of-Arrival
TEC	Total Electron Concentration
TECU	TEC Unit ($10^{16}\,\mathrm{m}^{-2}$)
STEC	Slant TEC
VTEC	Vertical TEC
TOA	Time-Of-Arrival
WAAS	Wide Area Augmentation System

Symbols and notations

Symbols

$\dot{x}$	Time derivative of x, i.e $\dot{x} \equiv \mathrm{d}x/\,\mathrm{d}t$
$\lvert x \rvert$	Absolute value or modulus of x
$\overrightarrow{x}, x, \widehat{x}$	Geometrical vector. The notations without an arrow above is equivalent to the modulus of the vector, i.e. $x \equiv \left\lvert \overrightarrow{x} \right\rvert$. With a hat above, this becomes the unit vector, i.e. $x\,\widehat{x} = \overrightarrow{x}$.
$A, \overrightarrow{A}, AB, \overrightarrow{AB}$	For points, capital letters are used (although, as shown below, capital letters can also be used for values). With an arrow above, this becomes the position vector of the point. Therefore, without an arrow above, this can also be the modulus of the position vector, as explained above. When two capital letters are side by side, this is the start and end of the vector or, as explained above, length.
$\left(\widehat{\overrightarrow{x}\,;\,\overrightarrow{y}}\right)$	Angles, e.g. $\overrightarrow{x} \cdot \overrightarrow{y} = x \times y \times \cos\left(\widehat{\overrightarrow{x}\,;\,\overrightarrow{y}}\right)$.
$\mathbf{A}, \boldsymbol{\alpha}$	Matrices are in bold upper case; column vectors in bold lower case.
Δx	error or uncertainty on x

Notations

$\mathbf{A}$	matrix of the dl
$\mathbf{b}$	vector of the TEC measurements
C	molecular concentration
c	speed of light in vacuum (299 796 458 $m\ s^{-1}$)
$\Delta_\theta^{n,f} t$	ambiguity on the phase pseudorange with satellite n on frequency f
$\Delta_r t$	receiver clock bias
$\Delta_s t$	satellite clock bias
$\Delta_s^r t$	satellite clock bias due to relativistic effect coming from the ellipticity of its orbit
$\Delta_s' t$	satellite-specific clock bias
$\Delta_r^{1\rightarrow 2} p$	P1-P2 bias of the receiver
$\Delta_s^{1\rightarrow 2} p$	P1-P2 bias of the satellite
$\mathbf{D}$	positioning covariance matrix

D_X, D_Y, D_Z, D_T, D_P	respectively : XDOP, YDOP, ZDOP, TDOP, PDOP
$\mathrm{d}l$	path element or path-to-voxel intersection
ϵ_0	free space permittivity
ϵ	negligible quantities
ϵ_f	noise on the pseudorange measured with the signal on frequency f
f_n	frequency of signal [n]
g	gravitational acceleration
$\mathbf{G}$	matrix of the geometry of the satellite constellation
h	altitude
η	number of EOFs
i, j, m, n	numbers and indexes
I	ionospheric delay term
k	wave number
N, N'	ED, respectively measured and calculated
$\int Ndl, \int N'dl$	TEC, respectively measured and calculated
n	refractive index
n'	relative refractive index
Ω	rotation of the Earth
ω	angular frequency
ϕ	elevation angle
p	pressure
P_n^*	absolute pseudorange between the satellite [n] and the receiver
P_0	ionosphere-free pseudorange
P_0'	ionosphere-corrected pseudorange
P_n^θ	phase pseudorange measured with the signal on frequency f_n
P_0^θ	ionosphere-free phase pseudorange
P_1, P_2	P1 and P2 code observations
R	position of the receiver
$\overrightarrow{\dot{R}_I}, \dot{R}_I$	receiver velocity and speed in the ECI frame
ρ	volumic mass
r_n	range between the satellite [n] and the receiver
r'	geometric range between the satellite and the receiver
r_s	Sagnac effect
S	position of the satellite antenna
S'	position of the centre of mass of the satellite
$\Delta_v S$	vertical component of the antenna offset
$T_{\phi,h}$	tropospheric delay for a receiver at altitude h viewing a satellite at elevation angle ϕ
t_n	signal travel time between the satellite [n] and the receiver
t_s	time of signal transmission
t_r	time of signal reception
v	signal speed
$\mathbf{w}$	vector of weighting coefficients

$\mathbf{X}$	mapping matrix
$\mathbf{x}$	vector of all the N
x, y, z	Cartesian coordinates of the receiver
X_n, Y_n, Z_n	Cartesian coordinates of the satellite or transmitter $[n]$

Chapter 1

Introduction

The Global Positioning System (GPS) and other Global Navigation Satellite Systems (GNSSs) enable the precise measurement of a position anywhere on the Earth. The systems are based upon knowledge of the time of flight of electromagnetic waves that at a first approximation travel through a vacuum. However, the Earth's atmosphere adds some delay to the signal travel times and the largest component of this delay comes from the ionosphere.

There are a number of different ways that the ionospheric delay can be compensated for. Sophisticated surveying receivers, that operate on at least two frequencies, can measure and compensate precisely for the ionospheric delay. The vast majority of navigation receivers still operate on a single frequency and do not compensate precisely for the ionospheric delay, causing an uncertainty in the positioning. The error components due to the ionosphere usually vary little over periods of time of a few minutes and over distances of a few kilometres and some users of GNSS receivers will have the illusion of a precise position. However, users who require a consistent positioning throughout the day and from one day to the next or who require an accurate positioning relative to a survey site must take this uncertainty into account.

The overall aim of this project is to use real-time maps of the ionosphere to compensate for the ionospheric delay and hence to improve the accuracy of GPS positioning. The principles of GPS positioning and the origin of its errors are presented in Chapter 2. A 4D imaging method to compensate precisely for the ionospheric delay with a forecast, tested in this project, is explained in Chapter 3, alongside other methods used as benchmark or references.

The algorithms to calculate the position of a GPS receiver as well as the data processing choices behind the analysis are detailed in Chapter 4. To make the forecast usable, it must be broadcast to the user and therefore compressed, as explained in Chapter 5. The proposed 4D imaging method has been compared to models in Chapter 6 for Europe. In Chapter 7 another simpler mapping approach is also compared to the 4D imaging and to models for the North America region. The results are summarised and their overall implications discussed in Chapter 8.

Chapter 2

GNSS positioning

The Global Navigation Satellite Systems (GNSSs) are designed to provide positioning anywhere on Earth at any time. They are based on a relatively simple method known as “pseudorange positioning”, but the factors that affect it and the systems that complement it are extensive. There are several GNSSs : the American Global Positioning System (GPS) and the Russian GLONASS are currently operational, and the Europeans are setting up GALILEO. Out of all these, the GPS is still by far the most popular and the one for which the largest amount of observations are available, so will be the one mainly detailed here. The aim of this Chapter is to briefly explain the pseudorange positioning method in Section 2.1 and to focus on the related factors and systems relevant to this project in Section 2.2.

2.1 Three-Dimensional pseudorange positioning

This section is based on Kaplan et al. (1996) and on Allain (2005).

GPS uses Time-Difference-Of-Arrival (TDOA) ranging with a constant offset. The satellites give information about the time of transmission of the signals they send. The signal travels the distance r between the satellite and the receiver at a velocity v and reaches the receiver after a time t :

$$r = v\,t \tag{2.1}$$

A receiver with a clock synchronised to GPS time could measure the difference t between the time of transmission, from the information contained in the signal, and the time of reception, from the receiver clock, and calculate the distance r. The signal velocity v is assumed to be approximately equal to c, the speed of light in vacuum.

Receivers use the signals of several transmitters to solve for a position as is explained in the following paragraphs.

2.1.1 Introduction with the Two-Dimensional solution

Using the signal from two transmitters, the receiver position can be found by solving the following system of equations:

$$\begin{cases} r_1^2 = (v\ t_1)^2 = (X_1 - x)^2 + (Y_1 - y)^2 \\ r_2^2 = (v\ t_2)^2 = (X_2 - x)^2 + (Y_2 - y)^2 \end{cases} \tag{2.2}$$

using the known variables: r_n the range measured for transmitter n with v the signal travel velocity and t_n the signal travel time, X_n and Y_n transmitter n's co-ordinates, and the two unknowns: x and y, the receiver's position in Cartesian coordinates.

Solving the above equation is the equivalent of finding the intersection of two circles, as shown in Figure 2.1. Both Equation (2.2) and the intersection of two circles give two solutions. With approximate knowledge of the position of the receiver, the most unlikely position can be discarded.

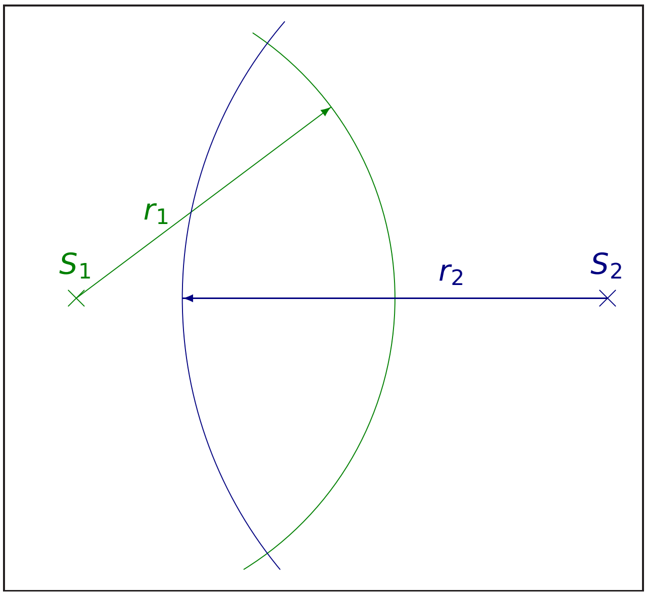

Figure 2.1: Geometric solution of 2D range positioning.
A receiver can measure the distances r_1 and r_2 to two transmitters S_1 and S_2 at known positions, (X_1, Y_1) and (X_2, Y_2) respectively, to determine its position.

The signal travel time can be directly measured, e.g. from the time difference between the transmission of a signal and the response from a transponder. This method however limits the number of users. The signal travel time can also be measured by taking the difference between the transmission time and the reception time: this is called Time-Of-Arrival (TOA). Range positioning with TOA ranging requires that the receiver clock is synchronised with the transmitter clocks. If the receiver clock shows a bias of $\Delta_r t$, the measurement of the range will be affected by $\Delta r = v\Delta_r t$. Since $v \approx c = 299\,796\,458\,\mathrm{m\,s^{-1}}$ a clock error of only $\Delta_r t = 1\,\mu s$ will induce a ranging error of almost $\Delta r \simeq 300\,\mathrm{m}$. Only atomic clocks, that deviate only by a few nanoseconds, are accurate enough to carry out TOA range positioning with electromagnetic waves to a sufficient precision. This can be and has been implemented but only few users can carry or afford a heavy and extremely expensive atomic clock.

As an alternative, receivers with less accurate clocks can be used with range measurements that have errors from the receiver clock. In this case a modified procedure is adopted whereby the reception time is calculated simultaneously with the position. A pseudorange is the distance calculated by subtracting the reception time from the transmission time, both of which have a bias, and multiplying this difference by the signal velocity. All the measured travel times are offset by the same amount $v\,\Delta_r t$, with v the signal velocity and $\Delta_r t$ the receiver clock deviation, making the range measurements pseudoranges.

The signal from one extra transmitter is used to compensate for the extra unknown and the receiver's position is found by solving the following system of equations:

$$\begin{cases} \left(P_1^* - v\,\Delta_r t\right)^2 = \left(v\,(t_1 - \Delta_r t)\right)^2 = (X_1 - x)^2 + (Y_1 - y)^2 \\ \left(P_2^* - v\,\Delta_r t\right)^2 = \left(v\,(t_2 - \Delta_r t)\right)^2 = (X_2 - x)^2 + (Y_2 - y)^2 \\ \left(P_3^* - v\,\Delta_r t\right)^2 = \left(v\,(t_3 - \Delta_r t)\right)^2 = (X_3 - x)^2 + (Y_3 - y)^2 \end{cases} \tag{2.3}$$

using the known variables: P_n^* the absolute pseudorange measured for transmitter n with v the signal travel speed and t_n the signal travel time, X_n and Y_n transmitter n's coordinates, and the three unknowns: x and y, the receiver's position in Cartesian coordinates, and $\Delta_r t$, the receiver clock bias.

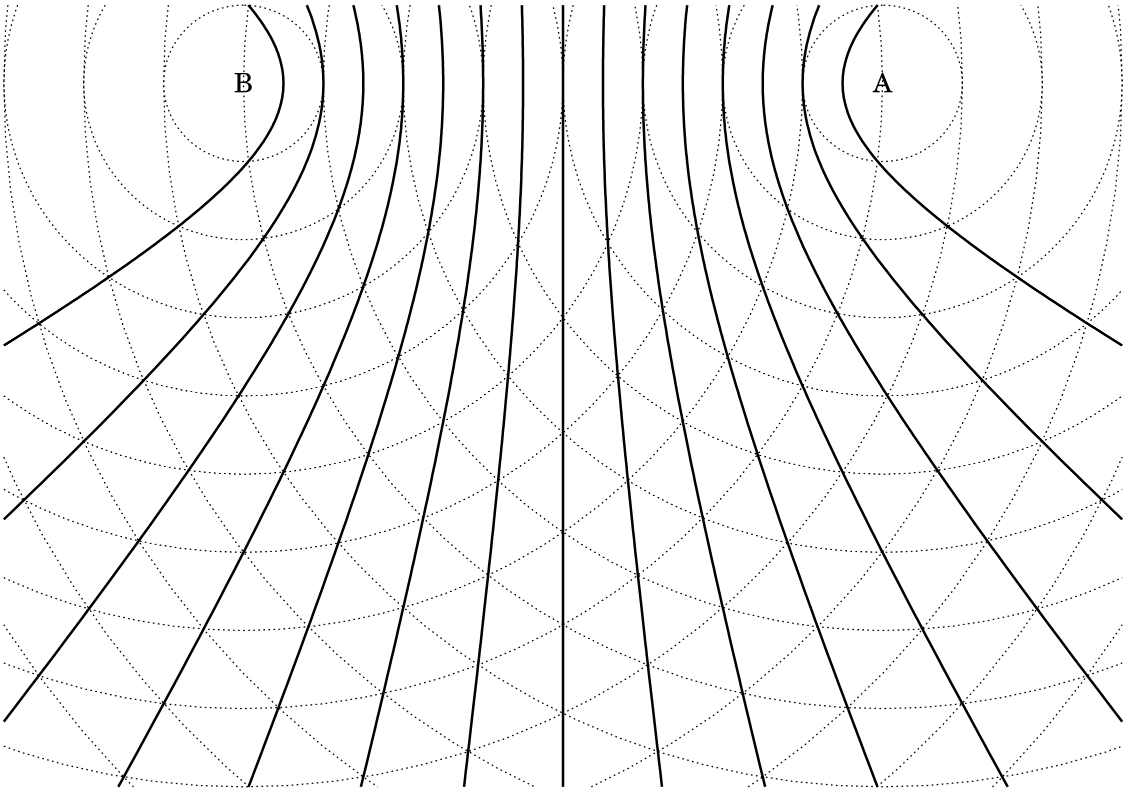

Figure 2.2: Hyperbolae are lines made of the points that are closer by a constant distance to one point than to another.

An alternative way of understanding pseudoranging can be reached by using a geometric solution. In Figure 2.2 the dotted circles show the lines of constant distance from the transmitter. The solid lines mark out the hyperbolae of constant differences in distance between the two transmitters. To view a specific example, in Figure 2.3 the red hyperbola shows the points that are two units closer to C than B. Three hyperbolae, that intersect in one point in 2D, can be computed from three pseudoranges as shown in Figure 2.3.

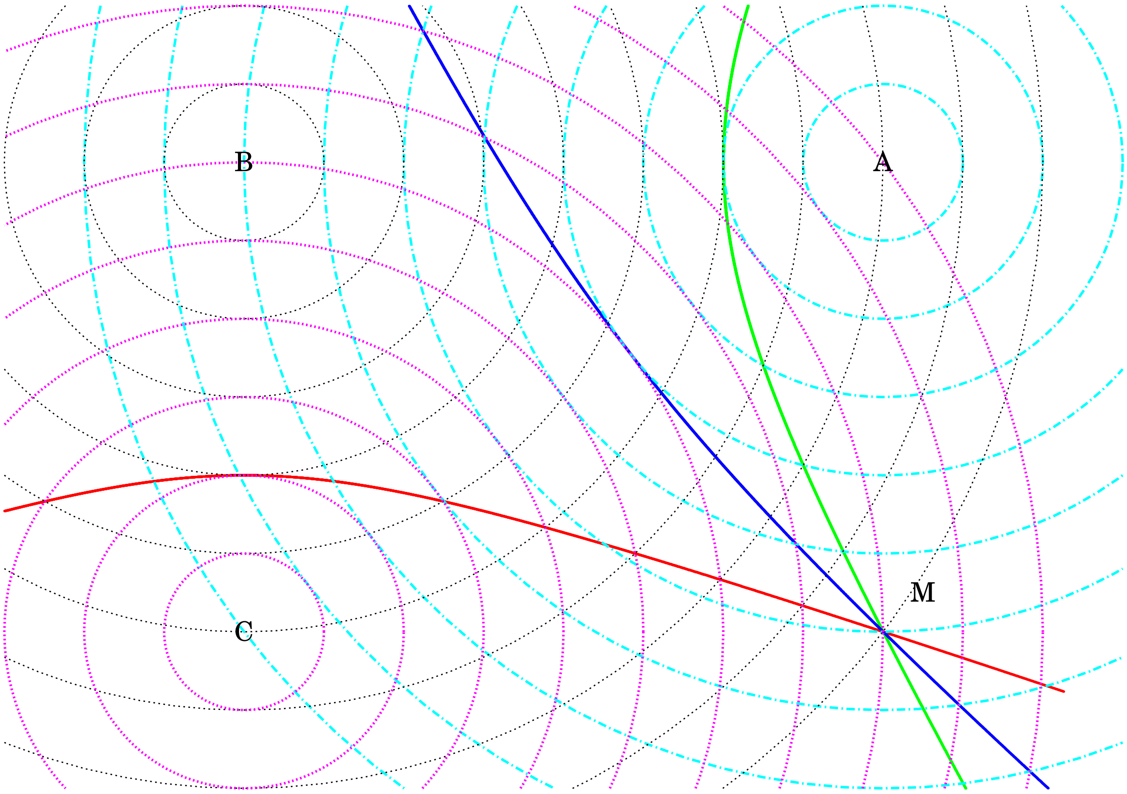

Figure 2.3: Geometric solution of 2D pseudorange.
Consecutive concentric circles are separated by 1 unit.
The red hyperbola joins intersections of circles centred on B (black) and C (magenta) and its points are 2 units closer to C than to B. The green hyperbola joins intersections of circles centred on A (cyan) and B and its points are four units closer to A. The blue hyperbola joins intersections of circles centred on A and C and its points are two units closer to A.

2.1.2 Progression to Three Dimensions

In 3D, a ranging receiver's position is found by ranging with three transmitters. Equation (2.2) then becomes:

$$\begin{cases} r_1^2 = (v\ t_1)^2 = (X_1 - x)^2 + (Y_1 - y)^2 + (Z_1 - z)^2 \\ r_2^2 = (v\ t_2)^2 = (X_2 - x)^2 + (Y_2 - y)^2 + (Z_2 - z)^2 \\ r_3^2 = (v\ t_3)^2 = (X_3 - x)^2 + (Y_3 - y)^2 + (Z_3 - z)^2 \end{cases} \tag{2.4}$$

In 3D, the circles become spheres and the three spheres intersect again at two points, the least likely of which is again discarded.

In 3D, a pseudorange receiver's position is found by using the signals from at least four transmitters. Equation (2.3) then becomes :

$$\begin{cases} \left(P_1^* - v\ \Delta_r t\right)^2 = (v\,(t_1 - \Delta t))^2 = (X_1 - x)^2 + (Y_1 - y)^2 + (Z_1 - y)^2 \\ \left(P_2^* - v\ \Delta_r t\right)^2 = (v\,(t_2 - \Delta t))^2 = (X_2 - x)^2 + (Y_2 - y)^2 + (Z_2 - y)^2 \\ \left(P_3^* - v\ \Delta_r t\right)^2 = (v\,(t_3 - \Delta t))^2 = (X_3 - x)^2 + (Y_3 - y)^2 + (Z_3 - y)^2 \\ \left(P_4^* - v\ \Delta_r t\right)^2 = (v\,(t_4 - \Delta t))^2 = (X_4 - x)^2 + (Y_4 - y)^2 + (Z_4 - y)^2 \end{cases} \tag{2.5}$$

using the known variables : P_n^* the pseudorange measured for transmitter n, X_n, Y_n and Z_n transmitter n's coordinates, v the signal travel speed and the four unknowns : $\Delta_r t$ the receiver clock deviation and x, y and z the Cartesian coordinates of the receiver's position. Equation (2.5) shows a component of the bias that is equal on all the pseudoranges P_n^* will affect only the value of t and not the values of neither x, y nor z at all.

In 3D, the hyperbolae become hyperboloids (shaped almost like a cone with a rounded top) and the three hyperboloids intersect in a conic curve : an ellipse, a parabola or again a hyperbola. Another transmitter is therefore necessary in order to calculate at least one other hyperboloid that will intersect the conic in one point or possibly two if the conic is an ellipse.

2.1.3 Least squares solution

The following section draws from material found in Parkinson (1996).

Typically more than four satellites are visible to a receiver. In this case a least square fit of the solution is appropriate. For $n \geq 4$ satellites, taking a receiver of position R and a satellite of position S_i, with $RS_i \equiv r_i$ and $1 \leq i \leq n$, the absolute pseudorange P_i^* is :

$$P_i^* = v\Delta_r t + r_i \tag{2.6}$$

Rewriting r_i with $\overrightarrow{r_i}$ the receiver to satellite vector, $\widehat{r_i}$ its unit vector and $\overrightarrow{S_i}$ and $\overrightarrow{R}$ the position vectors of the satellite and the receiver respectively :

$$r_i = \widehat{r_i} \cdot \overrightarrow{r_i} = \widehat{r_i} \cdot \left(\overrightarrow{S_i} - \overrightarrow{R}\right) = \widehat{r_i} \cdot \overrightarrow{S_i} - \widehat{r_i} \cdot \overrightarrow{R} \tag{2.7}$$

gives, from (2.6) and (2.7) :

$$P_i^* = v\Delta_r t + \widehat{r_i} \cdot \overrightarrow{S_i} - \widehat{r_i} \cdot \overrightarrow{R} \tag{2.8a}$$

$$\widehat{r_i} \cdot \overrightarrow{R} - v\Delta_r t = \widehat{r_i} \cdot \overrightarrow{S_i} - P_i^* \tag{2.8b}$$

Taking $u_{r_i}^x$, $u_{r_i}^y$ and $u_{r_i}^z$ the components of $\widehat{r_i}$ gives **G** the matrix of the geometry of the constellation:

$$\mathbf{G} = \begin{pmatrix} u^x_{r_1} & u^y_{r_1} & u^z_{r_1} & -1 \\ \vdots & \vdots & \vdots & \vdots \\ u^x_{r_n} & u^y_{r_n} & u^z_{r_n} & -1 \end{pmatrix} \tag{2.9}$$

and the matrix notation of Equation (2.8b):

$$\mathbf{G} \begin{pmatrix} x \\ y \\ z \\ v\Delta_r t \end{pmatrix} = \begin{pmatrix} \widehat{r_1} \cdot \overrightarrow{S_1} - P^*_1 \\ \vdots \\ \widehat{r_n} \cdot \overrightarrow{S_n} - P^*_n \end{pmatrix} \tag{2.10}$$

Taking $(\mathbf{G}^T\mathbf{G})^{-1}\mathbf{G}^T$ the generalised inverse of $\mathbf{G}$ gives the solution of Equation (2.10):

$$\begin{pmatrix} x \\ y \\ z \\ v\Delta_r t \end{pmatrix} \simeq \left(\mathbf{G}^T\mathbf{G}\right)^{-1} \mathbf{G}^T \begin{pmatrix} \widehat{r_1} \cdot \overrightarrow{S_1} - P^*_1 \\ \vdots \\ \widehat{r_n} \cdot \overrightarrow{S_n} - P^*_n \end{pmatrix} \tag{2.11}$$

One issue remains with the solution given in Equation (2.11): three unknowns, x, y and z (the coordinates of the receiver R), are needed to calculate the components of $\widehat{r_i}$, on the right side. Iteration is therefore necessary, with a guessed value for $\overrightarrow{R}$ at the start, but with $S_i \gg R$ even large errors on the guessed value of $\overrightarrow{R}$ do not greatly affect the accuracy of $\widehat{r_i}$ — see Equation (2.7) — and therefore neither $\mathbf{G}$. By tracking the values of $\overrightarrow{R}$ at each iteration it has been found that an error of 200 m on one value of R influences the next value by only about 1 mm and that when x, y and z are not known at all, taking 0 as a start value, i.e. $\overrightarrow{R}$ at the centre of the Earth, and iterating over Equation (2.11) four or five times gives the solution, if there is one, within 1 mm.

If $n > 5$, Equation (2.10) is used to check for erroneous pseudoranges from the residual. When an erroneous pseudorange is found, it is removed and the calculations redone.

2.1.4 Dilution Of Precision

The Dilution Of Precision (DOP) is the factor by which the relative geometry amplifies the effect of pseudorange errors on the positioning error (Leva et al., 1996, §7.1.3.1). When the geometry changes, the positioning error changes, even when the pseudorange error remains the same. Comparing Figure 2.4 with Figure 2.2 shows that the divergence between each consecutive hyperbola (the positioning error) increases when the distance between the transmitters (the geometry) decreases, even though the radius increment (the pseudorange error) between each circle is the same.

Menke (1989, §3.11) shows the link between measurement errors and the solution is given by the covariance matrix, here $\mathbf{D}$:

$$\mathbf{D} = \left(\mathbf{G}^T\mathbf{G}\right)^{-1} \tag{2.12}$$

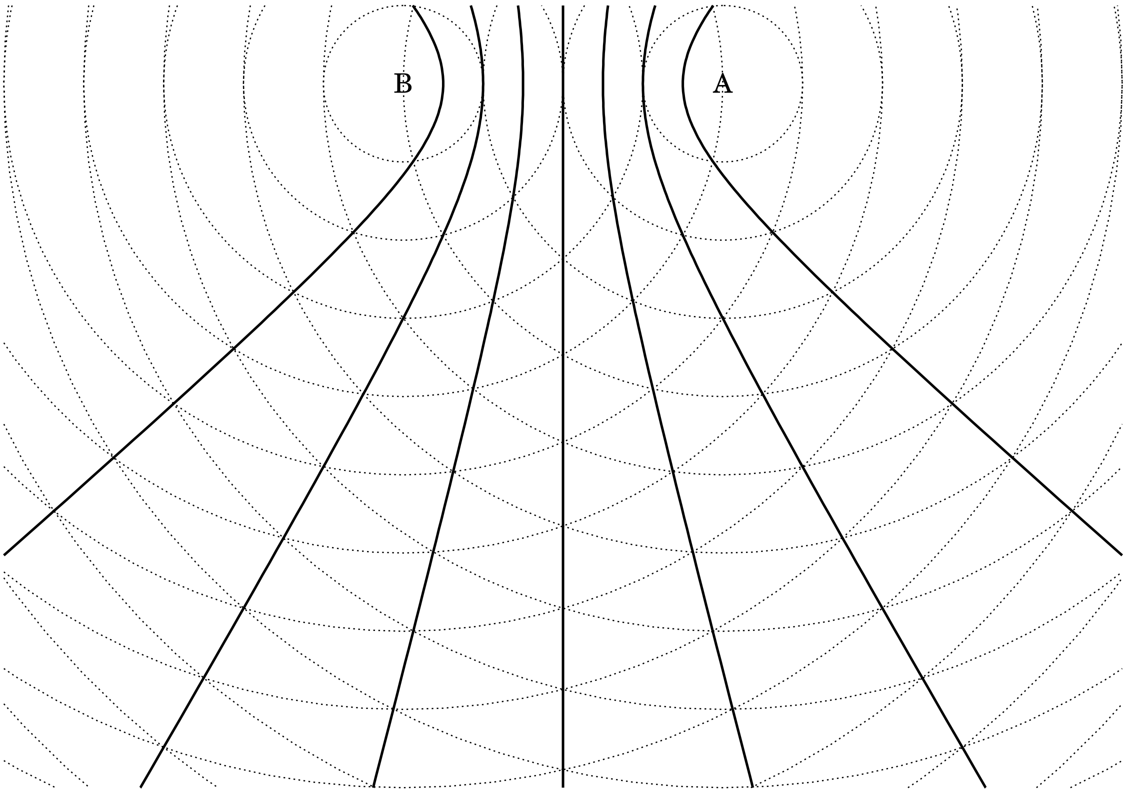

Figure 2.4: Dilution Of Precision : The closer the transmitters are, the more divergent the hyperbolae become.

The diagonal of **D** is made of the squares of the DOP coefficients D_X, D_Y, D_Z and D_T the XDOP, YDOP, ZDOP and Time DOP (TDOP). These give D_P the Positioning DOP (PDOP) :

$$D_P = \sqrt{D_X^2 + D_Y^2 + D_Z^2} \tag{2.13}$$

The PDOP is important to relate ΔR the uncertainty on the position of the receiver and Δp the Root Mean Square (RMS) uncertainty on the pseudoranges, somewhat as follows (Leva et al., 1996, eq.7.1) :

$$\Delta R \approx D_P \times \Delta p \tag{2.14}$$

so the lower the PDOP, the better.

With four satellites the best possible constellation is when the angle between each satellite is as wide as possible. In theory, this angle is the same as the angle between the segments joining the centre and the vertices of a tetrahedron, i.e. $\arccos -3^{-1} \simeq 109.5^\circ$. Equation (2.12) gives the PDOP for this configuration as about 1.3. The satellite configuration would then be one satellite at the zenith angle and the other three about 19.5° below the horizon and 120° of azimuth apart. This would only be possible for a satellite 400 km above the ground or above. For ground receivers, it is more reasonable to take a minimum elevation of 0.26 rad to lower the effects of multipath (see Equation (2.16) and context). The best possible constellation is then one satellite at the zenith angle and the other three 0.26 rad above the horizon and 120° of azimuth apart. Equation (2.12) gives the PDOP for this more realistic configuration as about 2.6.

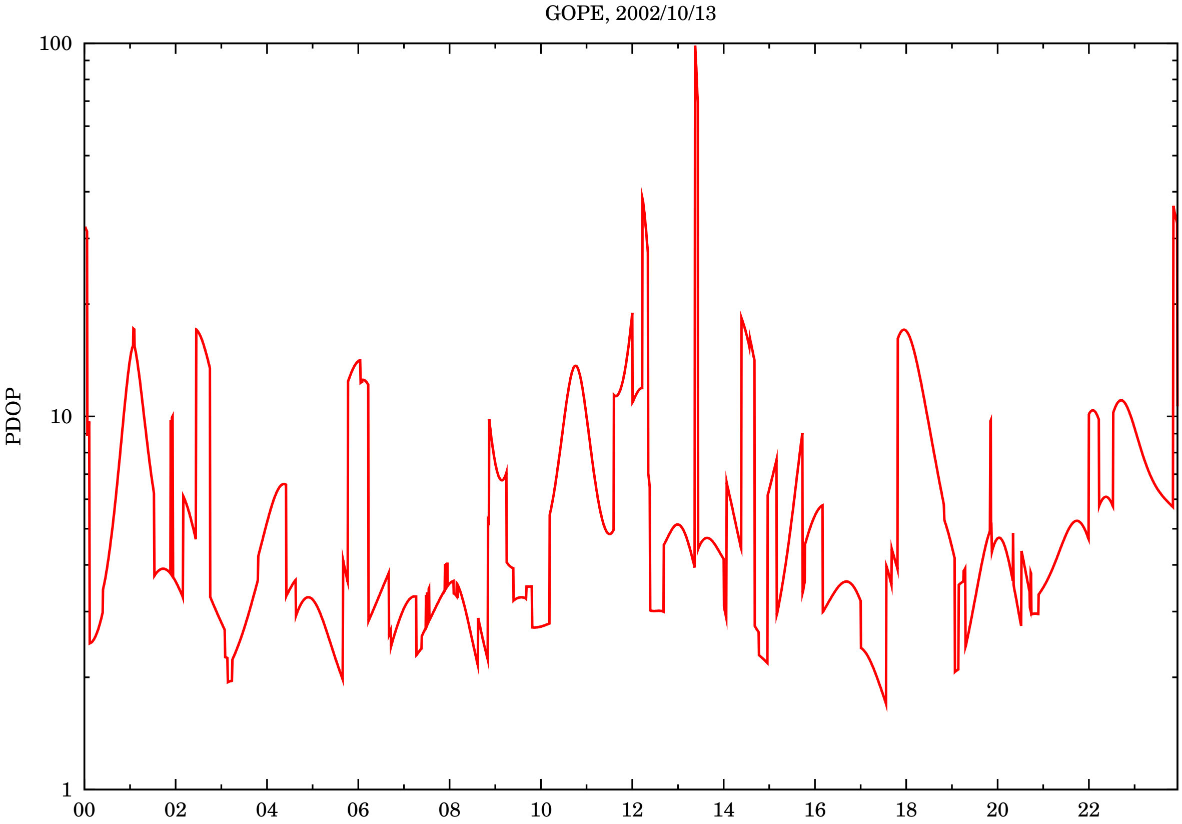

Figure 2.5: Daily evolution of PDOP calculated for GOPE on 13 Oct 2002. GOPE (for: Geodetic Observatory PEcny) is located at 49°54'49.3322" North, 14°47'8.2323" East at an altitude of 592.6 m (see `ftp://garner.ucsd.edu/pub/docs/site_logs/gope.log` and Figure 4.1b).

The PDOP values for a typical station have been plotted on Figure 2.5. As much more than four satellites are generally visible, the best achieved PDOP is of about 1.7. The PDOP decreases significantly when a satellite reaches above the cut-off elevation and increases significantly when a satellite goes below the cut-off elevation. It otherwise decreases or increases smoothly, somewhat with the angles between the satellites. There is not upper limit on the PDOP.

Equation (2.14) shows the only way to increase positioning accuracy for a given receiver position is to reduce the pseudorange uncertainty. This is detailed in the following section.

2.2 Pseudorange components

The errors on the pseudoranges have components from the signal transmitter, in our case the satellite, the propagation and the receiver.

The pseudorange P_n observed by a receiver on the frequency f_n can be defined in terms of the true range r, the speed of light in vacuum c, the receiver and satellite clock biases $\Delta_r t$ and $\Delta_s t$, the ionospheric delay If_n^{-2}, the tropospheric delay $T_{\phi,h}$ and the sum of multipath, background and receiver noise and of gravitational relativistic effects ϵ such that:

$$P_n = r + c(\Delta_r t + \Delta_s t) + If_n^{-2} + T_{\phi,h} + \epsilon \tag{2.15}$$

The influences of the background noise, including multipath, and gravitational relativistic effects (Ashby and Spilker, 1995) ϵ are neglected and not corrected for in this study.

A cut-off elevation ϕ_{min} is taken at:

$$\phi \le \phi_{min} = 0.26\,\mathrm{rad} \tag{2.16}$$

to lower the effects of multipath. Multipath induce errors on the pseudorange measurements of the order of 1.5 m for the P code (Braasch, 1994, §II.D.2 and fig.1). Multipath is changing and unpredictable for a roving receiver and is not compensated for specifically in this study.

The other terms are detailed below.

2.2.1 Tropospheric effects

Taking n the refractive index of the troposphere for microwaves, with the relative refractive index $n' = n - 1$, the following assumption is made, with C the molecular concentration:

$$n' \propto C \tag{2.17}$$

The perfect gas law and neglecting variations in temperature and in molecular composition, gives the pressure p and the volumic mass ρ such as:

$$p \propto C \propto \rho \tag{2.18}$$

The curvature of the Earth is also neglected with the variation of the gravitational acceleration g with the height h. This then gives the pressure variation dp with height and the height variation dh related as follows:

$$\mathrm{d}p = -\rho\ g\ \mathrm{d}h \tag{2.19a}$$

and with (2.18) this gives: $$\mathrm{d}p \propto -p\ \mathrm{d}h \tag{2.19b}$$

Taking (2.17), (2.18) and (2.19b) gives:

$$p \propto e^{-k\ h} \propto C \propto n' \tag{2.20}$$

with $k > 0$ and a constant. For a receiver at altitude h viewing a satellite at elevation angle ϕ, with dl a ray path element at altitude h', the tropospheric delay T is such as:

$$T_{\phi,h} \propto \int_h^\infty n'\,\mathrm{d}l = \int_h^\infty n'(\sin\phi)^{-1}\,\mathrm{d}h' \quad (2.21a)$$

with (2.20) this gives:

$$T_{\phi,h} \propto \frac{e^{-kh}}{\sin\phi} \quad (2.21b)$$

A more exact approach, i.e. taking into account the variation in the gravitational acceleration, the curvature of the Earth and the temperature variations with altitude, gives another approximation as follows, with the zenith delay at sea level $T_{\pi/2,0} \approx 2.44\,\mathrm{m}$, from Spilker (1994, eq. (44)):

$$T_{\phi,h} \simeq T_{\pi/2,0}\frac{1.0121 \times e^{-0.133\times10^{-3}\,h}}{\sin\phi + 0.0121} \quad (2.22)$$

The above equation has been used to calculate the tropospheric delays plotted on Figure 2.6. As expected from the above equation, the tropospheric delay is entirely elevation dependant. The minimum tropospheric delay for most satellite passes will be little above the zenith delay $T_{\pi/2,h} \approx 2.26\,\mathrm{m}$. Some satellite passes remain at low elevations and their minimum tropospheric delay will be significantly higher. The cut-off elevation of Equation (2.16) means the delays for all the passes are bounded at $T_{\phi,h} \le T_{\phi_{min},h} \approx 8.4\,\mathrm{m}$, although Equation (2.22) can give tropospheric delays of up to $T_{0,0} \approx 200\,\mathrm{m}$.

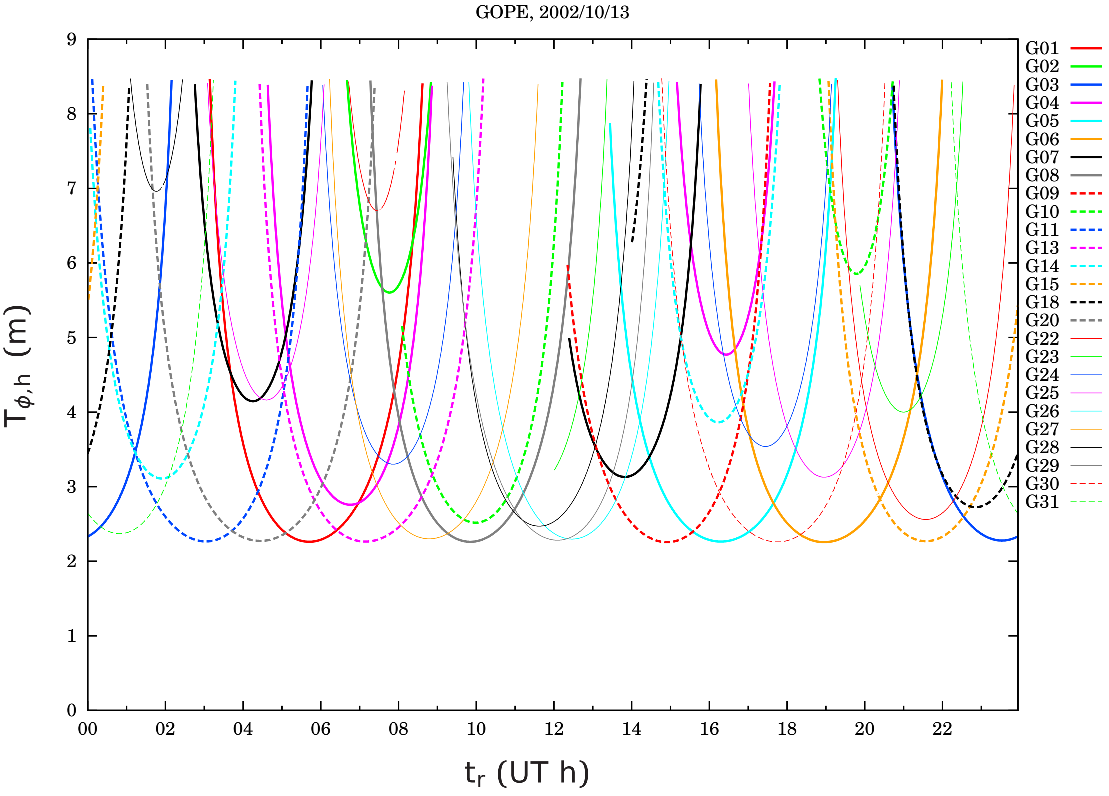

Figure 2.6: Tropospheric delays calculated for GOPE on 13 Oct 2002.

As the refractive index of the air depends on the temperature, the pressure and the humidity, $T_{\pi/2,0}$ will depend on these atmospheric parameters. The tropospheric effect is expected to be at least 2 m for stations below 1000 m of altitude. As shown previously, receivers should cancel out pseudorange measurements of satellites of elevation below a certain angle. This limits the tropospheric effects to a maximum of 15 to 25 m.

The value of $T_{\pi/2,0}$ given above is an average and can vary by $\Delta T_{\pi/2,0} = 0.14\,\mathrm{m}$ depending on the atmospheric conditions (Spilker, 1994, Table 5). This means there is an error on the tropospheric delay compensation $\Delta T_{\phi,h}$, with :

$$\Delta T_{\phi,h} \simeq \Delta T_{\pi/2,0} \frac{1.0121 \times e^{-0.133\times 10^{-3}\ h}}{\sin\phi + 0.0121} \tag{2.23a}$$

with Equation (2.16) this gives :

$$\Delta T_{\phi,h} \leq \Delta T_{\pi/2,0} \frac{1.0121}{\sin\phi_{min} + 0.0121} \tag{2.23b}$$

$$\Delta T_{\phi,h} \leq 0.53\,\mathrm{m} \tag{2.23c}$$

2.2.2 Ionospheric effects

The errors caused by ionospheric effects are the focus of this research, and a detailed explanation is deferred until the next Chapter. See Section 3.6.

2.2.3 Orbits of GPS satellites

The orbits of GPS satellites are inclined at 55° to the equatorial plane, are almost circular and have a semimajor axis of 26 561.75 km (Spilker and Parkinson, 1994).

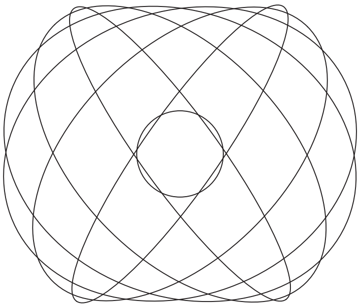

Figure 2.7: Side view of the Earth and the GPS orbits.

Their orbital period is nominally half a sidereal day, i.e. 11 h 58 min 2 s (Spilker and Parkinson, 1994), so that their ground tracks are fixed. However, Choi et al. (2004) show in their study that their period is actually 4 s inferior to half a sidereal day, i.e. 11 h 57 min 58 s, allowing for the J2 nodal drift (precession) of the Earth.

2.2.4 Satellite clock bias

The satellite clock bias $\Delta_s t$ is the sum (Kouba and Héroux, 2001, eq.(16); Kouba, 2003, §5.3.4) of a satellite-specific error $\Delta'_s t$ and of the relativistic effects on satellites with an elliptic orbit $\Delta^r_s t$.

The relativistic effects are due to the velocity of the satellite and to the gravitational field. The average relativistic effects are corrected at the satellites themselves (Ashby and Spilker, 1995, eq. (96) and after) by a frequency offset. However, as the orbits of the satellites are elliptic, these effects oscillate around the average. Taking S as the distance of the satellite to the centre of the reference frame and $\dot{S}$ as the rate of change of this distance, gives, after complex calculations, from Ashby and Spilker (1995, eq. (109)) or from the ICD 200c, p.89 :

$$c\Delta^r_s t = 2S\dot{S}c^{-1} \quad \text{giving:} \quad c\Delta_s t = c\Delta'_s t + 2S\dot{S}c^{-1} \tag{2.24}$$

An example of satellite relativistic clock biases have been plotted on Figure 2.8. This shows that satellites, depending on their ellipticity, can have a maximum relativistic clock bias of around 1 m (3 ns) when others have a maximum relativistic clock bias higher than 10 m (30 ns).

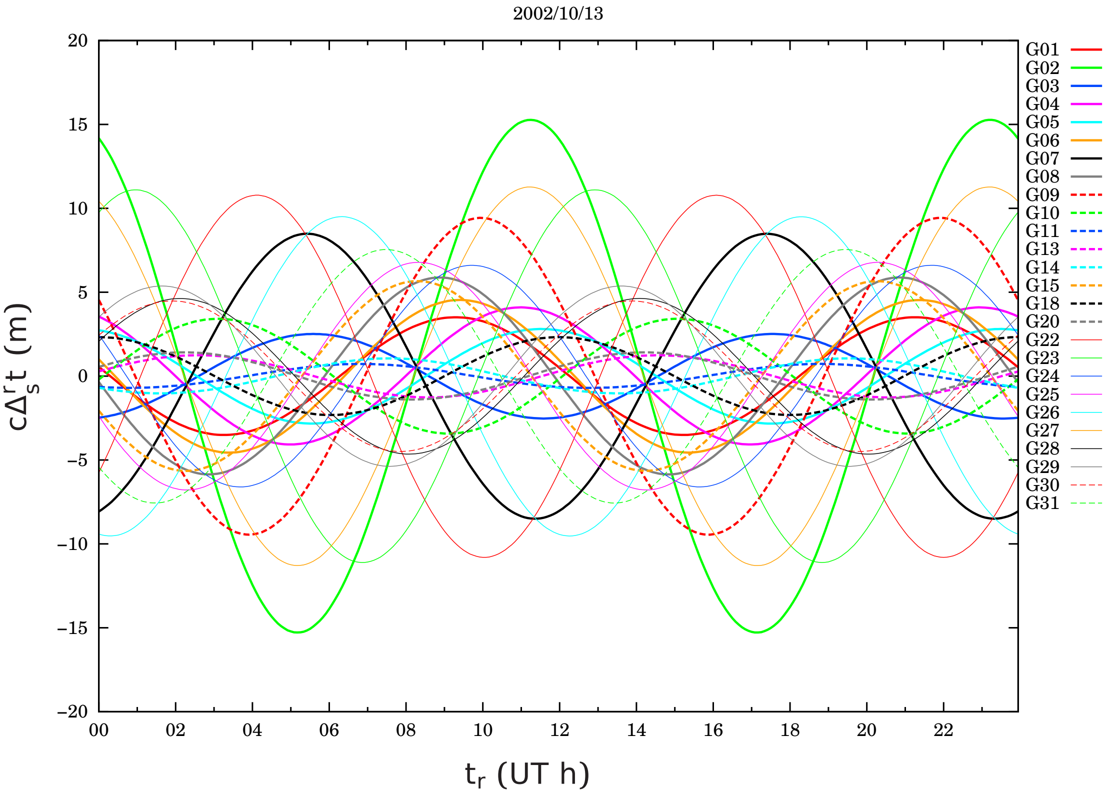

Figure 2.8: Satellite relativistic clock biases calculated on 13 Oct 2002.

Estimates for each of the satellite-specific errors $\Delta'_s t$ and for each of the satellites positions are calculated and made publicly available by the International GNSS Service (IGS) (Dow et al., 2005). These ephemeris show the satellite-specific error is very large, with $\left|\Delta'_s t\right| \leq 1\,\mathrm{ms}$. A linear interpolation from the IGS value gives the satellite-specific clock bias $\Delta'_s t$. The method to interpolate for the position of the satellite $\overrightarrow{S}$ and to obtain its velocity $\overrightarrow{\dot{S}}$ from the IGS ephemeris is explained in Section 4.3.

The satellites also show a small P1 to P2 bias $\Delta_s^{1\to 2}t$. This gives a different clock bias for each frequency. The IGS ephemeris contains the satellite clock bias for the dual-frequency. This means that the single frequency clock bias $\Delta_s^1 t$ is offset from the dual-frequency clock bias $\Delta_s t$, from Equations (3.9a) and (3.21b) :

$$\Delta_s^1 t = \Delta_s t + \frac{f_1^{-2}}{f_1^{-2} - f_2^{-2}} \Delta_s^{1\to 2} t \tag{2.25}$$

which is consistent with Kouba (2003, §6, eq. (28)). Satellite P1 to P2 biases are provided by the Center for Orbit Determination in Europe (CODE).

2.2.5 Sagnac effects

Two coordinate systems are used with the GPS (Spilker, 1996, Fig. 16), both with the centre of the Earth as origin : the **Earth-Centred Inertial (ECI) frame**, with the axes pointing in constant directions, irrelevant of the rotation of the Earth; and the **Earth-Centred Earth-Fixed (ECEF) frame**, with the axes rotating with the Earth. The ECI frame is almost inertial and as such the equations of the laws of physics will approximately apply with no modification. The ECEF frame is not inertial and the equations of the laws of physics do not apply unless the rotation of the frame is accounted for.

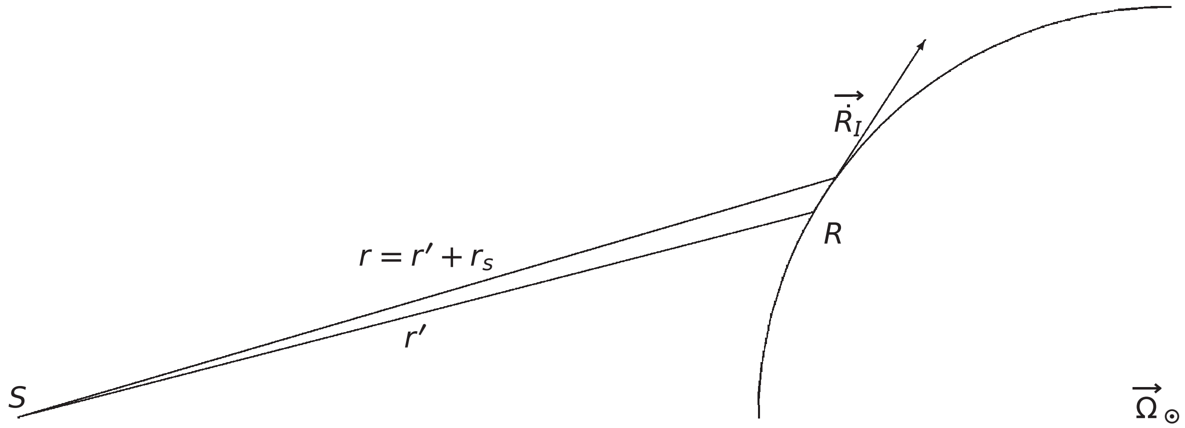

Figure 2.9: The Sagnac effect
By the time $r/c \simeq r'/c$ the signal reaches the receiver, the receiver position in the ECEF frame will have moved by $\dot{R}_I r/c$, or $\cos\left(\widehat{\overrightarrow{\dot{R}_I};\overrightarrow{RS}}\right) \times \dot{R}_I r/c$ with respect to the satellite.

A receiver of position vector $\overrightarrow{R}$ in the ECEF frame will have a velocity $\overrightarrow{\dot{R}_I}$ in the

ECI frame, with $\overrightarrow{\Omega}$ the rotation vector of the Earth, such that:

$$\dot{\overrightarrow{R_I}} = \overrightarrow{\Omega} \times \overrightarrow{R} \tag{2.26}$$

The receiver R is separated by a distance r, the true range, from the satellite S at the time of transmission (Figure 2.9). The signal will take a time $r/c \simeq r'/c$, where r' is the geometric range in the ECEF frame, to travel between the receiver and the satellite. During that time, the receiver will have moved by a distance r_s away from or towards the satellite. This is the Sagnac effect. From Ashby and Spilker (1995, eq. (90)), with $\overrightarrow{S}$ the position vector of the satellite and $\overrightarrow{R}$ the position vector of the receiver, the distance r_s is given by:

$$\begin{aligned}
r_s = c^{-1}\, \dot{R}_I r \cos\left(\widehat{\dot{\overrightarrow{R_I}};\overrightarrow{RS}}\right) &\simeq c^{-1}\, \dot{R}_I r' \cos\left(\widehat{\dot{\overrightarrow{R_I}};\overrightarrow{RS}}\right) && \text{(2.27a)}\\
&\simeq c^{-1}\, \dot{\overrightarrow{R_I}} \cdot \left(\overrightarrow{S} - \overrightarrow{R}\right) && \text{(2.27b)}\\
&\simeq c^{-1}\, \overrightarrow{\Omega} \times \overrightarrow{R} \cdot \left(\overrightarrow{S} - \overrightarrow{R}\right) && \text{(2.27c)}\\
&\simeq c^{-1}\, \overrightarrow{\Omega} \times \overrightarrow{R} \cdot \overrightarrow{S} = c^{-1}\, \overrightarrow{\Omega} \cdot \overrightarrow{S} \times \overrightarrow{R} && \text{(2.27d)}
\end{aligned}$$

An example of Sagnac distances have been plotted on Figure 2.10. This shows that Sagnac distances are often very large, here in this example up to 25 m, but in certain cases they can be as large as 41 m. Equation (2.27d) shows that the uncertainty on the Sagnac delay Δr_s can only be due to the uncertainty on the satellite ephemeris ΔS and the uncertainty on the receiver positioning ΔR. Even when these are large, e.g. $\Delta S = 10\text{m}$ and $\Delta R = 100\text{m}$, this uncertainty remains small: $\Delta r_s < 0.7\text{mm}$.

When calculating the true range between the point of transmission and the point of reception one must take into account not only the geometric range r' but also the Sagnac effect r_s induced by the rotation of the reference frame. This gives the true range r, with $\overrightarrow{S}(X,Y,Z)$ and $\overrightarrow{R}(x,y,z)$ the position vectors and coordinates in the ECEF frame of respectively the satellite and the receiver as:

$$r = r_s + r' \quad \text{with} \quad r' = \sqrt{(X-x)^2 + (Y-y)^2 + (Z-y)^2} \tag{2.28}$$

The maintainers of the IGS station give the exact receiver position in the header of the Receiver Independent Exchange Format (RINEX) file (Gurtner, 2001) and the exact satellite position is interpolated from the IGS ephemeris (see Section 4.3).

2.2.6 Error budget

As shown on Table 2.1, all the errors presented previously, apart from the ionospheric delay, can be precisely compensated for by simple receivers.

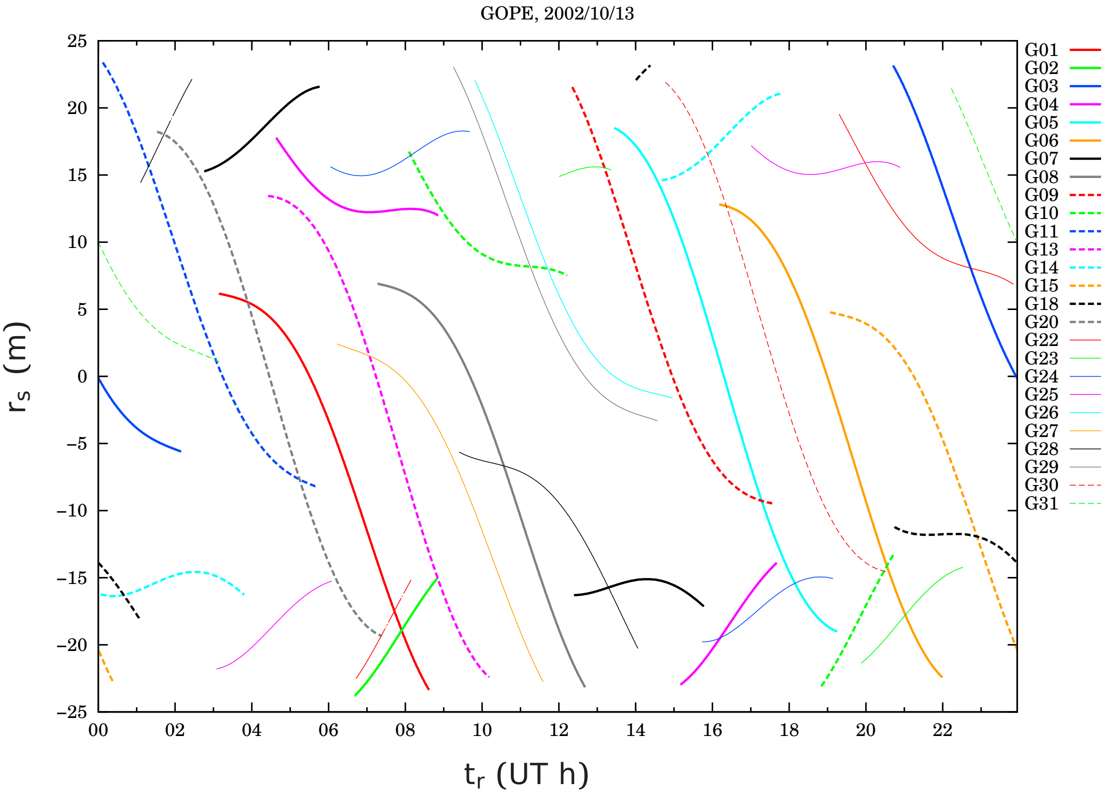

Figure 2.10: Sagnac distances calculated for GOPE on 13 Oct 2002.

Error source	Range /m min → max	Maximum compensation error /m
Tropospheric delay	2.3 → 9	0.5
Ionospheric delay	1.5 → 35	20 (NAVSTAR, 1996, Table 3-1)
Satellite clock bias	$-3{\cdot}10^5 \rightarrow 3{\cdot}10^5$	2 on predicted IGS ephemeris (IGS, 2005)
Sagnac effect	-41 → 41	$7{\cdot}10^{-4}$

Table 2.1: Pseudorange errors. The ranges for the tropospheric and ionospheric delays are given for a cut-off elevation of $\phi \leq \phi_{min} = 0.26\,\mathrm{rad}$.

2.3 Conclusion

In this Chapter the principle of GPS positioning and the origin of its errors have been presented. The uncertainty on the positioning depends on the PDOP, which comes from the constellation, and on the quality of the pseudorange measurement. The constellation is given, the number of satellites is limited, and all errors on the pseudorange measurement, but the ionospheric delay, can be precisely compensated for. A method to compensate precisely for the ionospheric delay, proposed in this project, is presented in Chapter 3.

Chapter 3

Ionospheric imaging and corrections

In Chapter 2, the many factors that affect the positioning accuracy with GPS have been presented. It has been shown that the accuracy can be improved by compensating for many of the factors that affect the pseudoranges. As the temporally and geographically variable errors caused by ionospheric effects are the focus of this research, a detailed explanation of the compensation has been deferred until this Chapter.

The ionosphere is described in Section 3.1 followed by a description of methods to observe it in Section 3.2. A method to map the Free Electrons Density (ED) is then presented with a numerical example of tomography in Section 3.3 followed by a detailed description of how tomography is applied to the ionosphere in Section 3.4. Current ionospheric correction systems are reviewed in Section 3.5. In Section 3.6 the methods used to correct for the ionospheric delay that are compared in this project are explained.

3.1 The ionosphere

The first part of this section is based on a review of the basic physics of the ionosphere by Rishbeth (1988). A detailed description of the physics of the ionosphere has been made by Kelley (2007). After a brief description, some of the basic physics will be detailed in Section 3.1.1 before presenting its features in Section 3.1.2 and Section 3.1.3.

The ionosphere is the ionised layer of the upper atmosphere, defined as the part in which the ED is sufficient to influence the propagation of radio waves. Its limits are not well defined. Its lower boundary lies around 60 km above the surface of the Earth during the day and 90 km at night.

The ionosphere is formed by ionising radiations, mainly high energy, X-ray and Extreme Ultra-Violet (EUV), photons but also charged particles. At any point, a maximum of only 1% of its molecules is ionised. The radiations come mainly from the Sun and hence it has a strong daily cycle and a yearly cycle. The Sun has spots : regions of high magnetic field, lower visible light emission (hence their name) and higher ionising radiation emission (hence their impact on the ionosphere). The sunspot number evolves during an 11 year cycle, going from below 20 at what is called solar minimum, the start and end of each cycle, to typically around 110 at what is called solar maximum (Hargreaves, 1992, §5.2.4). The latest cycle peaked in 2000 and 2002 and ended in 2008 with no sunspots, a record low. A small fraction of the radiations are also of cosmic origin.

3.1.1 Basic physics

The ionising radiations dissociate molecules, creating monoatomic molecules of the normally diatomic elements nitrogen and oxygen. The ionising radiations knock out electrons from molecules, creating positive ions. There are therefore monoatomic positive ions created. Free electrons and monoatomic positive ions can not recombine on their own, as all reactions must conserve momentum and energy, in addition to satisfying quantum theory. This means free electrons and monoatomic positive ions will coexist until either a three body collision occurs, the third body taking the excess energy, or until they recombine with other neutral molecules or polyatomic ions of the opposite charge. When recombining with neutral molecules, free electrons and monoatomic positive ions create, respectively, negative ions and polyatomic positive ions, which themselves may recombine. All the reactions detailed above may leave atoms and molecules in an exited state. These excited atoms and molecules emit photons, giving some glow to the ionosphere.

The flux of particles from the Sun is called the Solar wind. All charged particles, i.e. of Solar or cosmic origin or free electrons or ions, are deviated, and bound if no other force is strong enough, by the Earth's magnetic field. This means Solar or Earth winds will create currents of charged particles in the ionosphere, which will in turn modify the magnetic field of the Earth. These currents will separate positive and negative charges. This accumulation of charges will create electric fields, which will in turn have an effect on the movements of charged particles. When the Sun emits a large amount of high energy photons or charged particles, this makes the ionosphere particularly active. The changes in the magnetic field are then particularly important, giving these events their name of geomagnetic storms.

Also, charged particles of Solar or cosmic origin coming to the Earth tend to either be deviated away from the Earth or be guided towards its magnetic poles. The ionosphere is therefore particularly active around the magnetic poles. The region around the magnetic poles is actually so active it glows particularly strongly : it is the polar aurora, at what is called the auroral region. The regions close to the geographic equator are the most exposed to electromagnetic radiations from the Sun. However it is the area on both sides of the magnetic equator that is particularly active and ionised, because of the movements of charged particles and of the configuration of the magnetic and electric fields there (Materassi et al., 2003). It is the equatorial anomaly, at what is called the equatorial region. It is characterised by a magnetic-field-aligned ED peak, as is well shown by Andreeva et al. (2000, fig.1) and Yeh et al. (2001, fig.1).

3.1.2 Structure

Simple functions giving ED profiles can be derived from basic assumptions. For limited altitude ranges they can be very simple, e.g. linear functions. The Chapman (1931) function assumes a monochromatic radiation dissociating the sole constituent of an atmosphere with exponentially decaying density in two components. The production rate of the two components is assumed to be proportional to the energy absorbed. The recombination rate of the two components is assumed to be proportional to the square of the density of the dissociated components. Epstein functions are also used (Hardy et al., 1987, eq.4; Meggs and Mitchell, 2006, §2).

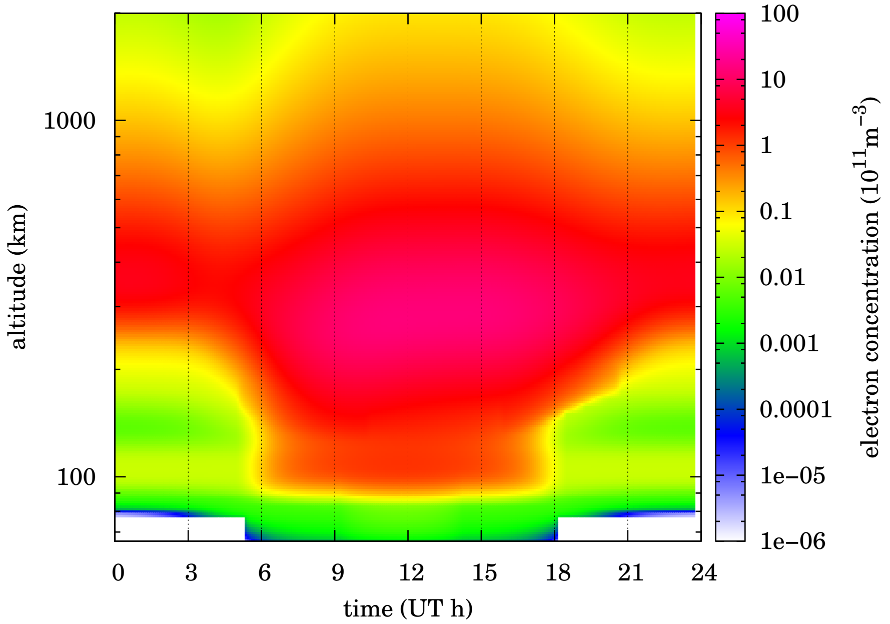

Figure 3.1: Daily evolution of the Free Electrons Density profile as given by the IRI 2007 (without storm model) on the 13 Oct 2003 at 50° North 0° East.

Figure 3.1 gives the evolution of the ED profile throughout one quiet day as given by the IRI 2007 (see Section 3.5.3). It shows the layered structure of the ionosphere. The ionosphere has two main layers : the E layer, around 100 km, and the F layer, above 150 km. Other layers, C and D, below 90 km, have electron densities so low they are not important to this project. The F layer is produced by low energy EUV. It is itself separated in two layers, F1 and F2, respectively below and above 200 km. The F2 layer is the only layer to keep a high ED at night because the recombination is much slower there, not only because of the lower density of molecules but also because of their composition. The E layer is produced by high-energy EUV and soft (low energy) X rays. It may become particularly active during geomagnetic storms, giving the sporadic E layer.

Figure 3.1 shows the ED peak height remains similar, from 300 to 350 km, throughout the day. During storms, the ED profile can change significantly (Bust et al., 2007). In particular, Bust et al. (2007) shows the ED peak height can increase to 400 km and up to almost 800 km.

Most of the literature about the ionosphere covers electron density profiles only up to below 1000 km. It must be noted that free electrons exist in relatively important concentrations well up to the GPS orbits (Balan et al., 2002; Gulyaeva, 2003) in the region known as the plasmasphere.

The ionosphere has, by definition, an effect on the propagation of electromagnetic waves. Of particular interest to this project it slows and refracts microwaves. This induces the ionospheric delay that is important in the context of GPS navigation accuracy.

3.1.3 Scintillation

The amplitude and phase of signals that have propagated through the ionosphere can sometimes exhibit rapid fluctuations in attenuation and phase. This is explained by ED irregularities in the ionosphere that diffract the signal.

Scintillation is more intense at the auroral and equatorial regions. Intense scintillation causes losses of lock. For positioning receivers, at best the signal is lost, at worse the pseudorange measurement drifts well away from its real value, greatly corrupting the final positioning solution.

3.2 Experimental observations

Because of its influence on the propagation of radio waves and on the variation of the magnetic field of the Earth, the ionosphere has an important impact on man-made systems. A lot of resources are therefore put into studying it and there are many different techniques (Rishbeth, 1988, §1.4) to do so. After giving a little more details about the propagation of radio waves in the ionosphere, a review of some observation techniques will be given, first and briefly point observations, second and in more details line integral measurements.

3.2.1 Ionosphere index and group delay

The Appleton formula (Davies, 1989, eq. (3.8)) gives the refractive index of an electromagnetic wave in a magnetised plasma. The magnetic field $\overrightarrow{\omega_B}$ has a component along the direction of propagation B_L and a component perpendicular to the direction of propagation and to the polarisation B_T. The influence of the component of the magnetic field along the polarisation is neglected. Taking e and m the charge and mass of the electron and $B < 80{\cdot}10^{-6}\,\mathrm{T}$ the intensity of the magnetic field of the Earth gives the plasma giro angular frequency $\overrightarrow{\omega_B} = e\overrightarrow{B}/m$ with its components ω_{B_L} and ω_{B_T} relating to B_L and B_T respectively. With GPS, $f > 1.2{\cdot}10^6\,\mathrm{Hz}$ (see Section 3.2.3) and on the Earth $B < 80{\cdot}10^{-6}\,\mathrm{T}$. So the ratio of the plasma giro frequency f_B and of the wave frequency is small :

$$\frac{f_B}{f} = \frac{\omega_B}{\omega} = \frac{eB}{2\pi f m} < 0.002 \ll 1 \tag{3.1}$$

With ϵ_0 the free space permittivity the plasma angular frequency ω_N is :

$$\omega_N = \sqrt{\frac{Ne^2}{m\epsilon_0}} \tag{3.2a}$$

Even when the ED is high, the plasma frequency $f_N = \omega_N/2\pi$ is still small compared to the frequency of GPS, e.g. :

$$N = 100{\cdot}10^{11}\,\mathrm{m}^{-3} \quad \text{gives} \quad f_N \simeq 28\,\mathrm{MHz} \ll f \tag{3.2b}$$

Davies (1989) writes that "collisions are negligible ... in the E and F regions". In this case we can take a simplified form of the Appleton formula from Davies (1989, eq. (3.9)). Simplifying it a little more by taking into account Equation (3.2b) gives :

$$n_\phi \simeq \sqrt{1 - \frac{\left(\frac{\omega_N}{\omega}\right)^2}{1 - \frac{w_{B_T}^2}{2w^2} \pm \sqrt{\frac{w_{B_T}^4}{4w^4} + \frac{w_{B_L}^2}{w^2}}}} \tag{3.3a}$$

then also taking into account Equation (3.1) gives :

$$n_\phi \simeq \sqrt{1 - \frac{\left(\frac{\omega_N}{\omega}\right)^2}{1 \pm \frac{w_{B_L}}{w}}} = \sqrt{1 - \frac{\omega_N^2}{\omega^2 \pm \omega\omega_{B_L}}} \simeq \sqrt{1 - \left(\frac{\omega_N}{\omega}\right)^2} = \sqrt{1 - \frac{Ne^2}{m\epsilon_0\omega^2}} \tag{3.3b}$$

The last approximation above shows neglecting the magnetic field leaves an error of less than 0.001 on the relative index $1 - n_\phi$. Equation (3.3b) shows that the influence of a charged particle is related to the ratio of the square of its charge over its mass. Nucleons have a mass more than 1800 times higher than electrons so the influence of ions on the ionospheric index is negligible. Also, we have $n_\phi < 1$, which means the phase travels faster than the speed of light in vacuum c at c/n_ϕ.

However the phase refractive index is a function of frequency, i.e. the ionosphere is dispersive, so we must consider the group index n_g. Let's have two waves of amplitude 1, of close angular frequencies $\omega - \mathrm{d}\omega$ and $\omega + \mathrm{d}\omega$ and of close wave numbers $k - \mathrm{d}k$ and $k + \mathrm{d}k$ respectively. Taking their sum at a distance r of the emitter and at a time t :

$$\cos([k - \mathrm{d}k]r - [\omega - \mathrm{d}\omega]t) + \cos([k + \mathrm{d}k]r - [\omega + \mathrm{d}\omega]t) = 2\cos(kr - \omega t)\cos(\mathrm{d}kr - \mathrm{d}\omega t) \tag{3.4}$$

gives a wave of wavelength $2\pi/k$ with an enveloppe of wavelength $2\pi/\mathrm{d}k$. The speed of the enveloppe is the group velocity v, giving the group index :

$$v = \frac{\mathrm{d}\omega}{\mathrm{d}k} = \frac{c}{n_g} \tag{3.5a}$$

as $k = \omega n_\phi / c$, taking the invert gives :

$$\frac{n_g}{c} = \frac{\mathrm{d}\frac{\omega n_\phi}{c}}{\mathrm{d}\omega} \quad \text{or} \quad n_g = \frac{\mathrm{d}(\omega n_\phi)}{\mathrm{d}\omega} = n_\phi + \omega\frac{\mathrm{d}n_\phi}{\mathrm{d}\omega} \tag{3.5b}$$

with Equation (3.2a), this gives :

$$\begin{aligned}
n_g &\simeq n_\phi + \omega \frac{\mathrm{d}\sqrt{1-\left(\frac{\omega_N}{\omega}\right)^2}}{\mathrm{d}\omega} && \text{(3.5c)}\\
&\simeq n_\phi + \frac{\omega}{2n_\phi} \times \frac{\mathrm{d}\left[1-\left(\frac{\omega_N}{\omega}\right)^2\right]}{\mathrm{d}\omega} = n_\phi - \frac{\omega\omega_N^2}{2n_\phi} \times (-2)\omega^{-3} && \text{(3.5d)}\\
&\simeq n_\phi + n_\phi^{-1}\left(\frac{\omega_N}{\omega}\right)^2 = \frac{n_\phi^2 + \left(\frac{\omega_N}{\omega}\right)^2}{n_\phi} && \text{(3.5e)}\\
&\simeq \frac{1-\left(\frac{\omega_N}{\omega}\right)^2 + \left(\frac{\omega_N}{\omega}\right)^2}{n_\phi} = n_\phi^{-1} && \text{(3.5f)}
\end{aligned}$$

When considering Equation (3.2b), the relative ionospheric indexes, respectively $1-n_g$ and $1-n_\phi$, can be approximated from Equations (3.3b) and (3.5f) to :

$$1-n_g \simeq -(1-n_\phi) \simeq \frac{\omega_N^2}{2\omega^2} \qquad \text{(3.6a)}$$

This gives If^{-2} the ionospheric group delay or phase advance in metres, with f the frequency of the signal in Hz, $\int N\,\mathrm{d}l$ the Total Electron Concentration (TEC) in m^{-2}, and I the ionospheric delay term in $\mathrm{m\,s}^{-2}$, like Klobuchar (1996, eq. (5)), :

$$\begin{aligned}
If^{-2} &\simeq 40.3f^{-2}\int N\,\mathrm{d}l && \text{(3.6b)}\\
\text{or}\quad I &\simeq 40.3\int N\,\mathrm{d}l && \text{(3.6c)}
\end{aligned}$$

It must be highlighted that this is an approximation.

Whenever a wave travels along a direction that is different to the phase refractive index gradient, the ray bends towards that gradient, so the ray path is not a straight line and therefore longer. The use of a signal that propagates from a satellite to another satellite and that partly travels through the atmosphere is called radio occultation. A radio occultation signal travels horizontally when it is closest to the Earth, so somewhat perpendicularly to the refractive index gradient. Schreiner et al. (1999, Tab. 1) calculated a bending angle for radio occultation rays with L1 GPS frequency of $\approx 2{\cdot}10^{-3}$ rad for an ionosphere with an ED peak of $100{\cdot}10^{11}\mathrm{m}^{-3}$, similar to one of a quiet day at solar maximum conditions. This shows that even in this worse possible case of ray bending, the effect is negligible at GPS frequencies.

3.2.2 Point measurements

With instruments on rockets or satellites, various in-situ measurements, including ED, can be carried out. These measurements are however limited to where these vehicles can reach and when : rockets with their once-per-launch trajectory and satellites with their orbit.

Equation (3.3b) shows that when the ED N is large enough and when the frequency f is low enough, the phase refractive index n_ϕ becomes imaginary, which means the wave is reflected. This is intensely used by many instruments, in particular ionosondes, which are radars that send a sweeping frequency pulse vertically towards the ionosphere. From the echoes and delays one can work out the ED profile up to the peak. As they are relatively simple, there are many ionosondes on the surface of the Earth. Their field of observation is however limited to below the ED maximum, which is quite low as shown on Figure 3.1. Few ionosondes, called topside sounders, are mounted on satellites orbiting above the ED peak, but generally much below 2000 km of altitude (Benson, 1997), and send their pulse towards the surface.

Electrons very weakly back-scatter high frequency radio waves. Incoherent Scatter Radars (ISRs) send a very powerful pulse and analyse the weak echo to give, all along the ray path, electron and ion density, temperature and speed (Rishbeth and Williams, 1985, tab.1). However these are very expensive instruments to run and they are very few. Also, their range is of around 1000 km at most.

Do to their limitations, the point measurements techniques listed above are not suited to give information about the full-height of the ionosphere.

More details about ionospheric instrumentation can be found in Hargreaves (1992, §3).

3.2.3 Dual-frequency TEC measurements

The GPS satellites emit on several frequencies (Space and Missile Systems Center (SMC)), two of which can be used for positioning. Both frequencies are modulated with a coarse acquisition (C/A) code and a precise (P) code. The P code is repeated at such a high frequency that receivers need to track the C/A code first to be able to use the P code. The C/A code on the L1 frequency of $f_1 = 1575.42\,\text{MHz}$ (C1) is unencrypted, so all GPS receivers can use the P code on the L1 frequency (P1). The coarse acquisition code on the L2 frequency of $f_2 = 1227.6\,\text{MHz}$ (C2) is encrypted on all but the newer satellites, so only the more expensive and heavier survey grade GPS receivers can use the P code on the L2 frequency (P2), by tracking it with the P1 code instead of the C2 code. They are called dual-frequency receivers and are used for surveying work, such as geodetic positioning and also the survey of GPS satellites themselves by the IGS. Many networks make available in near real-time the data from hundreds of these receivers. As the signals travel through the ionosphere below GPS satellites orbit, they give information about all of the ionosphere relevant to positioning.

Dual-frequency GPS receivers can record four particular observables in the RINEX files they produce (Gurtner, 2001). P_1 and P_2 are the pseudoranges from the precise P-code. L_1 and L_2 are the recorded carrier phases of the signal converted to distance units. Expressing P_1 and P_2 with P_0 the ionosphere-free pseudorange,

If^{-2} and ϵ the noise which includes multipath :

$$P_1 = P_0 + If_1^{-2} + \epsilon_1 \tag{3.7a}$$

$$P_2 = P_0 + If_2^{-2} + \epsilon_2 \tag{3.7b}$$

and expressing L_1 and L_2 with P_0, If^{-2}, n the integer ambiguity and λ the carrier wavelength :

$$L_1 = P_0 - If_1^{-2} + n_1\lambda_1 \tag{3.8a}$$

$$L_2 = P_0 - If_2^{-2} + n_2\lambda_2 \tag{3.8b}$$

gives two expressions for I :

$$\frac{P_1 - P_2}{f_1^{-2} - f_2^{-2}} = I + \frac{\epsilon_1 - \epsilon_2}{f_1^{-2} - f_2^{-2}} \tag{3.9a}$$

$$\frac{L_1 - L_2}{-f_1^{-2} + f_2^{-2}} = I + \frac{n_1\lambda_1 - n_2\lambda_2}{-f_1^{-2} + f_2^{-2}} \tag{3.9b}$$

Equation (3.9a) gives I with a noise term (see also Equation (3.20)). It has been used to obtain the ionospheric delay values plotted on Figure 3.2a and Figure 3.2c. Equation (3.9b) gives I with an offset term from the integer ambiguity. The integer ambiguity stays constant while the satellite is visible apart from large and sudden changes called cycle slips. The offset term of Equation (3.9b) depends on the integer ambiguity and stays also constant apart from similar changes. As the changes of the offset term of Equation (3.9b) are large and sudden, they are easily detectable. The offset between cycle slips is taken as a weighted mean of the differences between the first and second solutions above, i.e. the value of I is computed by fitting Equation (3.9b) into Equation (3.9a). The cosecant of the elevation angles are used for the weights. This way, the weights are correlated with the signal to noise ratio (Klobuchar, 1996, fig. 2). This method has been used to obtain the ionospheric delay values plotted on Figure 3.2b and Figure 3.2d.

All plots on Figure 3.2, (a) to (d), have a similar pattern showing the elevation dependence of the ionospheric delay and the daily cycle of the ionosphere. The ionospheric delay decreases by typically 3 m at night and by around 15 m during the day as the satellites rise and then increases by a similar amount as the satellites set : when the satellites are close to the horizon their signals travel through more ionosphere so are more delayed and when the satellites are high in the sky their signals travel through less ionosphere so are less delayed. The ionospheric delay is not only strongly elevation dependent but also depends on the daily cycle of the ionosphere. At night, when the ionosphere is least ionised, the minimum delay, for the maximum elevation, is around 1 or 2 m and the maximum delay, for the minimum elevation, is around 5 m. During the day, when the ionosphere gets ionised, the minimum delay is around 6 m and the maximum delay is around 20 m. There are a few outliers, most likely caused by losses of lock, on 13 Oct 2002 at around 2, 7:30, 11 and 20 UT and on 27 Oct 2003 at around 6, 13 and 18 UT. The receiver did not get a proper lock back after the losses on 13 Oct 2002 at around 7:30 UT for satellite G22 and on 27 Oct 2003 at around 18 UT for satellite G10 but kept giving rapidly fluctuating pseudorange measurements.

Comparing, on Figure 3.2, (a) and (c) with, respectively, (b) and (d) shows

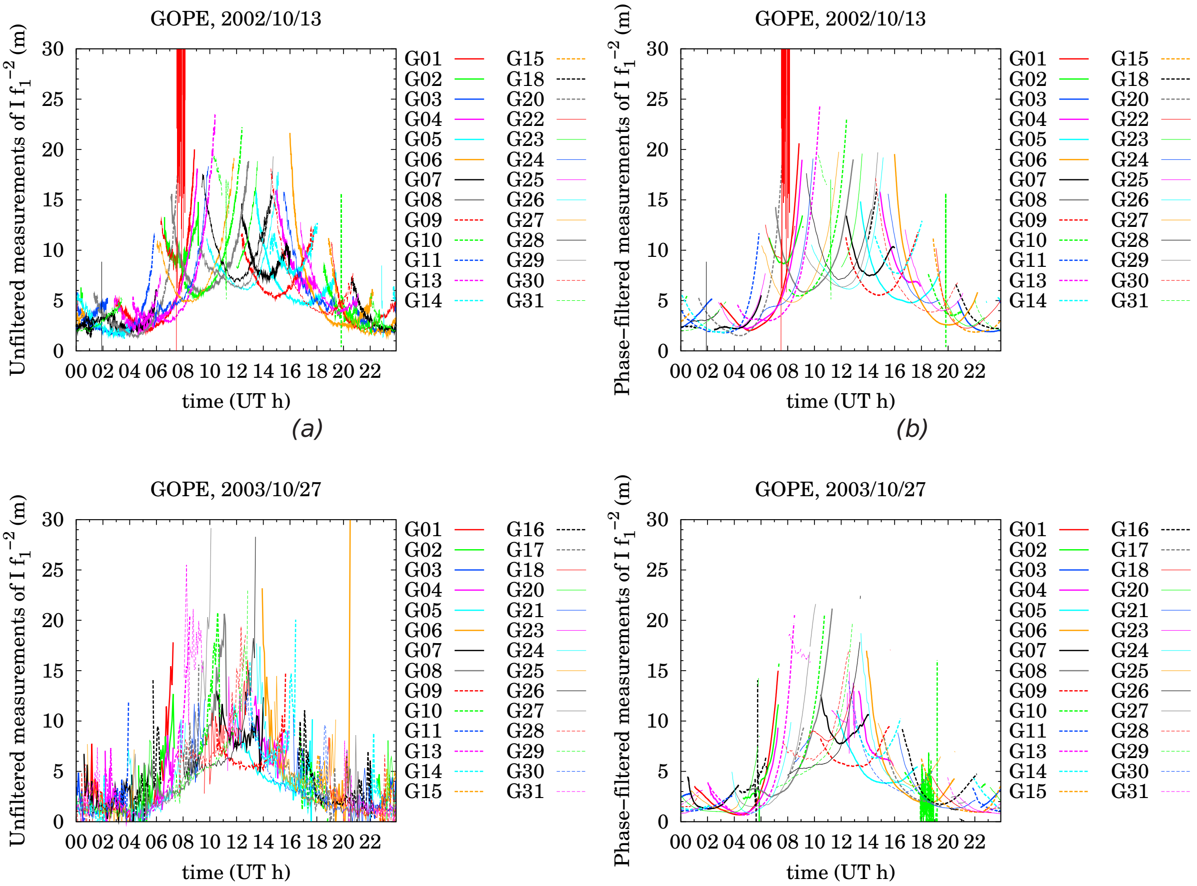

(a) (b)

(c) (d)

Figure 3.2: Ionospheric delays measured with the unfiltered, (a) and (c), and phase-filtered, (b) and (d), methods from GOPE pseudoranges on 13 Oct 2002, (a) and (b), and on 27 Oct 2003, (c) and (d). See also Figure 4.4.

how the noise is removed with this method. The noise on 13 Oct 2002, Figure 3.2a, is about 1 m peak-to-peak whatever the elevation. The noise on 27 Oct 2003, Figure 3.2c, is around 2 m peak-to-peak at higher elevations and increases to around 5 m peak-to-peak at the lowest elevation. The data for this plot has been subsampled to keep it readable. Interestingly, the records, available at `ftp://garner.ucsd.edu/pub/docs/site_logs/gope.log`, report no changes either to any component of the GOPE receiver or to its position between the dates of Figure 3.2a and Figure 3.2c. This reveals that the increase in noise, seen when comparing these two plots, is therefore most likely a change to the nearby landscape and also that noise is mainly induced by multipath.

Like satellites (see Equation (2.25)), receivers also show a P1 to P2 bias $\Delta_r^{1\to2}t$, also called the interfrequency bias. As this which affects equally all pseudoranges, this impacts only the timing solution and not the positioning at all, as shown by Equation (2.5). However it has an impact on the TEC measurement. P1 to P2 biases are also provided by the CODE, with the RMS uncertainties, for a limited number of receivers. The data from the CODE shows a typical value and uncertainty of receiver P1 to P2 bias is 2.00 ± 0.06 m (7.0 ± 0.2 ns), which means, from equations

(3.6c) and (3.9a), a correction of :

$$\frac{c\Delta_r^{1\to 2}t}{40.3\left|f_1^{-2}-f_2^{-2}\right|} \approx 19.0 \pm 0.5\cdot 10^{16}\,\mathrm{m}^{-3} \tag{3.10}$$

must be carried out on the dual-frequency TEC measurement. Dear and Mitchell (2006) showed that using Multi Instrument Data Analysis System (MIDAS) to evaluate the interfrequency bias gives results similar to the CODE.

The measurements from dual-frequency receivers give information about the TEC, i.e. the line integral of ED. Tomography is needed to process line integrals and give an image.

3.3 2D example of tomography

This section is based on Mitchell and Spencer (2003). See also Yin and Mitchell (2005).

The aim is to invert line integral measurements to produce a discrete map of the spatial distribution of a parameter. The parameter has been pixelised and represented in Figure 3.3a. Line integrals have been measured : their values are shown at the bottom of Figure 3.3a. Taking **A** the 6×90 matrix of the pixel to line intersections (Figure 3.3b shows the pixel intersection of two ray paths) and **x** the vector of pixel values gives **b** the vector of line measurements :

$$\mathbf{Ax} = \mathbf{b} \tag{3.11}$$

There are far less line integral measurements (here, 6) than values in each pixel (here, 90) and the problem can not be solved directly.

Thankfully the parameter can be precisely approximated by a weighted sum of, here five, mapping functions, represented in Figure 3.3, (c) to (g). Taking **X** the 90×5 matrix of mapping functions and **w** the vector of weights gives :

$$\mathbf{x} = \mathbf{Xw} \tag{3.12}$$

and, taking Equation (3.11) and Equation (3.12) gives :

$$\mathbf{AXw} = \mathbf{b} \tag{3.13}$$

The unknowns are now the weights of the mapping functions and there are more measurements than there are weights : the product **AX** gives a 6×5 matrix of line integrals of the mapping functions whose values are at the bottom of Figure 3.3, (c) to (g).

We then need to solve Equation (3.13) to get **w**. This is done using the natural generalised inverse matrix (Menke, 1989, §7.6). The Singular Values Decomposition (SVD) (see Press et al. (1992) for a good explanation of SVD) of **AX** returns two orthogonal matrices $\mathbf{U_{AX}}$ and $\mathbf{V_{AX}}$ and a diagonal matrix of singular values $w_{\mathbf{AX}}$,

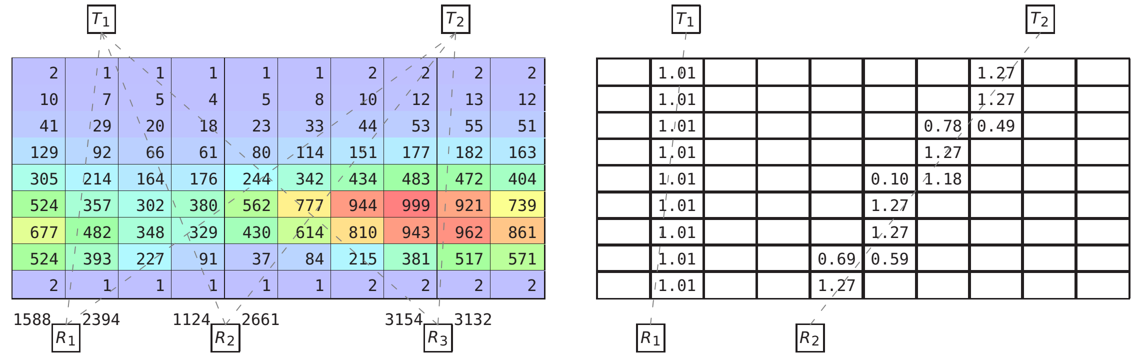

2	1	1	1	1	1	2	2	2	2
10	7	5	4	5	8	10	12	13	12
41	29	20	18	23	33	44	53	55	51
129	92	66	61	80	114	151	177	182	163
305	214	164	176	244	342	434	483	472	404
524	357	302	380	562	777	944	999	921	739
677	482	348	329	430	614	810	943	962	861
524	393	227	91	37	84	215	381	517	571
2	1	1	1	1	1	2	2	2	2

1588 R_1 2394 1124 R_2 2661 3154 R_3 3132

(a) Pixelised parameter and line integrals

	1.01						1.27		
	1.01						1.27		
	1.01					0.78	0.49		
	1.01					1.27			
	1.01				0.10	1.18			
	1.01				1.27				
	1.01				1.27				
	1.01			0.69	0.59				
	1.01			1.27					

(b) Pixel intersection of two ray paths

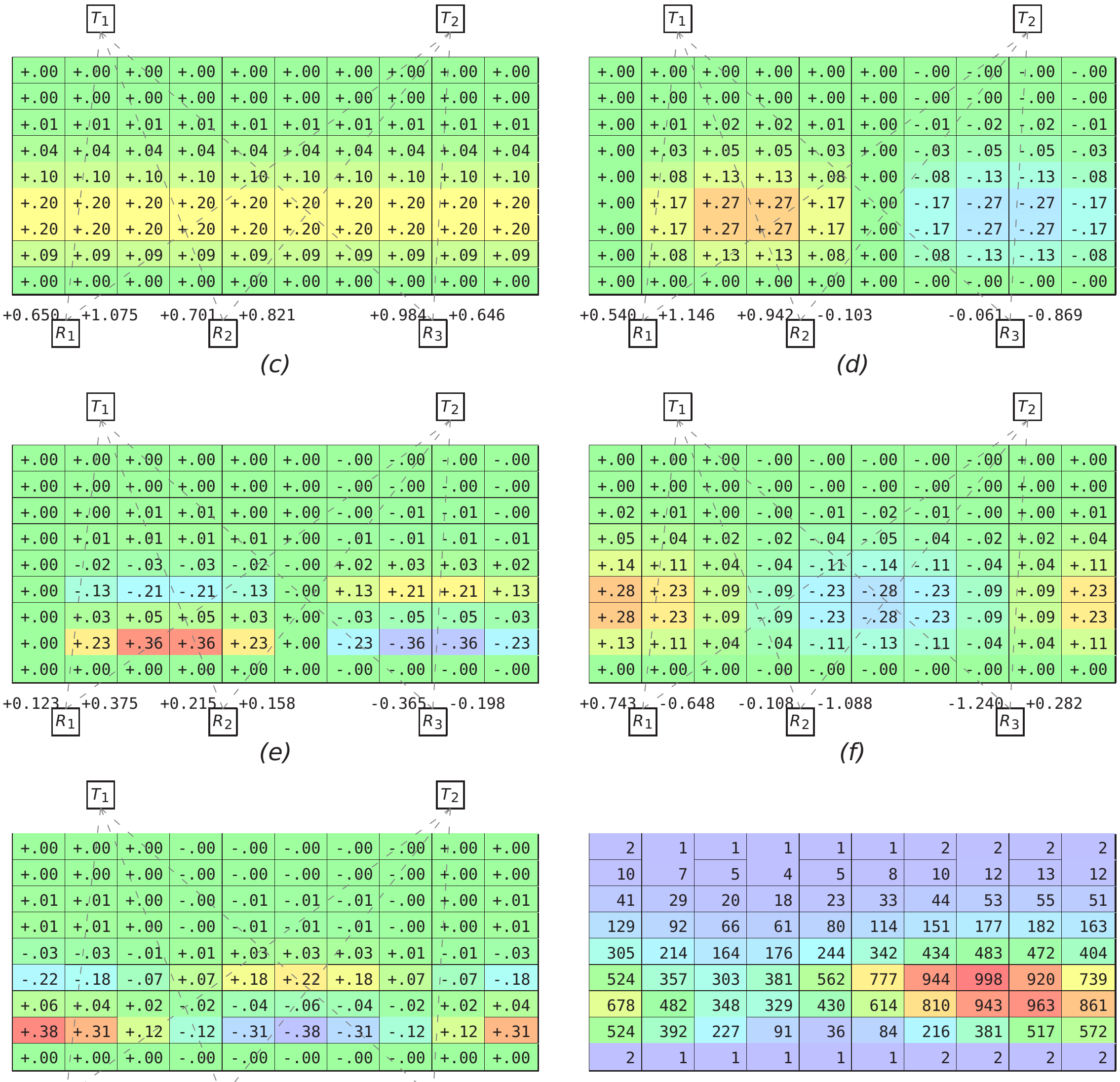

+.00	+.00	+.00	+.00	+.00	+.00	+.00	+.00	+.00	+.00
+.00	+.00	+.00	+.00	+.00	+.00	+.00	+.00	+.00	+.00
+.01	+.01	+.01	+.01	+.01	+.01	+.01	+.01	+.01	+.01
+.04	+.04	+.04	+.04	+.04	+.04	+.04	+.04	+.04	+.04
+.10	+.10	+.10	+.10	+.10	+.10	+.10	+.10	+.10	+.10
+.20	+.20	+.20	+.20	+.20	+.20	+.20	+.20	+.20	+.20
+.20	+.20	+.20	+.20	+.20	+.20	+.20	+.20	+.20	+.20
+.09	+.09	+.09	+.09	+.09	+.09	+.09	+.09	+.09	+.09
+.00	+.00	+.00	+.00	+.00	+.00	+.00	+.00	+.00	+.00

+0.650 R_1 +1.075 +0.701 R_2 +0.821 +0.984 R_3 +0.646

(c)

+.00	+.00	+.00	+.00	+.00	+.00	-.00	-.00	-.00	-.00
+.00	+.00	+.00	+.00	+.00	+.00	-.00	-.00	-.00	-.00
+.00	+.01	+.02	+.02	+.01	+.00	-.01	-.02	-.02	-.01
+.00	+.03	+.05	+.05	+.03	+.00	-.03	-.05	-.05	-.03
+.00	+.08	+.13	+.13	+.08	+.00	-.08	-.13	-.13	-.08
+.00	+.17	+.27	+.27	+.17	+.00	-.17	-.27	-.27	-.17
+.00	+.17	+.27	+.27	+.17	+.00	-.17	-.27	-.27	-.17
+.00	+.08	+.13	+.13	+.08	+.00	-.08	-.13	-.13	-.08
+.00	+.00	+.00	+.00	+.00	+.00	-.00	-.00	-.00	-.00

+0.540 R_1 +1.146 +0.942 R_2 -0.103 -0.061 R_3 -0.869

(d)

+.00	+.00	+.00	+.00	+.00	+.00	-.00	-.00	-.00	-.00
+.00	+.00	+.00	+.00	+.00	+.00	-.00	-.00	-.00	-.00
+.00	+.00	+.01	+.01	+.00	+.00	-.00	-.01	-.01	-.00
+.00	+.01	+.01	+.01	+.01	+.00	-.01	-.01	-.01	-.01
+.00	-.02	-.03	-.03	-.02	-.00	+.02	+.03	+.03	+.02
+.00	-.13	-.21	-.21	-.13	-.00	+.13	+.21	+.21	+.13
+.00	+.03	+.05	+.05	+.03	+.00	-.03	-.05	-.05	-.03
+.00	+.23	+.36	+.36	+.23	+.00	-.23	-.36	-.36	-.23
+.00	+.00	+.00	+.00	+.00	+.00	-.00	-.00	-.00	-.00

+0.123 R_1 +0.375 +0.215 R_2 +0.158 -0.365 R_3 -0.198

(e)

+.00	+.00	+.00	-.00	-.00	-.00	-.00	-.00	+.00	+.00
+.00	+.00	+.00	-.00	-.00	-.00	-.00	-.00	+.00	+.00
+.02	+.01	+.00	-.00	-.01	-.02	-.01	-.00	+.00	+.01
+.05	+.04	+.02	-.02	-.04	-.05	-.04	-.02	+.02	+.04
+.14	+.11	+.04	-.04	-.11	-.14	-.11	-.04	+.04	+.11
+.28	+.23	+.09	-.09	-.23	-.28	-.23	-.09	+.09	+.23
+.28	+.23	+.09	-.09	-.23	-.28	-.23	-.09	+.09	+.23
+.13	+.11	+.04	-.04	-.11	-.13	-.11	-.04	+.04	+.11
+.00	+.00	+.00	-.00	-.00	-.00	-.00	-.00	+.00	+.00

+0.743 R_1 -0.648 -0.108 R_2 -1.088 -1.240 R_3 +0.282

(f)

+.00	+.00	+.00	-.00	-.00	-.00	-.00	-.00	+.00	+.00
+.00	+.00	+.00	-.00	-.00	-.00	-.00	-.00	+.00	+.00
+.01	+.01	+.00	-.00	-.01	-.01	-.01	-.00	+.00	+.01
+.01	+.01	+.00	-.00	-.01	-.01	-.01	-.00	+.00	+.01
-.03	-.03	-.01	+.01	+.03	+.03	+.03	+.01	-.01	-.03
-.22	-.18	-.07	+.07	+.18	+.22	+.18	+.07	-.07	-.18
+.06	+.04	+.02	-.02	-.04	-.06	-.04	-.02	+.02	+.04
+.38	+.31	+.12	-.12	-.31	-.38	-.31	-.12	+.12	+.31
+.00	+.00	+.00	-.00	-.00	-.00	-.00	-.00	+.00	+.00

+0.169 R_1 +0.384 -0.119 R_2 -0.213 -0.190 R_3 +0.064

(g)

2	1	1	1	1	1	2	2	2	2
10	7	5	4	5	8	10	12	13	12
41	29	20	18	23	33	44	53	55	51
129	92	66	61	80	114	151	177	182	163
305	214	164	176	244	342	434	483	472	404
524	357	303	381	562	777	944	998	920	739
678	482	348	329	430	614	810	943	963	861
524	392	227	91	36	84	216	381	517	572
2	1	1	1	1	1	2	2	2	2

(h) Reconstruction

Figure 3.3: 2D Tomography.
(c) to (g) show the mapping functions and corresponding line integrals.

giving the natural generalised inverse matrix $(\mathbf{AX})^{-1}$:

$$(\mathbf{AX})^{-1} = \mathbf{V_{AX}}\,\mathrm{diag}(1/w_{\mathbf{AX}})\mathbf{U_{AX}}^T \tag{3.14a}$$

and the final solution such as:

$$\mathbf{x} \simeq \mathbf{Xw} = \mathbf{X}(\mathbf{AX})^{-1}\mathbf{b} \tag{3.14b}$$

In Equation (3.14a), the reciprocal of the terms in $w_{\mathbf{AX}}$ that are sufficiently small are zeroed to account for the potential degeneracy in **AX** (Press et al., 1992, eq. (2.6.7) and context). Other inversion methods (conjugate gradients, etc...) to solve for Equation (3.13) can also be used.

The reconstruction of **x** is represented in Figure 3.3h. A small residual remains, here because the mapping functions chosen can not give an exact fit to the original problem, but it can also be because of the noise of the line measurements.

3.4 MIDAS

3.4.1 Algorithm

Multi Instrument Data Analysis System (MIDAS) is a software package of modular algorithms that can be used to invert line integral measurements to form 3D time dependent tomographic images. Tomography uses networks of line integral measurements to yield the spatial distribution of the integrated parameter.

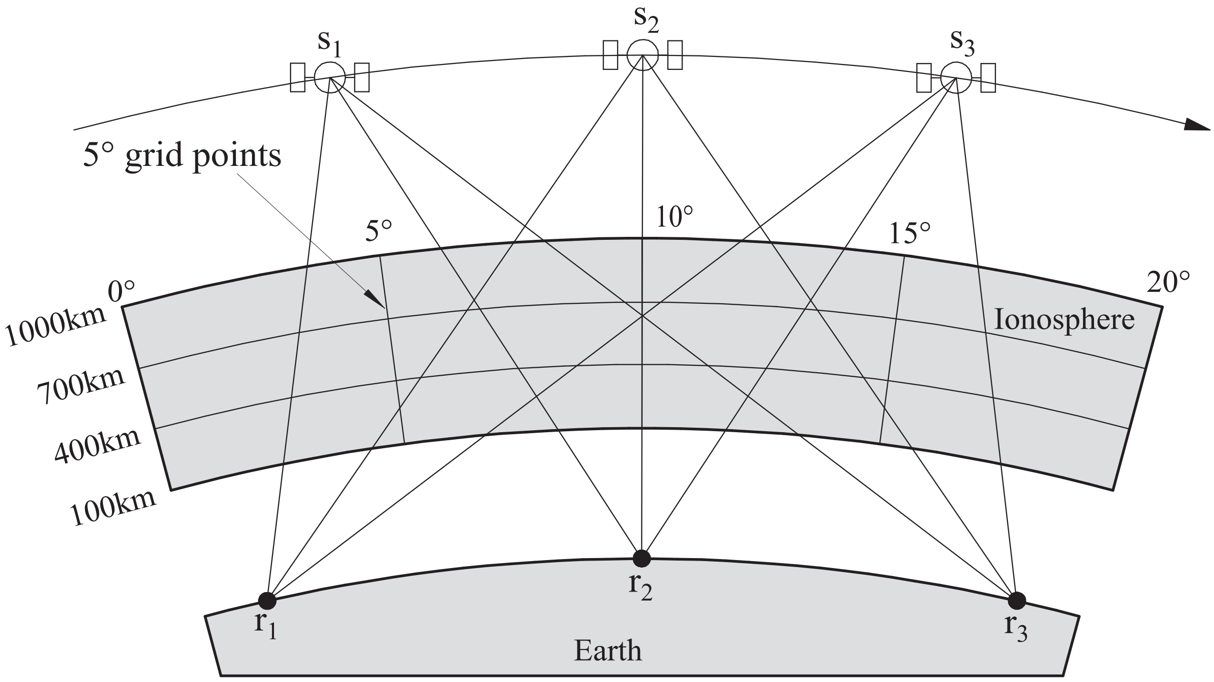

Figure 3.4: Simplified ionospheric tomography geometry, from Meggs (2005, Fig. 3.6)

From Equation (3.9b), the TEC measurements taken from GPS receivers $b_{n,m}$ can be expressed as the sum of the line integral of ED N, along a line from a satellite S_n to a receiver R_m, and of an offset $\Delta b_{n,m}$, due to the integer ambiguity, so that:

$$b_{n,m} = \Delta b_{n,m} + \int_{S_n}^{R_m} N \, \mathrm{d}l \tag{3.15}$$

The first stage of the tomography is to set-up a grid of temporal volume elements called voxels. Figure 3.4 shows how the voxels of the grid and the ray paths intersect with each other. Within each element the integrated parameter (in this case the ion density) is assumed to be constant. The length of each intersection $\mathrm{d}l$ between a transmitter-to-receiver path and an element is computed. For i line integral measurements and j voxels there is the unknown $\mathbf{x}$, a column vector of all the j values of N in the grid, $\mathbf{A}$ an $i \times j$ matrix of all the path lengths $\mathrm{d}l$, $\mathbf{b}$ the column vector of all the i measurements and $\mathbf{\Delta b}$ the column vector for the related integer ambiguities for which Equation (3.15) becomes:

$$\mathbf{Ax} + \mathbf{\Delta b} = \mathbf{b} \tag{3.16}$$

Equation (3.16) can not be solved directly as $\mathbf{A}$ is highly singular and as the problem is ill-defined: the number of unknowns j is much superior to the number of knowns i. However the distribution of N in the ionosphere is smooth and therefore highly cross-correlated, spatially and temporally. Its vertical profiles can be modelled as a weighted sum of a small number of Empirical Orthogonal Functions (EOFs). EOFs for the ionosphere can be obtained from the International Reference Ionosphere (IRI) (Bilitza, 2001) or from a set of ionospheric profile functions, such as Chapman or Epstein (Meggs and Mitchell, 2006, §2). Using a number η of EOFs, a 3D map of the ionosphere can be reduced to η maps of weighting coefficients. As the distribution of N in the ionosphere is also highly cross-correlated in the horizontal directions, these maps themselves may be modelled with spherical harmonics. Regularisation can also be applied to enforce cross-correlation of neighbouring voxels. Mapping must also be applied to take advantage of the fact that the integer ambiguities remain constant for the receiver-satellite pair while the signal lock is properly kept. Equation (3.16) can then be solved, e.g. through an SVD as shows previously with Equations (3.14).

3.4.2 Review

This section is based on a comprehensive review of ionospheric imaging given by Bust and Mitchell (2008).

Earlier work on ionospheric tomography made use of TEC measurements between Low Earth Orbit (LEO) satellites, e.g. the now retired Navy Navigational Satellite System (NNSS), also called Transit, and ground-based receivers. The NNSS was a Doppler-based navigation system. Its satellites had a circular and near polar orbit at 1100 km above the ground and transmitted phase-coherent signals on two frequencies, 150 and 400 MHz. Comparison with ISR observations enabled development of the technique (Pryse et al., 1998; Raymund et al., 1993; Walker et al., 1996). Raymund et al. (1993) showed broad agreement with European Incoherent Scatter Radar (EISCAT) observations of images from inversion with basis functions from IRI, but Walker et al. (1996) showed using basis functions from Chapman profiles gave better agreement. Pryse et al. (1998) compared EISCAT observations with tomographic images from the same NNSS data but obtained with three different inversion algorithms : IRI-initialised Multiplicative Algebraic Reconstruction Technique (MART), Discrete Inverse Theory (DIT) and Quadratic Programming (QP), the same method as MIDAS. The study showed that MART reconstruction is too constrained by its background model to be reliable whereas both DIT and QP are in reasonable agreement with each other and with ISR observations.

Most of the literature mentions that the geometrical coverage is often not advantageous : the fact that, as is the case in this project, all rays cross the ionosphere more or less vertically and that no signal travels through horizontally as is the case with radio-occultation makes the problem a little more ill-defined than it already is. There will also be higher uncertainties on the ED values for voxels in less covered areas, e.g. away from groups of receivers. As suggested by Yin et al. (2004), Yin and Mitchell (2005) compared “images produced with and without the use of radio-occultation data” using ionosondes to evaluate the peak of ED and showed that this improved the image of the ED profile.

The method has however been validated by a number of studies (Bust et al., 2007; Meggs et al., 2005; Spencer and Mitchell, 2007; Yin et al., 2004) many of which showing good agreement with ISR observations. Meggs et al. (2005) and Spencer and Mitchell (2007) both compared MIDAS images with data from the EISCAT in Scandinavia and Yin et al. (2004) compared MIDAS images with data from the Millstone Hill ISR in North America. Meggs et al. (2005, fig.2&3) successfully imaged the main trough and its southern wall in the early afternoon of the geomagnetically quiet day of 7 January 2002 with an earlier version of MIDAS that used spherical harmonics for horizontal regularisation. Spencer and Mitchell (2007, fig.2&3) used a version of MIDAS similar to the latest one with a Kalman filter to successfully image the significantly more challenging fast-moving structures of high ED over the polar cap during the extreme storm of 30 October 2003. Yin et al. (2004, fig.3&4) successfully imaged high ED gradients and ionisation upwelling over the USA, and confirmed the results also with ionosonde data. Bust et al. (2007) compared MIDAS with a fundamentally different ionospheric imaging method called Ionospheric Data Assimilation 3D (IDA3D). Despite their many differences, MIDAS and IDA3D images of 30 October 2003 were in agreement.

Bust et al. (2004) describes IDA3D. It uses a wider range of measurements, satellite probes and ionosondes in addition to TEC from GPS and LEO satellites to ground receivers, as input data. IDA3D also solves with a maximum likelihood method and with a model for regularisation. Bust and Crowley (2007) showed good agreement between IDA3D and Svalbard ISR observations when tracking the movements of high ED patches over the polar cap on the 12 December 2001, a geomagnetically quiet day. The study also revealed that these patches generally originate at latitude slightly higher than 60° when it was previously believed that they originated at mid-latitudes, which appears to be the case only during geomagnetic storms.

Another widely used method greatly simplifies the problem by approximating the ionosphere to a thin-shell. Yeh and Raymund (1991) computed the response to an impulse source function to investigate the limitations of this method. The study showed some limitations of the method were due to the sparse data coverage and the lack of low angle data, as is already the case for full-height tomography. Most of the current ionospheric correction systems, detailed and reviewed in the next section, are based on the thin-shell approximation.

3.5 Current ionospheric correction systems

The idea to map the ionosphere in real time to make corrections has been studied and implemented in various regions of the world. They either take measurements and map the ionosphere, approximating it to a thin shell, or use a model. Most studies on these systems and reviewed in this section compare directly corrections with TEC measurements. Unless stated otherwise, it is not known whether these measurements are carried out with the correction for the receiver P1 to P2 bias, although it is important as Equation (3.10) shows. Unless stated otherwise, these studies unfortunately do not evaluate the impact of their corrections on the positioning.

Most receivers will use the Klobuchar (1987) model unless a Satellite Based Augmentation System (SBAS) is available and the receiver is enabled to use it. Both these systems approximate the ionosphere to a thin shell at 350 km altitude.

3.5.1 Klobuchar

The following subsection is based on Klobuchar (1987) and the quotes come from the same article. It should be noted that the algorithm equations in this article are a summary and that some errors occur in the example calculation. The "algorithm has been implemented in a slightly different form for use with the GPS satellites" and the explanations given in the paper are clarified and confirmed in the description of this slightly different form in the ICD 200c, fig.20-4.

This thin shell model is "designed to give best fit to the large daytime values of monthly average TEC". It does not take into account short term hourly variability of the ionosphere. This model corrects "for approximately 50 percent rms of the ionospheric range error". "The goal of a 50 percent rms correction … was arrived at … as a compromise between number of coefficients … and the realization that even a state of the art ionospheric model, requiring many coefficients, would provide only a 70 to 80 percent rms correction". This project evaluates corrections from the IRI, a state of the art ionospheric model, and the results confirm the above claim.

As the "behavior of TEC in the equatorial and high latitudes is less well known" and because of the large variability of TEC in those region, the Klobuchar model is designed only for mid-latitude regions.

This model is based on an extremely simple thin shell approximation of the ionosphere, where the night-time vertical delay is an all-time all-latitude constant of

5 ns and the day-time vertical delay at each latitude is approximated to a cosine. For this cosine only the amplitude and the period are given, with the phase set for the maximum to be at 14:00 local time. The amplitude and period are given by a third degree polynomial of the latitude. 4 α coefficients are given for the amplitude and 4 β coefficients are given for the period. These 8 coefficients are broadcast by the GPS satellites themselves as part of the C code.

Klobuchar tests corrections from his model with “actual TEC”, but see the comment at the beginning of this Section 3.5, during the solar maximum period of 1968-1970 and claims that the tests show that the “goal of a 50 percent rms ionospheric correction has been met”. This project also evaluates corrections from the Klobuchar model and the results also confirm the above claim.

“Coefficients transmitted by the GPS satellites are updated once each ten days, or sometimes more frequently, if the five day running mean solar flux changes by a large amount during that period of time.” This means that the coefficients are not updated for storm days, as shown for example on Figure 3.5. The author recommends users who “cannot tolerate” “those infrequent times when a large deviation from average ionospheric behavior will be encountered” to “seriously consider opting for a dual-frequency GPS receiver”.

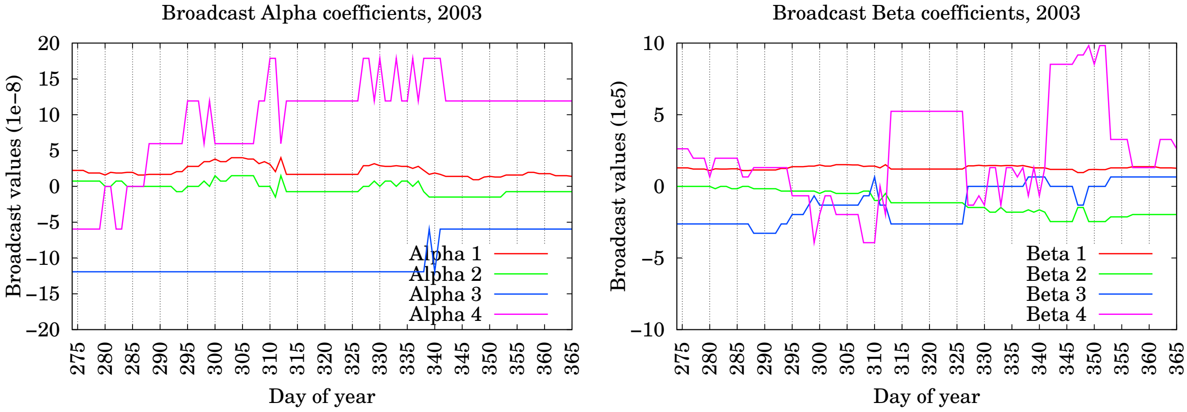

Figure 3.5: Evolution of the broadcast Klobuchar coefficients from 1 Oct to 31 Dec 2003
There was no significant updates to the Klobuchar broadcast coefficients for the two major ionospheric storms during that period, on days 302-303 and 324.
The broadcast Klobuchar coefficients are recorded and archived by the IGS (see “Broadcast” on `http://igscb.jpl.nasa.gov/components/prods.html`).

3.5.2 Satellite Based Augmentation Systems

SBASs have been implemented in various regions of the world, all working in a similar way. The Wide Area Augmentation System (WAAS) is available in North America, European Geostationary Navigation Overlay System (EGNOS) is the European system, while Multi-functional Satellite Augmentation System (MSAS) operates in Asia.

According to the real-time data available at the time of writing (`http://www.nstb.tc.faa.gov/IGPDelays.htm`), the grid spacings for WAAS are 5° in latitude and longitude from 5° to 60° North, 5° in latitude and 10° in longitude from 65° to 75° North and 30° in longitude at 85° North. See also FAA (2001, Tab.12). The WAAS is specified to give a position within a 7.6 m accuracy both horizontally and vertically in 95% of cases (FAA, 2001, Tab3.2-2).

A brief description of the WAAS is given by Komjathy et al. (2005, eq.4 and context). A network of receivers is used to carry out Slant TEC (STEC) measurements with a method similar to 3.6.3, correcting for interfrequency biases. Each STEC measurement is projected to a pierce point on the 350 km shell and converted to Vertical TEC (VTEC) measurement. For each grid point, an average of the VTEC of the surrounding pierce points is used as the VTEC value for the grid point. Also, the variance of the measured VTEC is used to derive an uncertainty on the grid point VTEC and this uncertainty is broadcast with the VTEC (Sparks et al., 2005, §I). This means that if, e.g. during a storm, the measurements show the thin shell approximation to be inappropriate, higher uncertainty values will be given, progressively informing the receivers not to use the affected satellites. Aquino et al. (2005) also notes that a SBAS can be severely affected by scintillation, as this can disable STEC measurements, in particular those located close to areas of high scintillation, like EGNOS, which covers the auroral region of Northern Europe. Komjathy et al. (2005) argues “that in the equatorial region the dominant error source for the WAAS planar fit algorithm is the inherent spatial variability of the equatorial ionosphere”. However, he fails to note that the important residuals could be explained by the thin shell approximation being invalid as, being magnetic-field-aligned, the ED peak has a height varying from 500 to 250 km in 5° of latitudes (see again Andreeva et al., 2000, fig.1 and Yeh et al., 2001, fig.1).

Performance Analysis Reports (PANs) are written quarterly for the WAAS (`http://www.nstb.tc.faa.gov/DisplayArchive.htm`). They show that, “only when all WAAS corrections (fast, long term, and ionospheric) for at least 4 satellites are available”, the positioning error is typically 1 m both horizontally and vertically. As mentioned above, it must be noted that corrections are not always available, especially during storms.

As archives of SBASs corrections do not appear to be public available, most studies of it use simulations to evaluate their performances. Komjathy et al. (2005) finds his simulation of WAAS gives ionospheric delays within 2 m of his interfrequency-biases-corrected TEC measurements on the 28 October 2003, a quiet day of solar maximum, and within 25 m of his TEC measurements on the following two days, which were extreme storm days.

Theoretical studies of the advantages of using full-height rather than thin-shell images have been carried out with MIDAS by Meggs and Mitchell (2006) for vertical delay and by Smith et al. (2008) for slant delay. Meggs and Mitchell (2006) evaluated the VTEC errors of thin-shell and full-height images by carrying out the tomography of the IRI for quiet and storm days of the solar maximum year 2001. The study showed the VTEC from full-height images are in error of around 5%, which was three times better that the VTEC from thin-shell images. It must be noted that a real ionosphere will be much more complex than the one given by the IRI, so the uncertainties must be expected to be higher when working on real data.

3.5.3 International Reference Ionosphere

The IRI (`http://iri.gsfc.nasa.gov/`) is a popular empirical model of the ionosphere. It is a joint project of the Committee on Space Research (COSPAR) and the International Union of Radio science (URSI) that has the goal to "establish an international standard model of the ionospheric densities temperatures, and drifts". It has been the subject of a lot of research, as its history by Reinisch and Bilitza (2004) shows, and it "is continually upgraded as new data and new modelling approaches become available" (Bilitza and Reinisch, 2008). The four latest versions, 90, 95, 2001 and 2007, are freely available (`ftp://nssdcftp.gsfc.nasa.gov/models/ionospheric/iri/`).

The 95 version has been integrated in MIDAS since its earliest version. It has been found that the integration into MIDAS of the 2007 version (Bilitza and Reinisch, 2008) was more difficult and therefore has been done only very recently. It has been found that the 2001 version was easier to integrate into MIDAS and has been used instead in this project. It has been described by Bilitza (2001). The following paragraph is based on this article and the quotes come from this article.

The IRI gives an ED for any point in the ionosphere below 2000 km of altitude. At low altitudes, in the E region, it uses geodetic coordinates because of "the close coupling to the neutral gas (high collision frequency) in the lower ionosphere". It is also where "strong solar control is best described with the solar zenith angle". At higher altitudes, in the F region and above, it uses geomagnetic coordinates because of "the coupling to the magnetic field line in the middle and topside ionosphere", as "transport processes along magnetic field lines redistribute the plasma". The variations of the 11-year solar cycle should ideally be reproduced from EUV emission intensity, but EUV "cannot be observed at the ground". Instead "the sunspot number ... and the solar radio flux at 10.7 cm wavelength (F10.7)" are used "since both can be observed from the ground". Correlations have shown that F10.7 is best below the F peak and that the sunspot number is best above. The IRI uses "the 12-month running mean" of these indexes as correlation is better for 12-month running mean than for "monthly and daily averages". The indexes are regularly updated from measurements. For the future, forecasts are used, although it must be noted that the "uncertainties of such forecasts naturally increase with the time span for which the forecast is required". As this projects uses the IRI for forecasts, the model was run in forecast mode.

The IRI has already been proposed for ionospheric corrections (Komjathy et al., 1998; Orús et al., 2002). Orús et al. (2002) compared IRI VTEC with precise measurements from dual-frequency space-to-ground radar carried out during the TOPEX mission and showed the IRI corrects for 60% of the ionospheric delay. Komjathy et al. (1998) use the IRI with a plasmasphere model to derive the ionospheric delay between a LEO satellite and the ground from TEC measurements between GPS satellites and ground receivers. The corrections were found to be accurate within 10 TEC Unit (TECU).

3.5.4 Ionospheric prediction

For real-time application, this project proposes to use a modified version of the prediction algorithm detailed in Dear (2007). We obtain, for a given location, N'_1 the ED at a time t_1 from N'_0 the ED from a tomographic image at a time t_0 and from N_0 and N_1 the EDs from a model at times t_0 and t_1 respectively :

$$N'_1 \approx \frac{N_1}{N_0} N'_0 \tag{3.17}$$

Among many factors, the ionosphere depends on randomly fluctuating Solar radiations and on turbulent Earth winds (see Section 3.1.1). This means it varies significantly within little time and in a way that is difficult to predict. Therefore Equation (3.17) is only valid when the difference between t_0 and t_1 is small, generally less that one hour ahead.

3.6 Ionospheric corrections

Equation (3.6b) shows the TEC can either be calculated if the ED and the ray paths are known or measured if pseudorange observations are available for at least two frequencies.

3.6.1 Ionosphere-corrected pseudorange

In this project the following method to compensate for the ionospheric delay is proposed.

We can compensate for the ionospheric delay If^{-2} by taking the ionosphere-corrected pseudorange P'_0, similarly to Equation (3.7a) :

$$P'_0 = P_1 - If_1^{-2} \tag{3.18}$$

The ionospheric delay term I is here calculated using Equation (3.6c), with N the ED from a model, e.g. the IRI (Section 3.5.3), a tomographic image (Section 3.4) or a prediction (Section 3.5.4) and $\mathrm{d}l$ the intersection of the voxel with the ray corresponding to the pseudorange.

The computation of the ray-path to voxel intersection shows when the signal has travelled through a part of the ionosphere that is outside the map. The pseudoranges corresponding to the rays that have travelled entirely or partially through a part of the ionosphere that is outside the map are taken out of the positioning computation. The remaining pseudoranges correspond to ray paths for which the TEC can be calculated, because the ED N is known for the entire part of the path that intersects with the ionosphere. The ray-paths to voxel intersections $\mathrm{d}l$ are then multiplied by the ED of the corresponding voxels N'. The total gives the ray path integral $\int N' \mathrm{d}l$.

3.6.2 Unfiltered Ionosphere-free pseudoranges

This subsection is based on Allain and Mitchell (2009a, "Pseudoranges" subsection).

The unfiltered dual-frequency position is computed from unfiltered ionosphere-free pseudoranges, here called P_ϵ. It is itself computed from two observables P_1 and P_2 as explained below.

Neglecting the importance of the noise term in Equation (3.7) gives:

$$P_\epsilon \simeq \frac{P_1 f_2^{-2} - P_2 f_1^{-2} - \epsilon_1 f_2^{-2} + \epsilon_2 f_1^{-2}}{f_2^{-2} - f_1^{-2}} \tag{3.19}$$

Comparing Equation (3.19) with Equation (3.7) shows the unfiltered dual-frequency pseudorange P_ϵ is about three times noisier than either of the single-frequency pseudoranges P_1 or P_2. Indeed, if we consider ϵ_1 and ϵ_2 to be uncorrelated and both with a Gaussian distribution of the same Standard Deviation (SD) of $\Delta\epsilon$, as $-\epsilon_1 f_2^{-2} + \epsilon_2 f_1^{-2}$ has a SD of:

$$\sqrt{\left(-f_2^{-2}\Delta\epsilon\right)^2 + \left(f_1^{-2}\Delta\epsilon\right)^2} = \Delta\epsilon\sqrt{f_2^{-4} + f_1^{-4}}$$

then the SD $\Delta\epsilon_\epsilon$ of the resulting noise on P_ϵ is such as:

$$\Delta\epsilon_\epsilon = \frac{\sqrt{f_2^{-4} + f_1^{-4}}}{\left|f_2^{-2} - f_1^{-2}\right|}\Delta\epsilon \simeq 3.0\,\Delta\epsilon \tag{3.20}$$

This suggests that unfiltered dual-frequency will be more vulnerable to the uncorrelated part of the noise, which includes multipath.

3.6.3 Phase-filtered Ionosphere-free pseudoranges

Fitting Equation (3.9b) into Equation (3.9a) as explained in Section 3.2.3 gives:

$$\frac{L_1 f_2^{-2} - L_2 f_1^{-2}}{-f_1^{-2} + f_2^{-2}} = P_0 + \frac{n_1\lambda_1 f_2^{-2} - n_2\lambda_2 f_1^{-2}}{-f_1^{-2} + f_2^{-2}} \tag{3.21a}$$

$$P_1 - I f_1^{-2} = P_0 + \epsilon \tag{3.21b}$$

$$L_1 + I f_1^{-2} = P_0 + n_1\lambda_1 \tag{3.21c}$$

Again, Equation (3.21b) gives P_0 with a noise term and Equation (3.21c) gives P_0 with an offset term. P_0 is, as in Section 3.2.3 for I, computed by fitting Equation (3.21c) into Equation (3.21b) with a similar weighted mean.

3.7 Conclusion

In this Chapter different methods to compensate for the ionospheric delay have been explained. The proposed new method that will be subsequently tested here uses 3D maps of ED. Current methods that are being implemented into ionospheric correction systems, such as SBASs, approximate the ionosphere to a thin shell. However it is known that simple shell approaches are not adequate either for regions of the Earth where the ED structure is complex, at high latitudes and at the equatorial regions (see Section 3.1.1), or on geomagnetic storm days (see Section 3.1.2). The ideal situation is to use pseudorange and phase observations on two frequencies but this method is clearly not available to single frequency receivers and requires calibration even for a fixed receiver. It has been found that the unfiltered dual-frequency measurement of the ionospheric delay has a typically 1 m peak-to-peak noise associated with it. Here the unfiltered and phase-filtered dual-frequency observations are used as a reference to evaluate the proposed new method from MIDAS in the subsequent chapters.

Chapter 4

Methods

The aim of this Chapter is to detail the methods to test the navigation accuracy for various ionospheric corrections. The demonstration is made through a comparison between navigation solutions that are each performed using a different ionospheric correction: (1) no correction (2) Klobuchar model (3) IRI model (4) near-real-time thin-shell images (5) near-real-time full-height images (6) forecast full-height images (6) broadcast forecast full-height images (7) unfiltered dual-frequency (8) phase-filtered dual-frequency.

In the case of real-time imaging there is a latency involved in the data collection and the image production and transmission. Thus the distinction between the forecast and the near real time imaging is to compare different latencies to allow for the data collation, calculations and transmission essential for the implementation of a correction system. The broadcast images are intended to be compressed versions of the forecast and are used to assess the impacts of compression.

The phase-filtered dual-frequency result is a benchmark that shows the best position that can be achieved at that instant without time averaging, whereas the unfiltered dual-frequency is of interest, for example using a moving receiver and not assuming phase continuity.

The material in this Chapter is in part published in Allain and Mitchell (2009a,b). The grid and inversion settings for the various images are given in Section 4.1. The different pseudorange processings and satellite ephemeris calculations, to be carried out before the navigation solution, are detailed respectively in Sections 4.2 and 4.3. The statistical processing of the navigation solutions was carried out according to a method adapted to this project, as explained and detailed in Section 4.5.

4.1 Map settings

Two studies were made, one each for a different area of interest, i.e. Europe and North America. The same grid was used for the IRI model and the full-height images: near-real time, forecast and broadcast. The areas of coverage were extended far beyond the boundaries of the areas of interest to allow the calculation of the TEC even for low elevation rays.

For Europe the grid was centred at 50°N 15°E and for North America the grid was centred at 40°N 100°W allowing for a similar pixel size and shape to cover the area

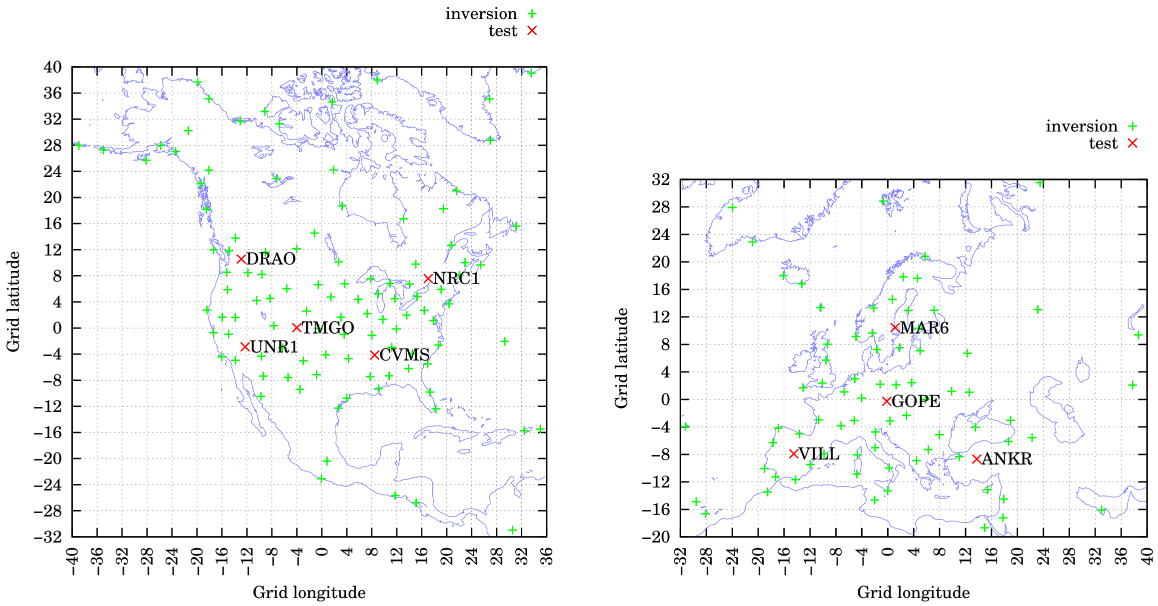

(a) North America (b) Europe

Map source: `http://rimmer.ngdc.noaa.gov/mgg/coast/getcoast.html`

Figure 4.1: Location of the test sites (×) and of the sites used for imaging (+)

of study (Spencer and Mitchell, 2007). For both areas the ranges were in latitude from -44° to +44° in steps of 4° (south to north), in longitude from -44° to +44° in steps of 4° (west to east). The altitude range, for the 3D grid of the full-height images, was from 100 km to 1500 km in steps of 50 km. The altitude of the thin-shell was 350 km, for coherence with the WAAS (see Section 3.5.2).

MIDAS uses ED basis profiles to reduce the number of unknowns (see Equation (3.13) and Section 3.4.1). The same set of basis profiles as Meggs and Mitchell (2006) were used in the vertical domain. A range of ED profiles were generated from Epstein functions. The first three orthonormal basis functions of this range of ED profile were used for the vertical mapping of the ED profiles of the MIDAS maps. MIDAS also uses regularisation. The inversions were stabilised in the horizontal domain with a set of regularisation factors preventing departure from a linear gradient, i.e. constant spatial and temporal gradients were allowed, but variations of gradients were discouraged.

4.2 Pseudorange processing

4.2.1 Stages

A number of parameters have been neglected during the processing of pseudoranges. In particular, Equation (2.23c) gives an uncertainty of $\Delta T_{\phi,h} \leq 0.53\,\mathrm{m}$ on the tropospheric delay correction. Relativistic effects, noise and multipath have also not been corrected for. As receiver clock biases are calculated for some stations by the IGS, it is possible to remove the largest terms in the pseudorange an obtain a residual to evaluate the quality of the corrections. An example has been done for station BRUS on Figure 4.2.

First, the main terms, geometric distance, receiver clock bias and satellite-specific clock bias, have been subtracted from the pseudorange, giving the sum of mainly Sagnac distance, atmospheric delays and satellite relativistic clock bias on Figure 4.2a. The general pattern resembles that of the Sagnac delay (see also Figure 2.10), the most important of the terms to be corrected for. This residual also decreases as the satellites rise and increases again as it sets. It ranges from -15 m to more than 50 m. The pseudoranges can not be used when such a residual remains : it would greatly corrupt the positioning. Corrections need to be applied.

Then correcting for the largest term the Sagnac distance on Figure 4.2b and for the satellite relativistic clock bias (see also Figure 2.8) we are left with mainly the atmospheric delay on Figure 4.2c. This residual decreases by at least 10 and at most 20 m as the satellites rise and then increases by a similar amount as the satellites set : when the satellites are close to the horizon their signals travel through more atmosphere so are more delayed and when the satellites are high in the sky their signals travel through less atmosphere so are less delayed. The atmospheric delay is strongly elevation dependant, like the terms it is made of : the tropospheric and ionospheric delays.

Removing the tropospheric delay (see also Figure 2.6) on Figure 4.2d we are left with mainly the ionospheric delay. This delay is elevation dependant and has a strong daily cycle, as has already been shown on Figure 3.2 and detailed in its comments. A change of scale has been made between Figure 4.2d and Figure 4.2e to highlight the details of the residual. Removing the tropospheric delay measured with the method detailed in Section 3.6.2 amplifies the noise, as shown on Figure 4.2e. Carrying out phase filtering as explained in Section 3.6.3 considerably smooths the residual, although it still leaves an average around 1.5 m. This residual can be explained as follows : taking the multipath as a uniformly random quantity between 0 and 1 m (see again Braasch, 1994, §II.D.2 and fig.1), its average is :

$$\epsilon = 0.5\,\mathrm{m} \tag{4.1a}$$

and as the noise is amplified, with Equation (3.20) this gives :

$$\frac{\sqrt{f_2^{-4}+f_1^{-4}}}{\left|f_2^{-2}-f_1^{-2}\right|}\epsilon \simeq 3.0\times 0.5 = 1.5\,\mathrm{m} \tag{4.1b}$$

This residual explains the error on the phase-filtered dual-frequency benchmark positioning throughout Chapter 6 and Chapter 7.

4.2.2 Compared ionospheric corrections

In order to implement calculations for the single-frequency positioning with no ionospheric correction the P1 code was extracted from the RINEX file. Corrections were made for the Sagnac effect and the satellite relativistic clock bias in accordance with Ashby and Spilker (1995). The tropospheric delays were estimated from receiver altitude and satellite elevation using the approach of Spilker (1994). These

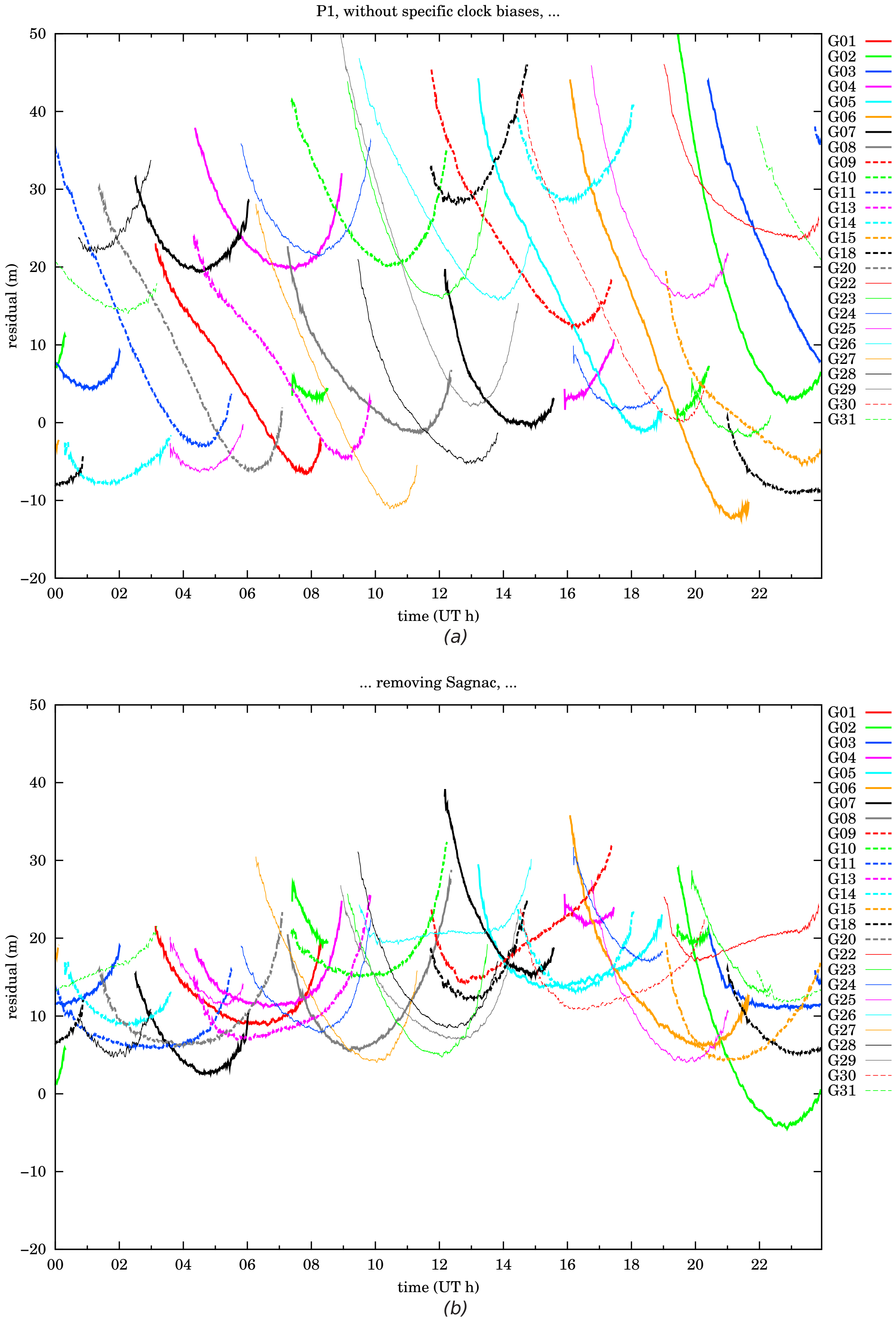

P1, without specific clock biases, ...

(a)

... removing Sagnac, ...

(b)

Figure 4.2: Stages of pseudorange processing for BRUS on 13 Oct 2002. This station is located in Brussels, hence its name, and is managed by the Royal Observatory of Belgium (see `ftp://garner.ucsd.edu/pub/docs/site_logs/brus.log`). Relativistic delays, ...

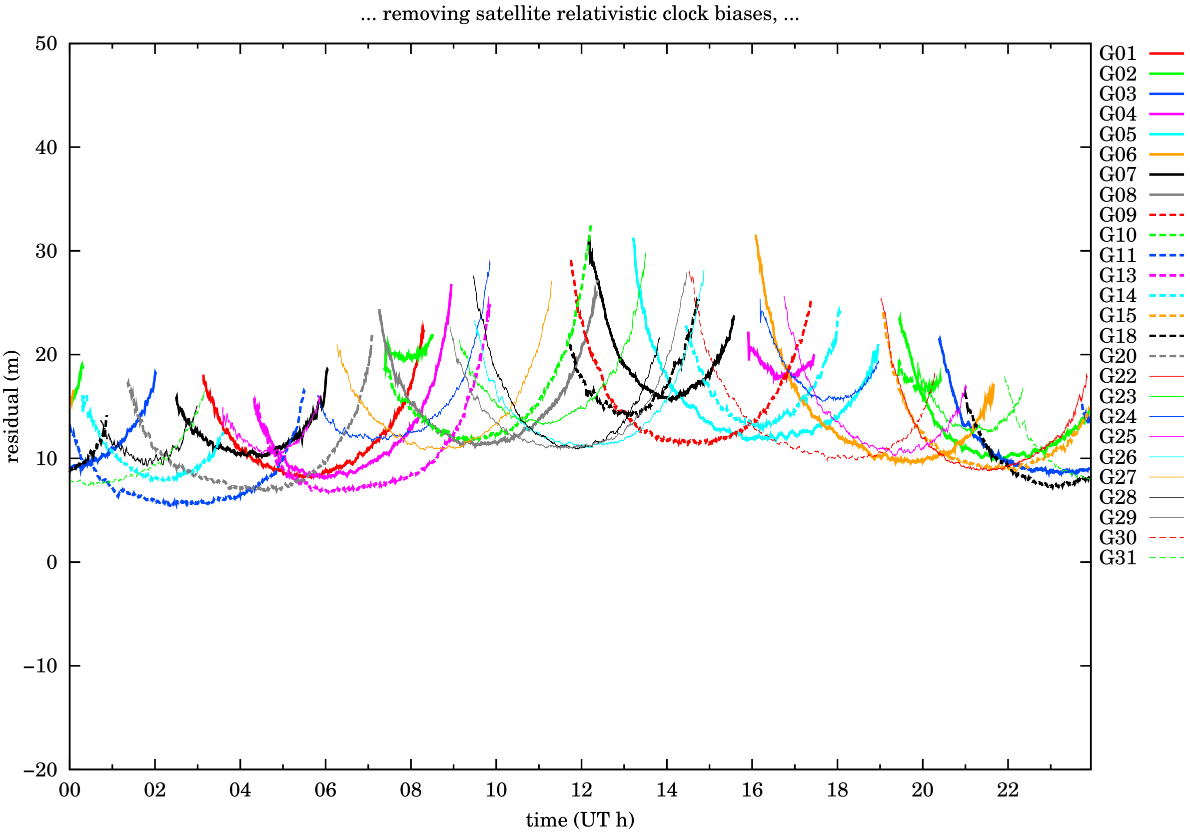
... removing satellite relativistic clock biases, ...

(c)

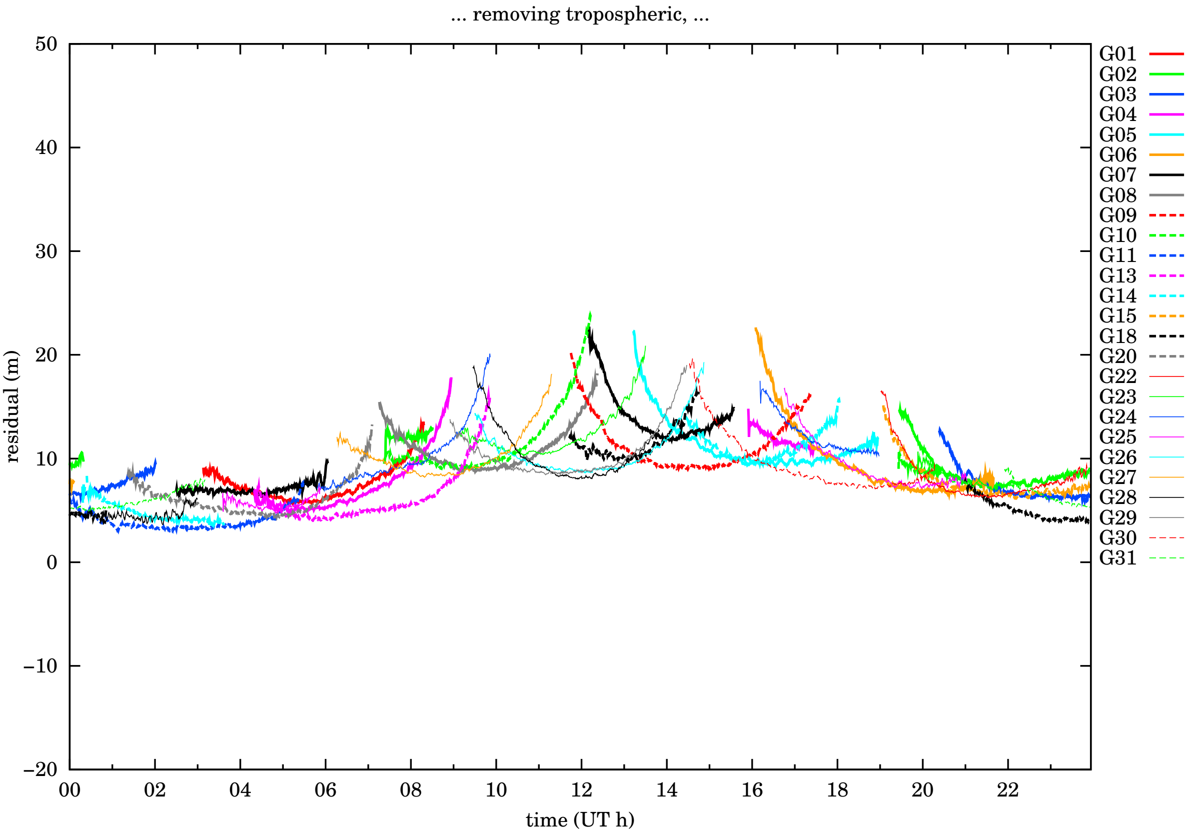
... removing tropospheric, ...

(d)

Figure 4.2: ... atmospheric delays ...

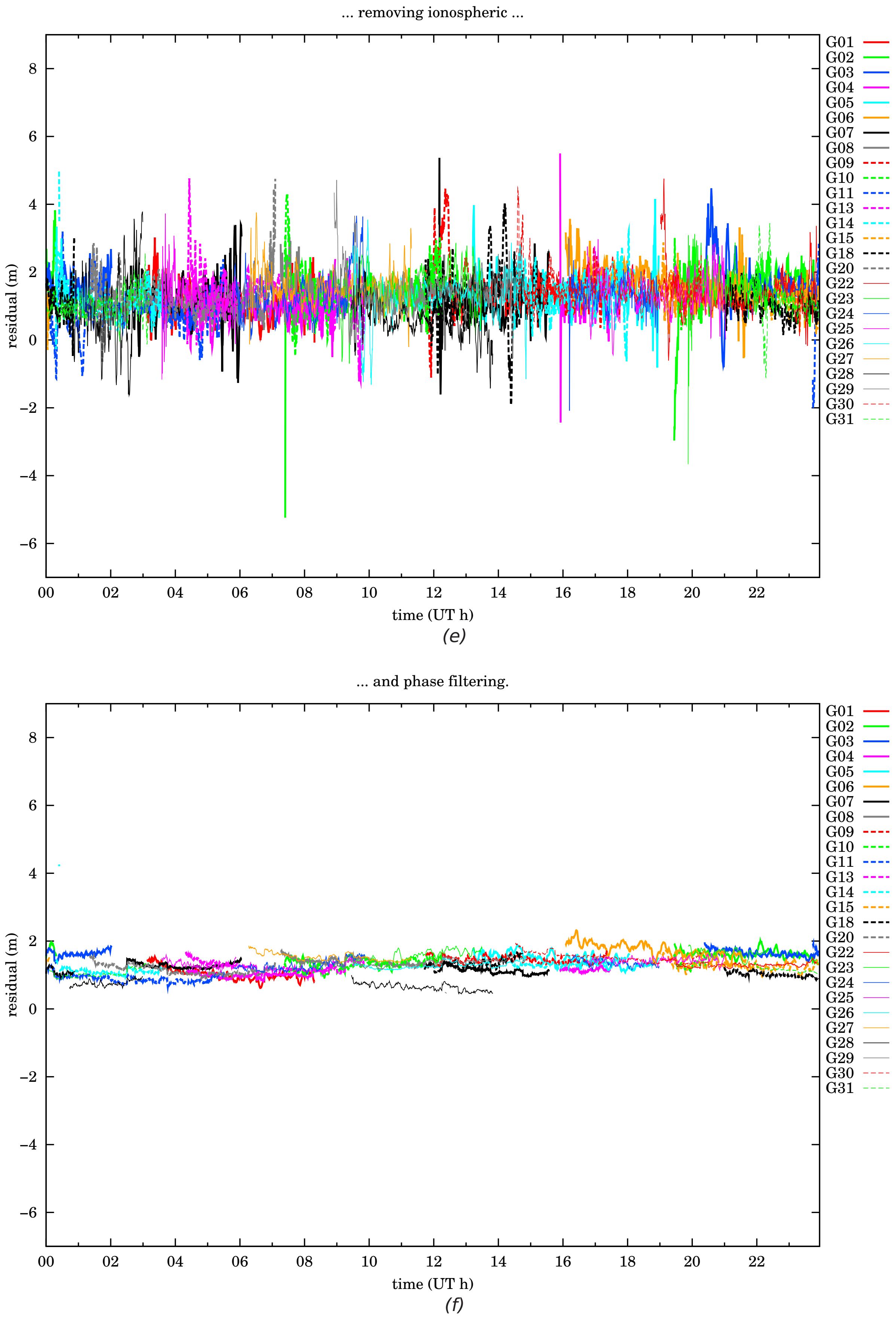

Figure 4.2: ... and phase filtering.

corrections resulted in a set of partially corrected pseudorange observations for each site at the maximum sample period of the IGS data, 30 s. The receiver position was then calculated using a least-squares estimate applied to the corrected pseudorange observations. At this stage no account was taken of the ionosphere and thus this constituted the first method, the results of which are labelled 'uncorrected'. The remaining approaches, each accounting for the ionosphere, are now described below.

The second method was to use the Klobuchar model (see Section 3.5.1). The results from this model are labelled 'Klobuchar'. The third method (labelled 'IRI') was to use the IRI 2001 model (see Section 3.5.3). This provides a full 3-D description of the ED on a global scale assuming knowledge of the date, time and solar output. This model is not currently used for GPS ionospheric corrections on a real-time basis although it could be applied to the system if the model were embedded into a GPS receiver and its parameters were broadcast. The ionospheric corrections were calculated using a forward integration through the model along slant paths to estimate the ionospheric delay to the L1 signal. The fourth method was to use MIDAS. The version of the algorithm described in Mitchell and Spencer (2003) was implemented here with upgrades described in Spencer and Mitchell (2007). The input data came from dual-frequency receivers. Their distribution across and around Europe, shown in Figure 4.1b, and North America, shown in Figure 4.1a, is representative of those available in near-real time. A forecast to real-time (up to 40 minutes ahead) was then implemented as explained in Section 3.5.4. These results are labelled 'forecast'. This forecast was also compressed as explained in Section 5.2. These results are labelled 'broadcast'. For further comparison a non-forecasted near-real-time result is shown, labelled 'full-height' or 'near real-time'. MIDAS in thin-shell mode was also used. These results are labelled 'thin-shell'.

These ionospheric corrections for single-frequency positioning were finally compared against dual-frequency benchmarks. The unfiltered dual-frequency results (see Section 3.6.2) and the phase-filtered dual-frequency results (see Section 3.6.3) are respectively labelled 'dual' and 'filtered dual'.

4.2.3 Absolute pseudoranges

As shown previously, the ionosphere-free pseudorange or ionosphere-corrected pseudorange or uncorrected pseudorange P is itself made of other terms : r the geometric range, r_s the Sagnac bias, $\Delta_s t$ and $\Delta_r t$ the satellite and receiver clock biases, c the speed of light in vacuum and $T_{\phi,h}$ the tropospheric delay :

$$P \simeq r + r_s + c(\Delta_r t + \Delta_s t) + T_{\phi,h} \tag{4.2a}$$

$$\text{giving} \quad P^* = r + c\Delta_r t \simeq P - r_s - c\Delta_s t - T_{\phi,h} \tag{4.2b}$$

Equation (4.2b) gives the absolute pseudorange P^* to put into the least squares pseudorange calculation of Equation (2.11). Equation (2.27d) gives r_s the Sagnac bias. Equation (2.24) gives $\Delta_s t$ the satellite clock bias and Equation (2.25) gives $\Delta_s^1 t$ its eventual single frequency offset. Equation (2.22) gives $T_{\phi,h}$ the tropospheric delay.

The calculations of all of these quantities as well as the solution of the pseudo-range, see Equation (2.11), require that the position and speed of the satellite is known. Their computation is detailed in Section 4.3.

4.3 Satellite position and velocity

The IGS ephemeris are, according to Jefferson and Bar-Sever (2000) : “arguably at least an order of magnitude more accurate than the broadcast ephemerides”. They are also freely available (IGS, 2005) and have been used as is detailed in the following sub-sections.

4.3.1 Antenna offsets

The IGS ephemeris gives the position of the centre of mass of the satellites S' (Kouba and Héroux, 2001; Kouba, 2003, §5.1.1). The antenna offsets have been calculated by Schmid et al. (2007) and are freely available (Schmid). Horizontal satellite antenna offsets $\Delta_h S$ are extremely complicated to take into account but they are up to ≤279 mm and their impact ΔR on the range is :

$$\Delta R \leq R/S \times \Delta_h S \quad \text{giving} \quad \Delta R \leq 67\,\text{mm} \tag{4.3}$$

so can be neglected. Taking $\Delta_v S$ the vertical component of the antenna offset and $\overrightarrow{S'}$ the position of the centre of mass of the satellites, we have $\overrightarrow{S}$ the position of the antenna such as :

$$\overrightarrow{S} \simeq \frac{S' - \Delta_v S}{S'} \overrightarrow{S'} \tag{4.4}$$

4.3.2 Time of transmission and trigonometric interpolation

The IGS ephemeris gives the position of the satellites in the ECEF frame once every 15 min. The precise coordinates of the antenna at the time of transmission t_t must be then be interpolated from surrounding values from the ephemeris and from t_t. The time of transmission t_t is contained in the signal data but is not recorded explicitly in the RINEX file (Gurtner, 2001). Trigonometric interpolation was chosen for a fine interpolation. An iteration process is also carried out to find the time of transmission t_t.

The accuracy of the different interpolation methods was evaluated. A set of positions were interpolated for times between the times for which the ephemerides are published. From this set of positions, a second set of positions was reverse interpolated to the times for which the ephemerides are provided. The half of the difference between the original values and those obtained from the second interpolation is used as the estimate of the interpolation error.

Interpolation of orbits can be computed using polynomial interpolation or trigonometric interpolation. Schenewerk (2003) shows that trigonometric interpolation gives the most accurate results with the least coefficients. By evaluating the spline method as explained in the previous paragraph it has been found that it gives results in error of around 25 m RMS. By evaluating in the same way the trigonometric interpolation with 4 harmonics in the ECEF frame :

$$\overrightarrow{S} \simeq \sum_{i=1}^{4} \overrightarrow{A_i} \cos i\Omega t + \overrightarrow{B_i} \sin i\Omega t \tag{4.5}$$

it has been found that it gives the best results with an uncertainty of around 0.04 m RMS with a maximum of 0.15 m.

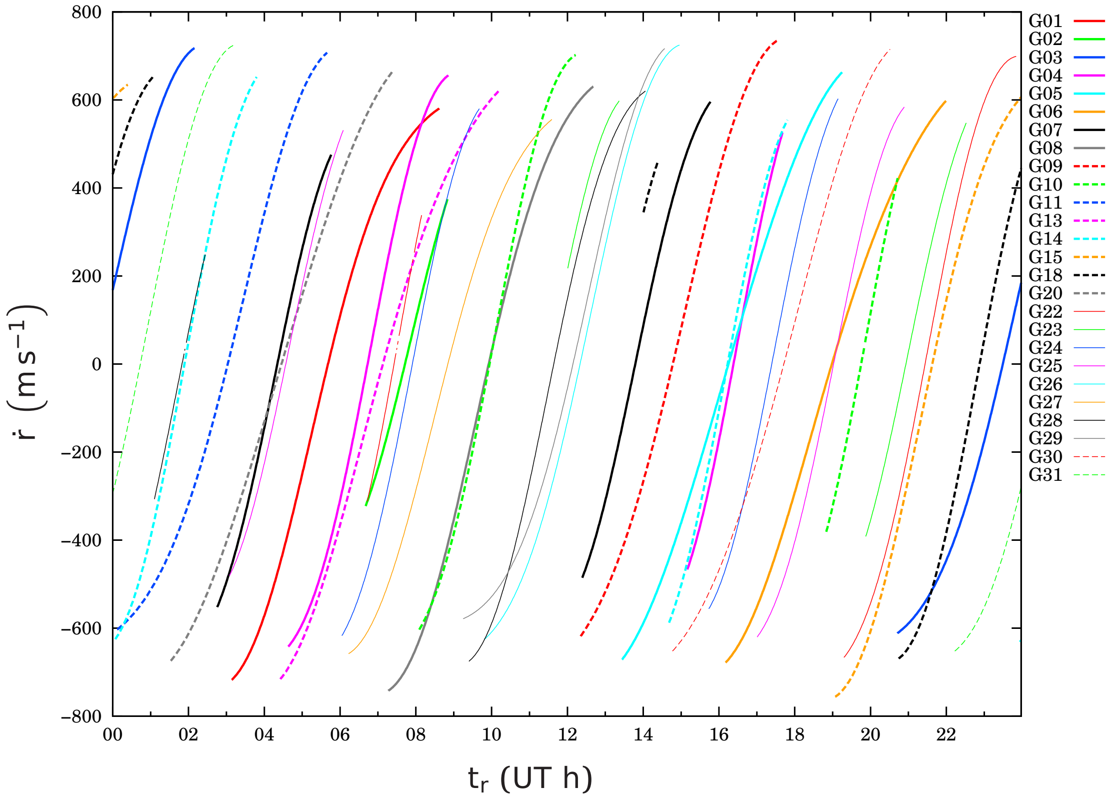

Figure 4.3: Speed of recession of the satellites $\dot{r}$ observed from GOPE on 13 Oct 2002.

The time of transmission can be calculated from t_r the time of reception, which is recorded in the RINEX file, and from $RS \equiv r$, the distance from the satellite S to the receiver R :

$$t_t = t_r - c^{-1} r \tag{4.6}$$

The range r can be calculated from the coordinates of the receiver R and from the coordinates of the satellite S. R is considered to be known, but S is not as it is a function of the transmission time t_t. Therefore, iteration is necessary to solve for the satellite position S. The speed of approach, i.e. the rate at which the distance between a satellite and a receiver changes, is $|\dot{r}| < 800\,\mathrm{m\,s^{-1}}$, as shown in Figure 4.3. The uncertainty on the range Δr has an influence on the uncertainty of the transmission time Δt_t :

$$\Delta t_t < c^{-1} \Delta r \tag{4.7}$$

and the uncertainty of the transmission time Δt_t has itself an influence on the uncertainty of the range Δr :

$$\Delta r = |\dot{r}|\,\Delta t_t \tag{4.8}$$

Each iteration then multiplies the uncertainty on the range by $c^{-1}\,|\dot{r}| < 2.7{\cdot}10^{-6}$. The computation therefore converges quickly toward the solution.

The range r between a satellite and a receiver is between $20.2{\cdot}10^{6}$ m and $26.6{\cdot}10^{6}$ m, or :

$$r = (23.4 \pm 3.2){\cdot}10^{6} \tag{4.9}$$

The aim is to achieve an uncertainty of $\Delta r < 0.1$ m. This gives the number of iterations required :

$$1 < \frac{\ln(0.1/3.2{\cdot}10^{6})}{\ln(|\dot{r}|/c)} \leq 2 \tag{4.10}$$

Two iterations are then carried out. They would reduce the range uncertainty to $3.2{\cdot}10^{6} \times (c/\dot{r})^{-2} < 3{\cdot}10^{-5}$ m if it were not for the intrinsic inaccuracy of the interpolation methods. As trigonometric interpolation was found to be slow, the first interpolation was carried with a spline, which was found to be a much faster method. It would reduce the range uncertainty to $3.2{\cdot}10^{6} \times c^{-1}\dot{r} \approx 9$ m if it were not for the intrinsic limitations of the spline interpolation. It would therefore require another iteration. It actually reduces the range uncertainty to 25 m RMS. The second interpolation would reduce the range uncertainty to $25 \times c^{-1}\dot{r} < 7{\cdot}10^{-5}$ m RMS which is much smaller than the intrinsic limitations of the trigonometric interpolation. Using this approach the satellite position is actually determined to within 0.15 m.

4.3.3 Satellite velocity

Numerical differentiation is slow because it requires the computation of two additional interpolations and is also subject to rounding errors. As an alternative, the coefficients found in the interpolation of the positions are multiplied by the derivatives of the trigonometric functions used in the interpolation of the positions, from Equation (4.5) :

$$\overrightarrow{\dot{S}} \simeq \sum_{i=1}^{4} i\Omega\left(-\overrightarrow{A_i}\,\sin i\Omega t + \overrightarrow{B_i}\,\cos i\Omega t\right) \tag{4.11}$$

This method is much more accurate and much faster than numerical differentiation.

The precise velocity and position of the satellite are then used to calculate the relativistic clock bias of the satellite $\Delta_s^r t$, in Equation (2.24), and, with the position of the receiver, the Sagnac bias r_s , in Equation (2.27d).

4.4 Receiver position

Once the absolute pseudoranges P^* and the satellite positions $\overrightarrow{S}$ are known, the position of the receiver can be computed as explained in Section 2.1.3.

4.5 Data choice and processing

The positions must not only be calculated, they must also be compared. As this project progressed, it became clear that traditional methods of statistical processing were not appropriate for this analysis. The selection of a large amount of days is explained in Section 4.5.1. The use of, rather than Root Mean Square (RMS), average errors and percentile errors is explained in Section 4.5.2

4.5.1 Data set choice

The following method was designed to semi-automatically obtain a good spread of receivers. Only a few GPS receivers could process GLONASS observations during the last Solar maximum, so only GPS observations were taken into account in this study. Only receivers that gave L1 and L2 observables at the time of study and are within the latitude and longitude ranges of the grid are accepted. Out of these, preference is given to the ones with P1 and P2 observables. Out of these, preference is given to the ones with an average 'filtered dual' benchmark closest to the reported position in the header of the RINEX file. If a receiver is less than 2° (222 km) away from another receiver, one of them, the least preferred one if there is a difference in preference, is excluded. Out ot this set, a few receivers that have L1, L2, P1 and P2 observables with an average 'filtered dual' position close to the reported position in the header of the RINEX file (see Section 3.6.3) and at an interesting position on the map, generally the centre or a corner of the set, are chosen as test receivers. The others are kept for the tomographic inversion. So any test receivers is left in a relatively poorly covered area, at least 222 km away from the nearest receiver used to produce the map of ED for the correction of its position, as shown on Figure 4.1. For Europe (Figure 4.1b), they were 74 receivers for the inversion and 4 test receivers. For North-America (Figure 4.1a), they were 106 receivers for the inversion and 5 test receivers. Each receiver typically sees 8 satellites at any time, and each satellite is visible up to 6 hours.

The ionosphere, being Sun-driven, has daily, yearly and solar cycles. Occasionally, bursts of radiations and charged particles also erupt from the Sun, causing a geomagnetic storm, during which the ionosphere is disturbed, and this for a few days. Also, a positioning system is not only evaluated with its accuracy, but also with its integrity, i.e. the probability with which it achieves a position within a given level of accuracy.

To estimate this probability, it was decided to test the method over a maximum of days. This was only limited by the amount of relevant data available. For Europe, 380 days were chosen : all of the days of the solar maximum year of 2002 were, to which were added the days from 21 October to 4 November 2003 for the set to contain at least one extreme storm, that of 30 October, and its aftermath. For North America, a lack of data from receivers giving P1 and P2 observables before October 2003 meant only 92 days were chosen, from 1 October to 31 December 2003.

For these number of stations, it takes MIDAS around 4 hours to carry out the tomography of one day and produce the full-height maps. The processing was parallelised to take advantage of the processing power available: two machines that had two four-core processors each ran 6 processes in parrallel each. This reduced the processing time from more than two months to less than one week.

4.5.2 Statistical processing method

An example of sample absolute errors is shown on Figure 4.4. This shows that the absolute errors show an amount of noise that can be large as shown by the unfiltered dual-frequency positioning errors on Figure 4.4b. To make the results readable with several methods on the same figure for easier comparison, some periodic statistics, e.g. hourly RMS or average absolute, has to be carried out. Losses of lock on the pseudorange can result in very high errors, e.g. around 9 UT on both days. Large outliers are given an inappropriately large amount of weight during RMS calculation. Average absolute errors was therefore preferred. However, average absolute errors do not represent the noisy nature of some quantities. It also does not give an idea of the integrity. Therefore percentile errors have been presented alongside average absolute errors.

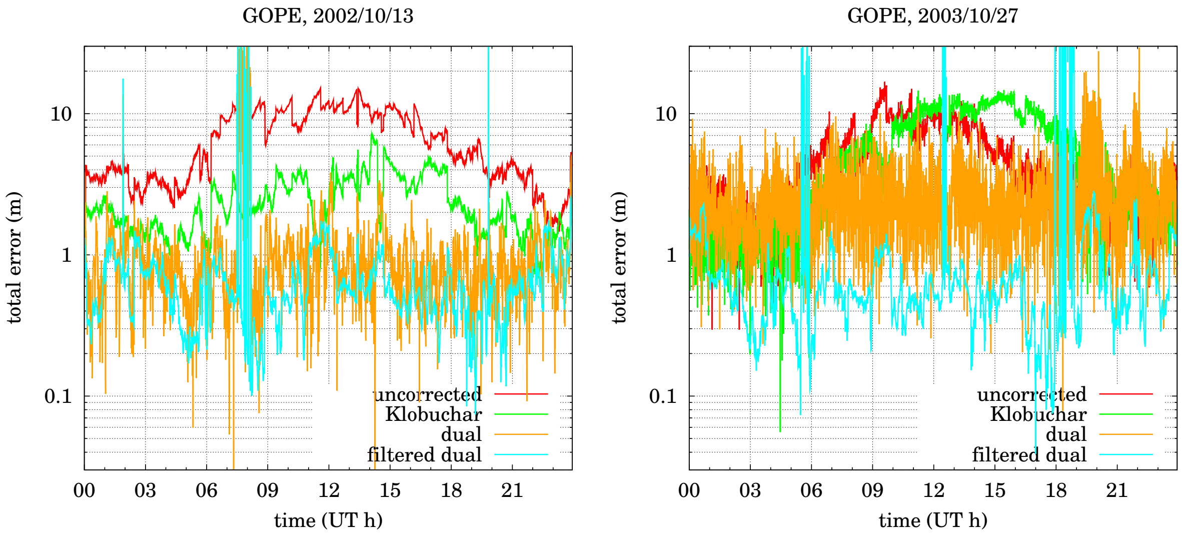

(a) (b)

Figure 4.4: Absolute errors for GOPE on 13 Oct 2002 (a) and on 27 Oct 2003 (b). See also Figure 3.2.

4.6 Conclusion

In this Chapter the methods to obtain the positions of the satellites and the absolute pseudorange have been explained, as well as the data processing choices behind the analysis. It has been shown that the phase-filtered dual-frequency pseudorange has a typically 1.5 m residual. These methods are the same to get and analyse all the positionings throughout Chapter 6 and Chapter 7 to compare all the ionospheric correction methods detailed in Chapter 3. In particular, a forecast and broadcast map are among the compared ionospheric corrections. The method to compress the forecast and to broadcast it is detailed in Chapter 5.

Chapter 5

Transmission

It has been shown in Chapter 2 that the positioning accuracy can be improved by compensating for the main factors. This research focuses on the temporally and geographically variable errors caused by ionospheric effects, explained in Chapter 3. In Chapter 4 the positioning method, including the different ionospheric corrections compared in this project, have been detailed. In particular, Section 3.5.4 shows a forecast is possible and necessary. To make the forecast usable, it must be broadcast to the user and therefore compressed. Section 4.2.2 gives the broadcast map as one of the evaluated ionospheric corrections methods. The detailed explanation of the compression algorithm has been deferred until this Chapter.

The tight transmission constraints, given in Section 5.1, justified several stages of sometimes lossy compression, as explained in Section 5.2, and an efficient encoding, detailed in Section 5.3.

5.1 Constraints

An opportunity arose of transmitting the maps with the MSF Radio Time Signal (`http://www.npl.co.uk/time/msf/`) of the National Physics Laboratory (NPL). Bits 01A to 16A and bits 17B to 51B (NPL Time & Frequency Services, 2007) are to be used for the transmission.

The map of ED is then broadcast over a very low bandwidth of $51\,\mathrm{bits\,min^{-1}}$. The map is a three dimensional $n_{radii} \times n_{latitudes} \times n_{longitudes}$ array. For the map over Europe, the settings are $n_{radii} = 29$, $n_{latitudes} = n_{longitudes} = 23$, giving a total number of elements of $n_{voxels} = 29 \times 23 \times 23 = 15341$. Assuming eight bits of precision per number are enough, transmitting one map would require $15341/51 \simeq 2406\,\mathrm{min} \simeq 40\,\mathrm{h}$. This would mean that by the time the user would have finished downloading the map, it would be completely out of date. In order for the user not to wait too long to get the first map after the receiver is switched on, a target of $15\,\mathrm{min}$ is chosen for the duration of the transmission. This means the maps need to be compressed several hundred times down to $765\,\mathrm{bits}$.

5.2 Compression

As the MIDAS inversions use vertical basis functions (see Section 4.1), the vertical profiles of $n_{radii} = 29$ voxels can be represented as a weighted sum of the small number η of EOFs. The weights are used in a first stage of almost ten times lossless compression.

Gonzalez and Woods (2002, p.478) show Discrete Cosine Transform (DCT) is best for smooth varying images. The following stages are an adaptation of, DCT based, Joint Photographic Experts Group (JPEG) compression (Gonzalez and Woods, 2002, p.498). In the second stage of compression, two dimensional DCT is applied to these arrays. The resulting arrays are then cropped 3×3 times and stacked again to form one three dimensional $\eta \times 10 \times 30$ array, resulting in a 9 times lossy compression.

This smaller array is then normalised so that the first value of the array is 127. The other normalised numbers are rounded, with the numbers below 3 changed to 0. The resulting array is then composed of integers, with most of the few non-zero values towards lower indices. A zig-zag algorithm illustrated in Figure 5.1 is applied in order to convert this three dimensional array into a one dimensional array while keeping the non-zero values mainly towards the lower indices.

η_1

1	3	7	14	24	37	53	72
2	6	13	23	36	52	71	
5	12	22	35	51	70		
11	21	34	50	69			
20	33	49	68				
32	48	67					
47	66						
65							

η_2

4	9	17	28	42	59	79
8	16	27	41	58	78	
15	26	40	57	77		
25	39	56	76			
38	55	75				
54	74					
73						

η_3

10	19	31	46	64	85
18	30	45	63	84	
29	44	62	83		
43	61	82			
60	81				
80					

Figure 5.1: Zig-zag algorithm.
This figure shows, for each element of the DCT of each EOF coefficient, the order number at which it is going to be encoded. The first number to be encoded is on the first row and the first column of the DCT of the first EOF. The number of the first row and the first column of the DCT of the third EOF is encoded tenth.

5.3 Encoding

Using Huffman coding, like for the last stage of JPEG compression, would require to transmit a dictionary prior to transmit the numbers. As the bandwidth is so limited, it has been preferred to encoded the numbers in an efficient way instead.

First, the normalisation factor $\overline{N}$ is encoded. This is a positive number representing the overall intensity of the ionosphere. It can vary greatly and needs to be know precisely, as its precision impacts the precision of the map overall. A sixteen bits precision, including 8 bit decimal places, of its binary logarithm is chosen for its representation. This means the following number: $2^8 \times \log_2 \overline{N}$ is rounded and transmitted as a 16 bits positive integer.

Then, the threshold is encoded. This is a small positive number. Numbers are encoded so that numbers close to zero take a minimum of bits. For positive numbers, the number of bits necessary to represent them is encoded as a three bit positive integer. Then the integer is represented, omitting the most significant bit, as it will always be 1. This is shown in Table 5.1.

number	encoding
0	000
1	001
2	0100
3	0101
4	01100
5	01101
6	01110
7	01111
8	100000
9	100001
10	100010
11	100011
12	100100
13	100101
14	100110
15	100111
16	1010000
17	1010001
30	1011110
31	1011111
32	11000000
33	11000001
62	11011110
63	11011111
64	111000000
65	111000001
126	111111110
127	111111111

Table 5.1: Encoding of positive integers

Then, the numbers of the three dimensional array are encoded in the zig-zag sequence previously described in Section 5.2. The first element is omitted, because, due to the scaling, it will always be 127. As the array is mainly made of sequences of zeroes, sequences of zeroes are encoded as follows: first, three “0” bits, then the number of zeroes in the sequence, encoded as a positive integer (see Table 5.1). For integers than can be positive and negative, the number of bits necessary to represent them is encoded as a three bits positive integer. Then the sign of the integer is represented, with “0” and “1” respectively for negative and positive. Then the absolute value of the integer is represented, omitting the most significant bit, as it will always be 1. This is shown in Table 5.2. The last sequence of zeroes is represented with six “0” bits, in this way signifying the end of the transmission.

5.4 Conclusion

As the most significant numbers are encoded first (see Section 5.2), the end of the resulting bit sequence can be truncated with a minimum of information losses. This is shown on Figure 6.1. The impact on the positioning is in this way kept to a minimum, as is shown in Chapter 6.

number	encoding
-127	1110111111
-126	1110111110
-65	1110000001
-64	1110000000
-63	110011111
-62	110011110
-32	110000000
-31	10101111
-30	10101110
-17	10100001
-16	10100000
-15	1000111
-14	1000110
-9	1000001
-8	1000000
-7	011011
-6	011010
-5	011001
-4	011000
-3	01001
-2	01000
-1	0010

number	encoding
1	0011
2	01010
3	01011
4	011100
5	011101
6	011110
7	011111
8	1001000
9	1001001
14	1001110
15	1001111
16	10110000
17	10110001
30	10111110
31	10111111
32	110100000
62	110111110
63	110111111
64	1111000000
65	1111000001
126	1111111110
127	1111111111

Table 5.2: Encoding of signed integers

Chapter 6

Europe Results

It has been shown in Chapter 2 that, of all the factors that have an impact on GPS positioning, the precise correction of the ionospheric delay is the only one left to be improved. Several ionospheric correction methods, reviewed in Chapter 3, will be compared in this Chapter, based on the results section of Allain and Mitchell (2009b). The positioning method detailed in Chapter 4 will be followed. In particular, the impact on the positioning of the compression algorithm described in Chapter 5 will be evaluated.

A brief comparison of the ionospheric maps is done in Section 6.1. Most of the ionospheric corrections listed in Section 4.2.2 will be compared here : ‘uncorrected’, ‘Klobuchar’, ‘IRI’, ‘forecast’, ‘broadcast’, ‘full-height’, ‘dual’ and ‘filtered dual’. Depending on the ionospheric corrections used, different positioning results have been obtained. They have been analysed in Section 6.2 as explained in Section 4.5. The results for a geomagnetically quiet day and for an extreme storm day are also presented respectively in Section 6.3 and in Section 6.4.

6.1 Broadcast

The IRI, forecast and broadcast images were computed only for Europe. Figure 6.1 shows an example of the different types of tomographic images over the European region that have been integrated through and contoured to show the spatial distribution of vertical TEC with the cross-section of the ED at grid longitude 0°. The example has been chosen arbitrarily and is for 12:00 UT on the 13th October 2002. All images show a gradient in the TEC which increases to the south as would be expected for this time and location. All cross-section show an electron density profile that reaches a maximum at around 300 km for all grid latitudes from -16° to 24°. The IRI image however shows the gradient as if it was very weak and had a more pronounced peak ED with a lower top-side concentration.

6.2 Statistics

Figure 6.2 shows the diurnal variation of the mean vertical (a) and horizontal (b) positioning errors for the receiver at site location GOPE and of their respective 90% percentile, (c) and (d). Each curve shows positioning error calculated on a point-by-

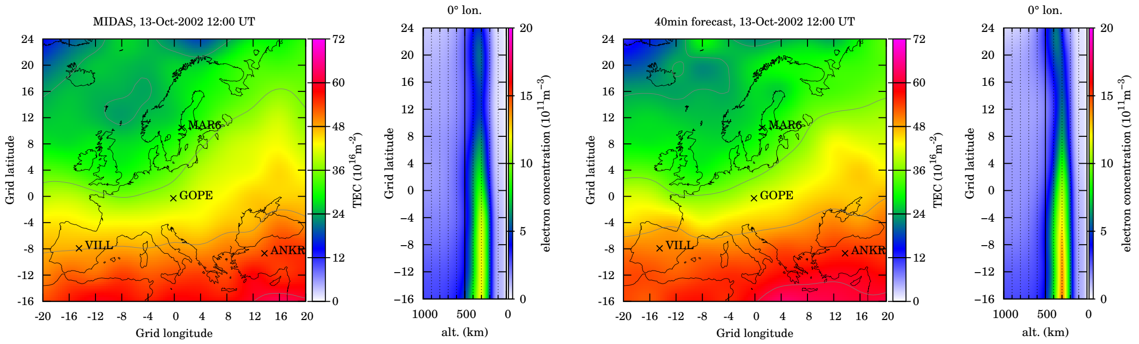

(a) MIDAS *(b) forecast*

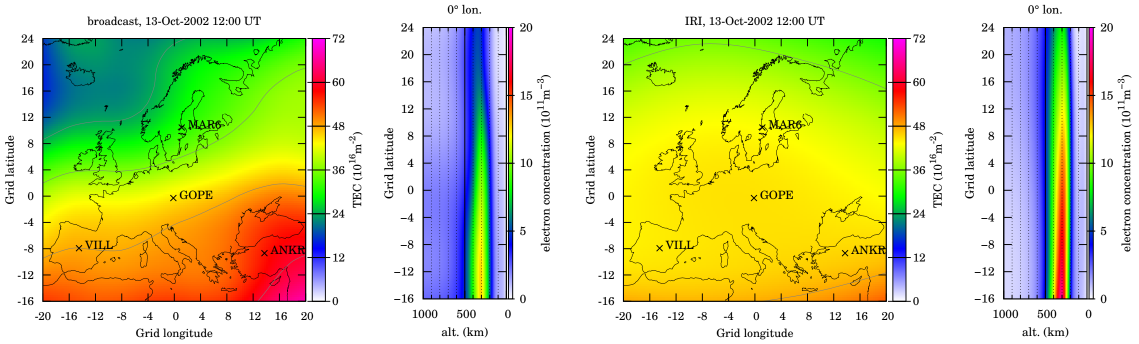

(c) broadcast *(d) IRI*

Figure 6.1: TEC from the vertical integration and cross-section of the ED on the 0° grid longitude plane of the MIDAS, forecast and broadcast images of 13 October 2002 12:00

point basis then averaged (mean) or sorted (percentile) over all of the points for that hour and for all the days of this study. The general accuracy is, in increasing order: uncorrected, Klobuchar, IRI, broadcast, 40 min forecast, near real-time and phase-filtered dual-frequency. The increase between the mean and the 90% percentile for the unfiltered dual-frequency positioning component is more important than for all the other corrections : when the error is similar and slightly lower respectively for the vertical and horizontal components on the mean, it is typically 1 m higher and similar respectively for the vertical and horizontal components on the 90% percentile. It can be seen by comparing (a) with (b) and (c) with (d) that the majority of the positioning error caused by the ionosphere impacts the vertical component rather than the horizontal one.

Figures 6.3 and 6.4 show the mean and 90% percentile positioning errors for the four test sites (see Figure 4.1b) for all the days of this study. All four sites show the same order of increasing accuracy, again for all corrections but for the unfiltered dual-frequency. It is less accurate than the broadcast maps but more accurate than IRI maps during the day, and slightly less accurate than even Klobuchar at night as the error remains constant throughout the day for MAR6 and VILL and similar to the near real-time and 40 min forecast for GOPE and ANKR. Comparing the uncorrected results in each of the four graphs (red curve) the largest errors occur at midday, with

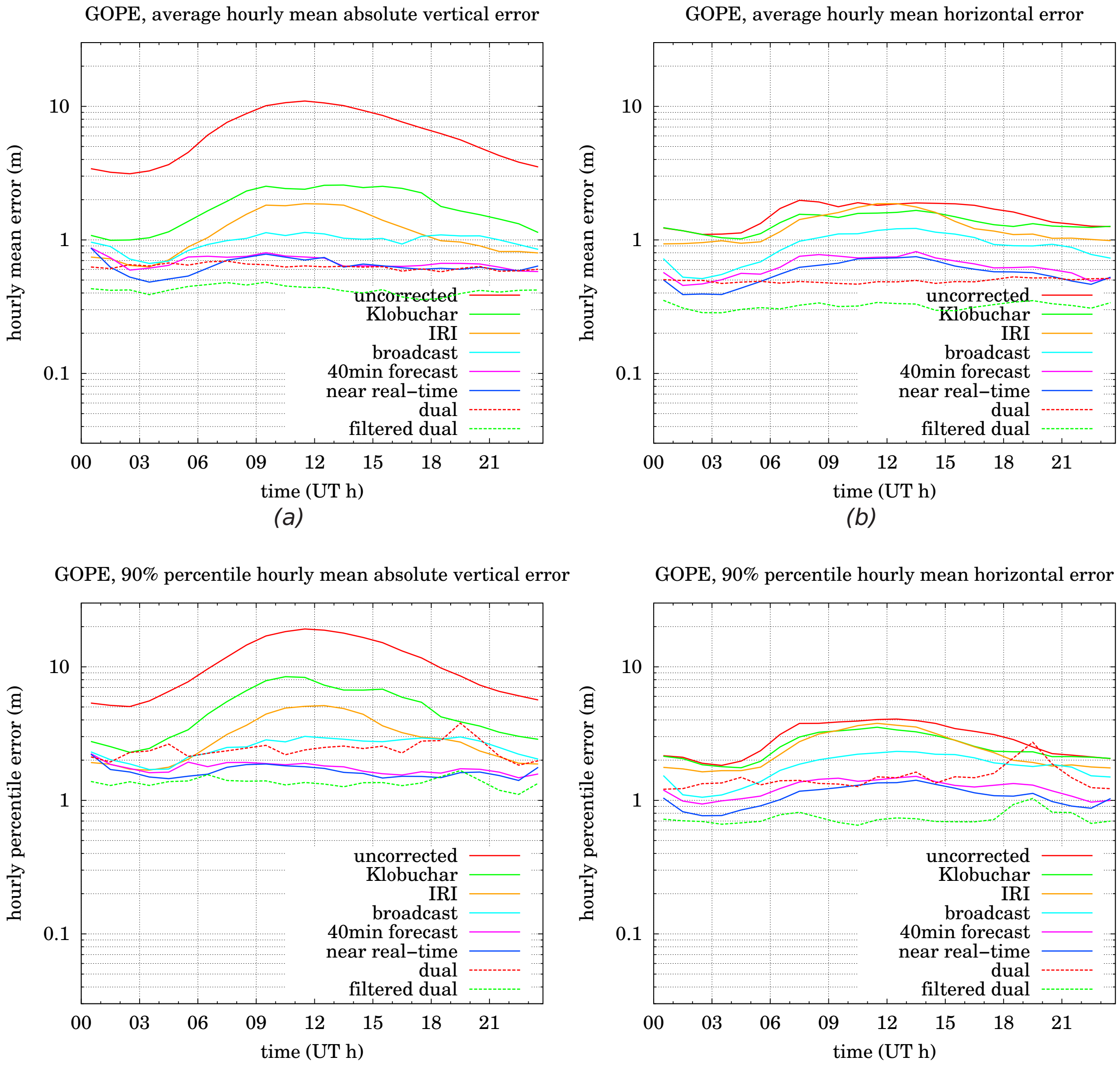

(a) (b) (c) (d)

Figure 6.2: Absolute error components for GOPE : mean vertical (a), mean horizontal (b), 90% percentile vertical (c) and 90% percentile horizontal (d)

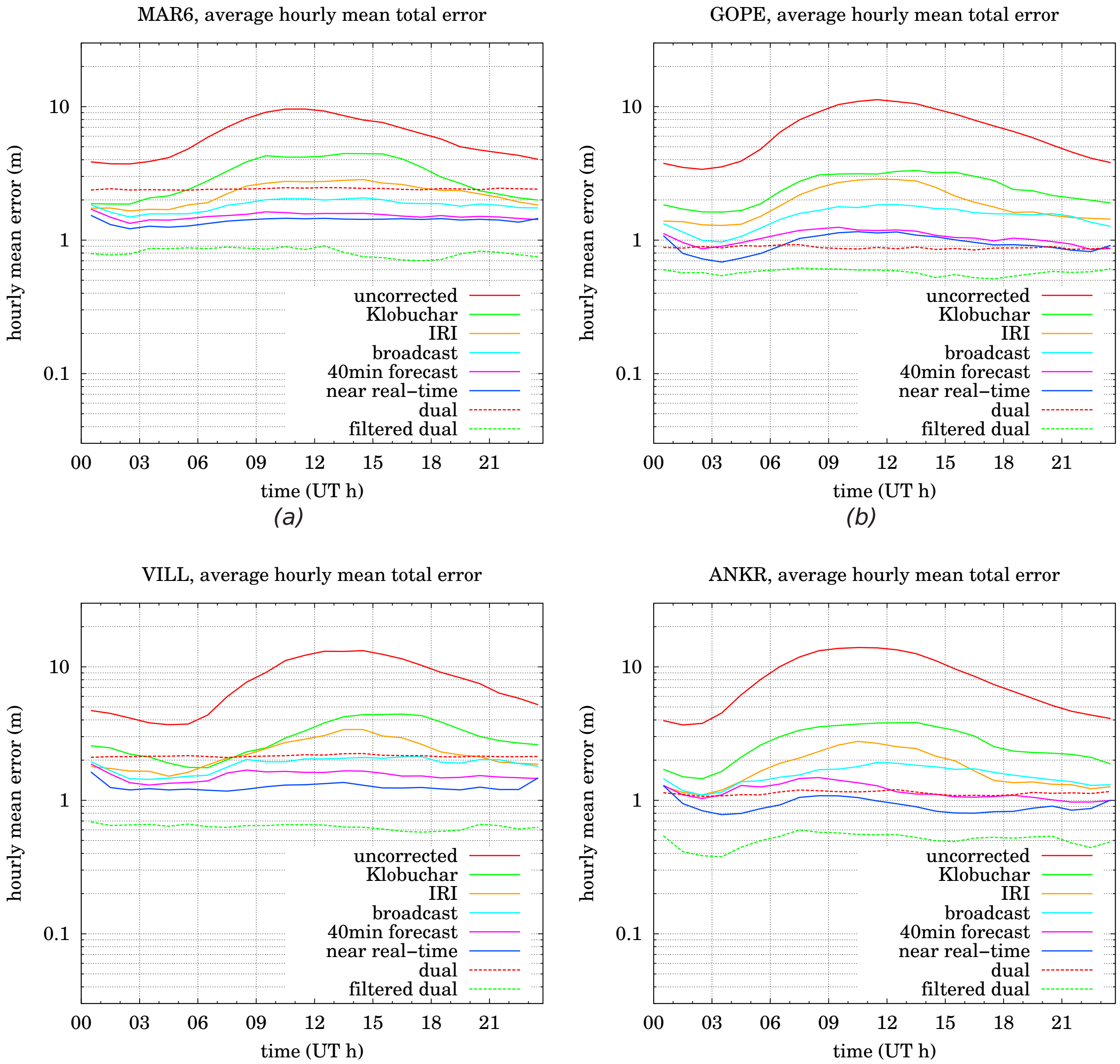

(a) (b)

(c) (d)

Figure 6.3: Average absolute positioning error for MAR6 (a), GOPE (b), VILL (c) and ANKR (d)

the most northerly site, MAR6, experiencing mean values of about 10 m (90% 18 m), the middle one, GOPE, mean values of about 11 m (90% 20 m) and the two southerly sites, VILL and ANKR, mean values of about 13 m (90% 20 m). The Klobuchar model reduces these errors to mean values of about 4; 3 and 4 m respectively (90% 10; 9 and 9 m). Interestingly the IRI model is able to bound all of the errors at mean values of about 3 m (90% 6 m). This implies that it is compensating for the ionospheric error for the southerly sites better (in percentage terms) than those to the north. The MIDAS and the 40 minute forecast MIDAS are able to bound the error at mean values of around 1.5 m (90% 3 m) and the phase-filtered dual-frequency receiver at mean values of about 0.5 m (90% 1.5 m) for these real-time positions. MIDAS is noticeably better for GOPE than for the other sites and this is likely to be due to the fact that GOPE is in the centre of the image region; thus is it likely that the MIDAS maps are most accurate where the surrounding distribution of receivers is good. The mean and 90% percentile positioning errors for GOPE are summarized in Table 6.1.

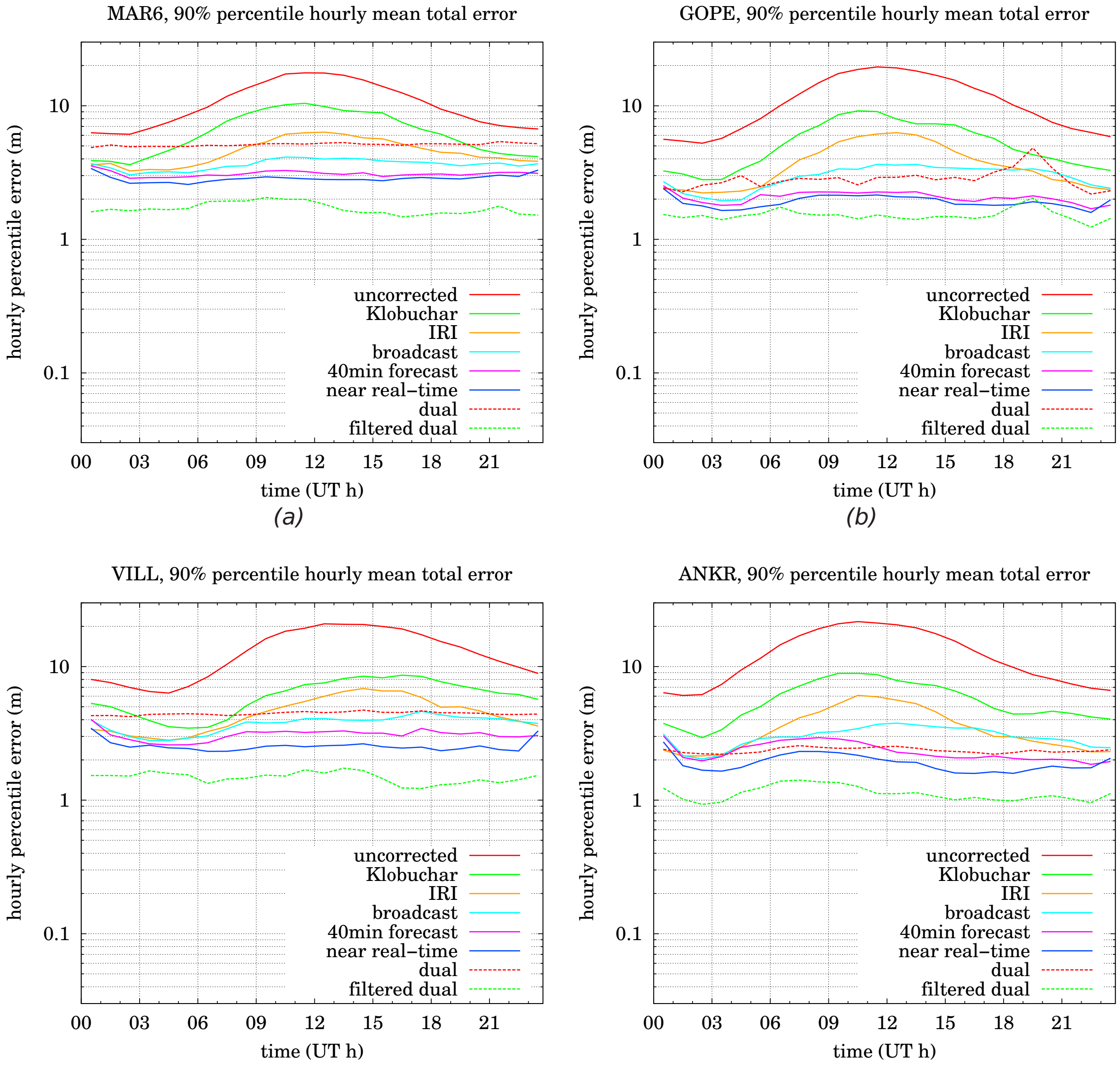

(a) (b) (c) (d)

Figure 6.4: 90% percentile absolute positioning error for MAR6 (a), GOPE (b), VILL (c) and ANKR (d)

method	mean	90% percentile
uncorrected	11	20
Klobuchar	3	9
IRI	3	6
MIDAS	1.5	3
phase-filtered dual-frequency	0.5	1.5

Table 6.1: Day-time positioning errors (m) for GOPE for all the days of the study

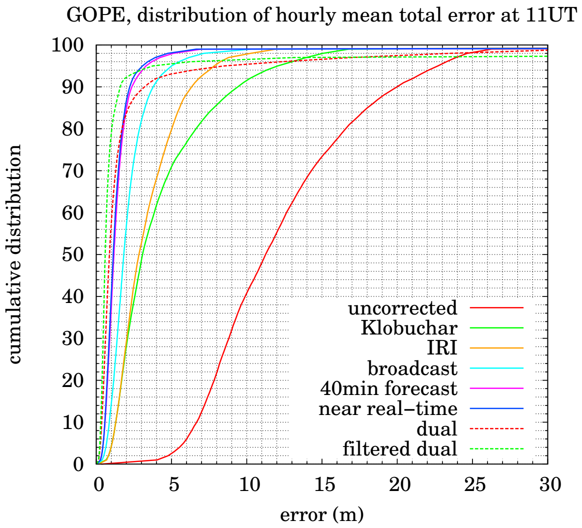

Figure 6.5: Cumulative distribution of total errors for GOPE at 11UT

Figure 6.5 shows the cumulative distribution of errors for GOPE at 11UT, the local midday. Each curve shows the portion of positions within a given uncertaincy for that hour and for all the days of this study. The uncorrected position is the only one to show an important systematic error : 95% of the positions it gives have an error superior to 6 m. The Klobuchar and IRI corrections perform equally for the first 30% of their positions, all within 2 m. Further up, the IRI gives a better performance. The forecast and near-real-time corrections show the best performance of all the single frequency distribution for all percentiles. When more observables have to be taken into account, the portion of cases when a coherent position is given is lower. A coherent position is given in 99% of the cases by the single-frequency methods. This is lower for the dual-frequency methods because they rely 2 and 4 observables, the lowest being the filtered dual, which relies on 4 observables and gives a position in 97% of the cases. At the 96th percentile and above, the MIDAS methods show the best performance. At this percentile and for this station, the errors on the positions are 3.5 m for the near real-time and the forecast methods, 5.5 m for the broadcast method, 6 m for the filtered dual, 8 m for the IRI, 12 m for the unfiltered dual, 13 m for the Klobuchar and 23 m for the uncorrected position.

6.3 Quiet day

Figure 6.6 shows the same as Figure 6.3 but for just one day of the study: 13 October 2002. This day was a geomagnetically quiet day with a Kp of 1.0 to 2.7. The hour-to-hour variability of the ionosphere is more apparent here from the uncorrected single frequency positioning errors. The general order of the accuracy is similar to the mean results of Figure 6.3. The Klobuchar model performs well on this day and, like IRI, is bounded at about 5 m. MIDAS is bounded at around 3 m.

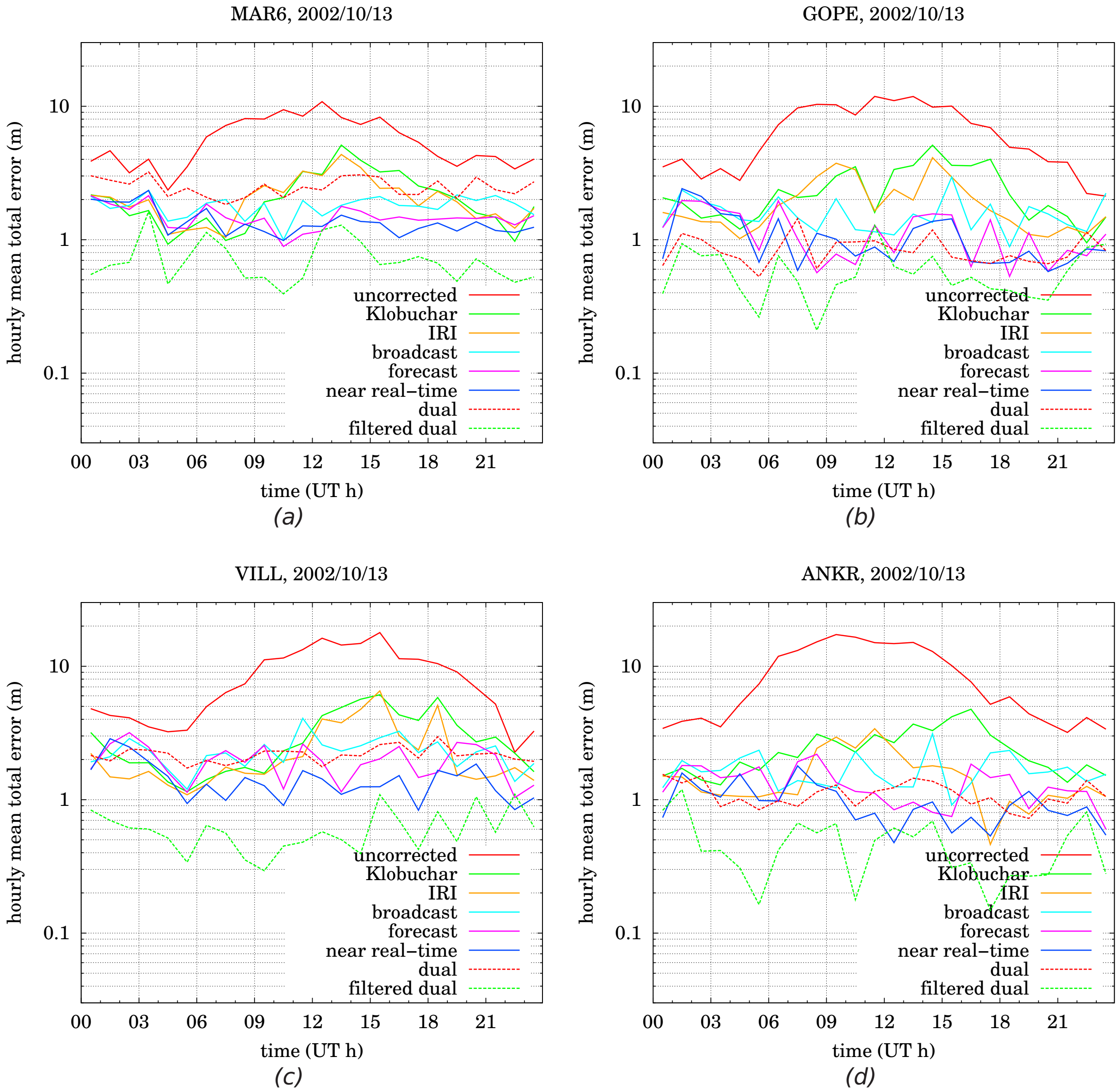

(a) (b) (c) (d)

Figure 6.6: Absolute error on the 13-Oct-2002 for MAR6 (a), GOPE (b), VILL (c) and ANKR (d)

6.4 October storm

Figure 6.7 shows the same as Figure 6.6 for another day of the study: 30 October 2003. This day was, over Europe, a negative geomagnetic storm day, which means the ionosphere was greatly depleted. The Kp index was between 4.7 and 9. The uncorrected positioning error is, during the day, about half of its mean value, showing the negative effect of the storm. The Klobuchar model performs very badly on this day, four times worse than its mean value, reaching above 16 m. Comparing the Klobuchar TEC with the MIDAS and the phase-filtered dual-frequency values shows the Klobuchar actually compensated about five times as much as it should have on this day. The general order of the accuracy for IRI, MIDAS and phase-filtered dual-frequency is similar to the mean results of Figure 6.3 but there are some points to note. IRI performs almost as well as MIDAS during the day for MAR6, the most northerly station. The signal has suffered from L2 losses of lock on this day and hence the positioning for the two more northerly sites, MAR6 and GOPE, is sometimes less accurate on the phase-filtered dual-frequency result. The unfiltered dual-frequency positionings were not affected, showing the losses of lock mainly affected the phase observations. MIDAS (Figure 6.8b) shows there were clusters of strong enhancement over Northern Europe in the evening explaining attenuation of the GPS signal, especially at the lower L2 frequency. In comparison, the IRI model (Figure 6.8a) shows an average ionosphere at that time.

Over Europe, the negative storm day of 30 October 2003 was preceded by two days of positive geomagnetic storm, with the Kp index between 3.0 and 4.7 on the 28th (initial phase) and between 4.0 and 9.0 on the 29th. MIDAS TEC maps and positioning results at VILL for these two days are shown on Figure 6.9. The uncorrected and phase-filtered dual-frequency results are similar to the mean results of Figure 6.3. The unfiltered dual-frequency results are particularly similar to the phase-filtered ones. A larger hour-to-hour variability of the ionosphere on the 29th is shown by the uncorrected single frequency positioning errors. Klobuchar, IRI and MIDAS positioning errors are generally twice as high as the mean results. Klobuchar, IRI and 40 min forecast show particularly strong changes (all increases but for Klobuchar on the 28th) in positioning error (Figure 6.9a) around 11:30 UT on the 28th, when the normally equatorial enhancement extended to most of Europe (Figure 6.9b), and around 19:30 UT on the 29th, when the normally polar depletion extended to most of Europe (Figure 6.9c).

6.5 Conclusions

In this Chapter, different methods of correcting for the ionospheric delay have been compared for 4 stations around the European region in 2002 and 2003. The first method uses no correction; the second and third use respectively the Klobuchar (1987) and IRI models; the fourth and fifth use respectively predicted and near real-time images from a four-dimensional inversion algorithm described by Mitchell and Spencer (2003), called MIDAS; the benchmarks use phase-filtered and unfiltered dual-frequency corrections. The results have been presented as hourly mean and hourly 90% percentile of the absolute error. It was shown that, while the Klobuchar and IRI models compensate for most of the ionospheric delay, the MIDAS images

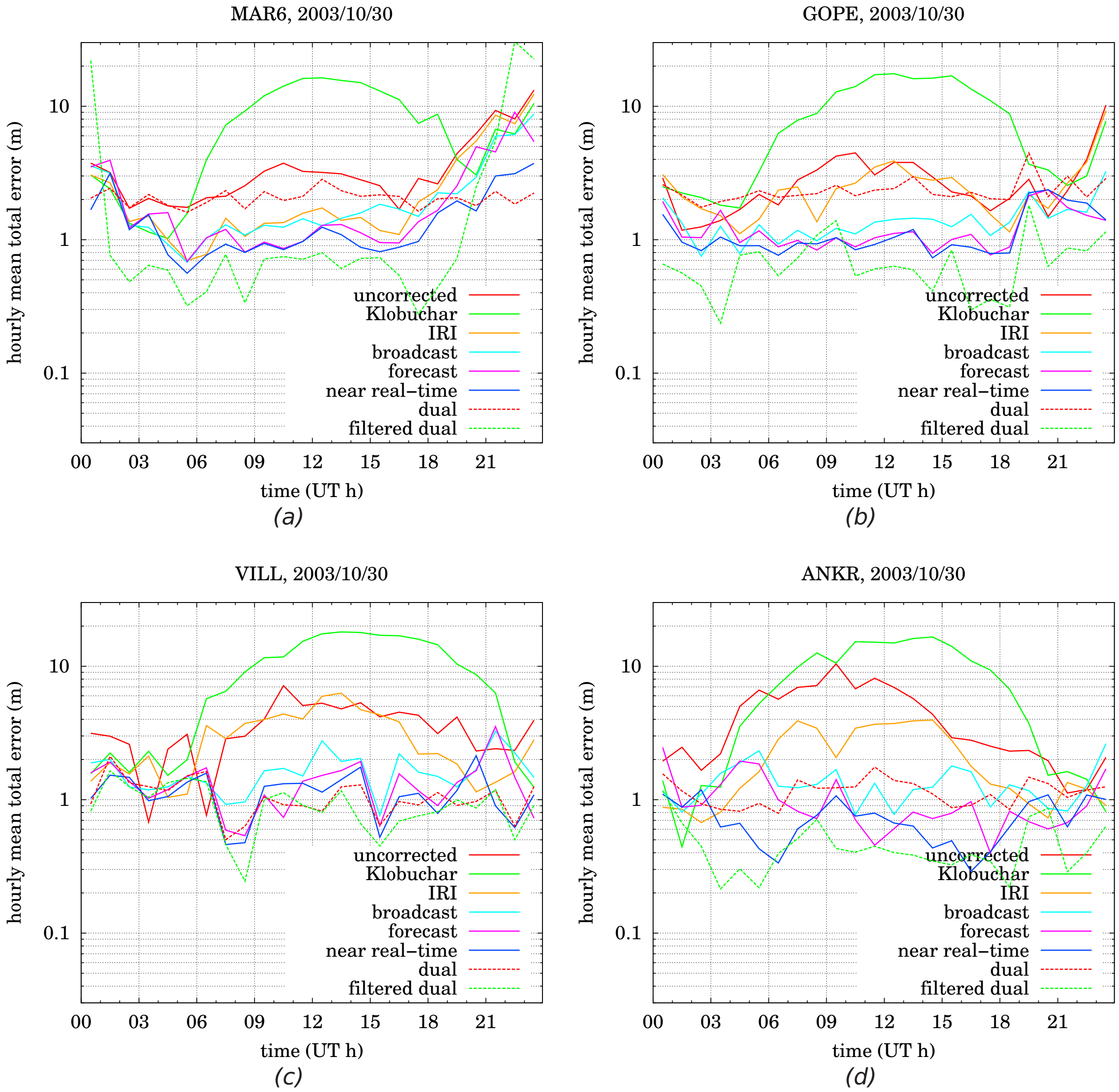

(a) (b) (c) (d)

Figure 6.7: Absolute error on the 30-Oct-2003 for MAR6 (a), GOPE (b), VILL (c) and ANKR (d)

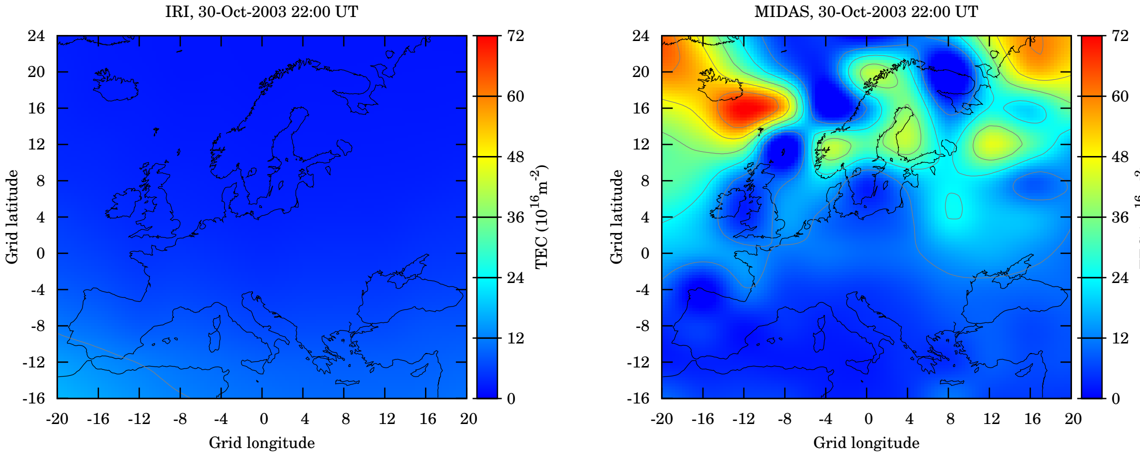

(a) (b)

Figure 6.8: TEC from the IRI (a) and MIDAS (b) images of 30-Oct-2002 22:00 UT

perform almost as well as the phase-filtered dual-frequency benchmark and for some stations better that the unfiltered dual-frequency corrections. The MIDAS methods show the best performance from the 96th percentile and above. Also, most of the positioning error comes from the vertical component.

Using MIDAS images gives a position on average within 1.5 m and 90% of the time within 3 m throughout the day, when the values during the day are 4 and 10 m for the Klobuchar model and 3 and 6 m for the IRI model. The horizontal positioning error is less than 2 m 90% of the time for the station at the centre of the map. MIDAS performs well even under extreme storm conditions and sometimes even better than phase-filtered dual-frequency as it is not vulnerable to losses of lock on the L2 frequency. The 40 min predicted MIDAS performs almost as well as the near real-time MIDAS, apart from rare and short periods when the ionosphere is particularly complex and dynamic. In a similar way, there are little differences between the forecast and its compressed-for-broadcast version, apart when the ionosphere is particularly complex.

The greatest errors appear to be for locations at the outset of the network used for the MIDAS inversion and are probably due to the lower accuracy of the MIDAS images in these areas.

The area of this study was generally under the mid-latitude region of the ionosphere.

This study has shown that, in general, the MIDAS method compensates the ionospheric delay better than the Klobuchar or IRI models. It compensates almost as well as phase-filtered dual-frequency, and sometimes gives an even better positioning as it is not vulnerable to losses of lock.

The study presented in this Chapter showed the impact of the forecast but did not evaluate thin-shell maps as they were not produced for Europe. A similar study

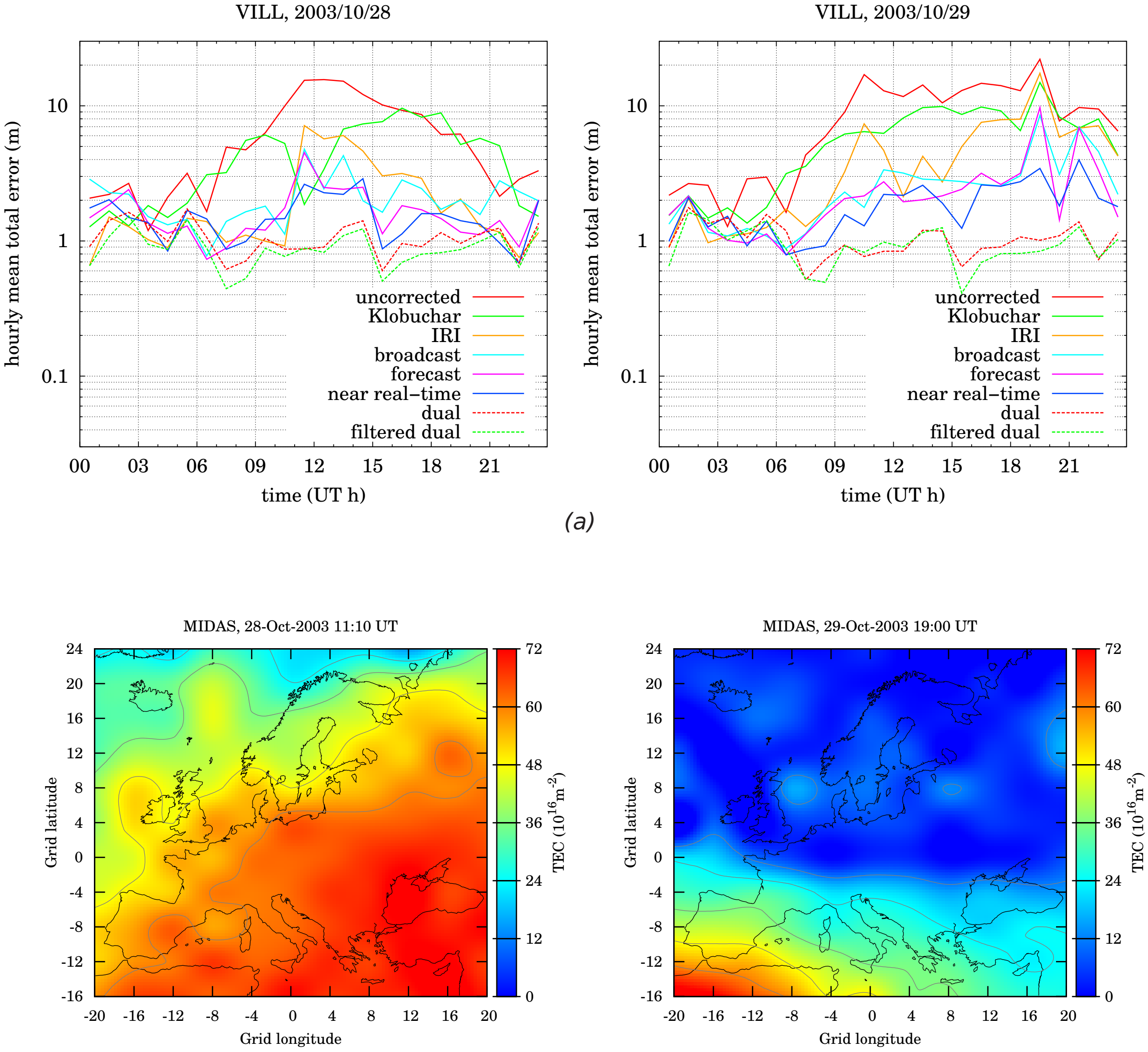

(a)

(b)

(c)

Figure 6.9: Absolute error on the 28 and 29-Oct-2003 for vill (a) and TEC from the MIDAS images of 28-Oct-2002 11:10 UT (b) and of 29-Oct-2002 19:00 UT (c)

that compares thin-shell and full-height maps has been done for North-America and is presented in Section 7.

Chapter 7

North-America Results

Among the several ionospheric correction methods reviewed in Chapter 3, all of the currently and widely broadcast ionospheric correction systems use thin-shell maps. This Chapter gives the results for positionings computed with MIDAS in thin-shell mode to evaluate the impact on the positioning of using thin-shell versus full-height imaging. As for the previous Chapter, the positionings with the following corrections, listed in Section 4.2.2, have also been computed and analysed: ‘uncorrected’, ‘Klobuchar’, ‘full-height’, ‘dual’ and ‘filtered dual’.

This Chapter is based on the results section of Allain and Mitchell (2009a). After a brief comparison of the thin-shell and full-height maps, the positioning results obtained with the different ionospheric corrections have been analysed in Section 7.1 as explained in Section 4.5. The results for several days around the extreme geomagnetic storm of 29-30 October 2003 and of the moderate storm day of 20 November were also presented respectively in Section 7.2 and in Section 7.3.

Figure 7.1 shows an example of a tomographic image over part of North America. The example has been chosen arbitrarily and is for 18:00 UT on the 27th October

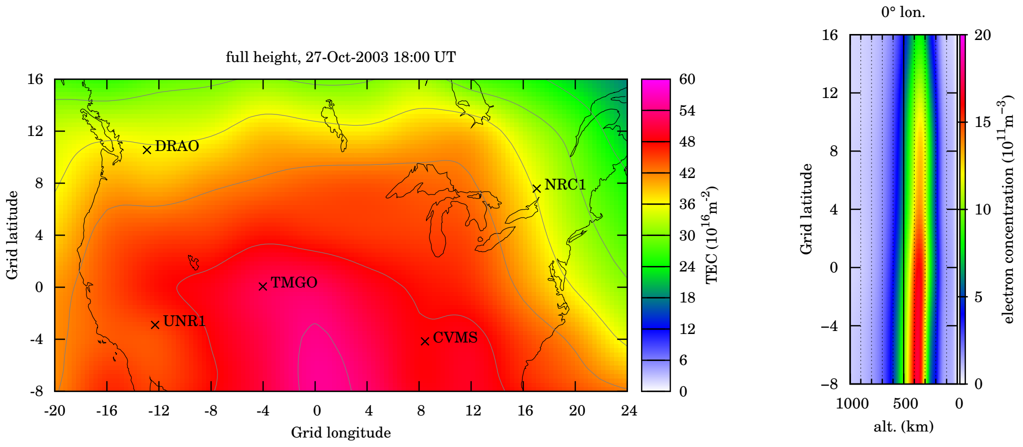

(a) *TEC from a vertical integration*

(b) *Cross-section of the free electron density on the 0° grid longitude plane*

Figure 7.1: Full-height image of 27 October 2003 18:00 UT

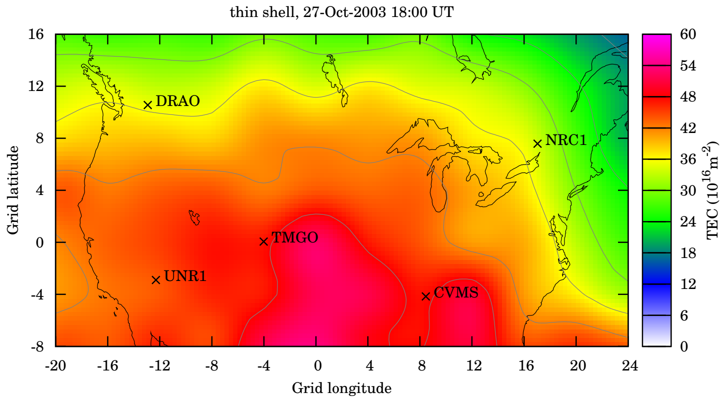

Figure 7.2: Thin-shell image of 27 October 2003 18:00 UT

2003. The 3D image has been integrated through and contoured to show the spatial distribution of vertical TEC on Fig. 7.1a. The TEC shows a gradient to the southern centre of the map as would be expected for this time and location. Figure 7.1b shows a cross section of the free electron density at grid longitude 0°. It shows the electron density profile reaches a maximum at around 350 km for all grid latitudes from -8° to 16°. Figure 7.2 shows the thin-shell image at the same time. The TEC values are similar to the TEC from the full-height image, slightly lower overall.

7.1 Statistics

Figures 7.3 and 7.4 show the mean and 95% percentile positioning errors for the five test sites (see Fig. 4.1) for all the days of this study. Comparing the uncorrected results in each of the five graphs (red curve) the largest errors occur at local midday, with all sites experiencing values of about 8 m (95% 13 m) but DRAO, in the north west, values of about 7 m (95% 12 m) and CVMS, in the south east, values of about 9 m (95% 16 m). The Klobuchar model reduces these errors to mean values of about 5; 4 and 6 m respectively (95% 13; 13 and 15 m), but on the local evening: the largest errors occur around 18:00 local time (around 00:00 UT). The thin-shell and full-height ionospheric maps reduce these errors to almost constant mean values of around 1 m for the northerly sites DRAO and NRC1, 1.5 m for TMGO, at the centre, and 2 m for the two southerly sites UNR1 and CVMS with a 95% percentile of around 5 m for all stations. Whereas the phase-filtered dual-frequency results is similar for all locations: mean around 0.5 m (95% 1.5 m), the unfiltered dual-frequency is most site dependent, going from mean around 1.5 m (95% 3 m) for the northerly sites to a mean of almost 6 m (95% 16 m) for CVMS. The unfiltered dual-frequency positioning for CVMS has the worst mean of all but the uncorrected positioning, then only during the day time, and has the worst 95% percentile of all positionings.

Figure 7.5 shows the cumulative distribution of errors for TMGO at 20UT, the local midday. Each curve shows the portion of positions within a given uncertaincy for that hour and for all the days of this study. The uncorrected position is the only one to show an important systematic error 95% of the positions it gives have an

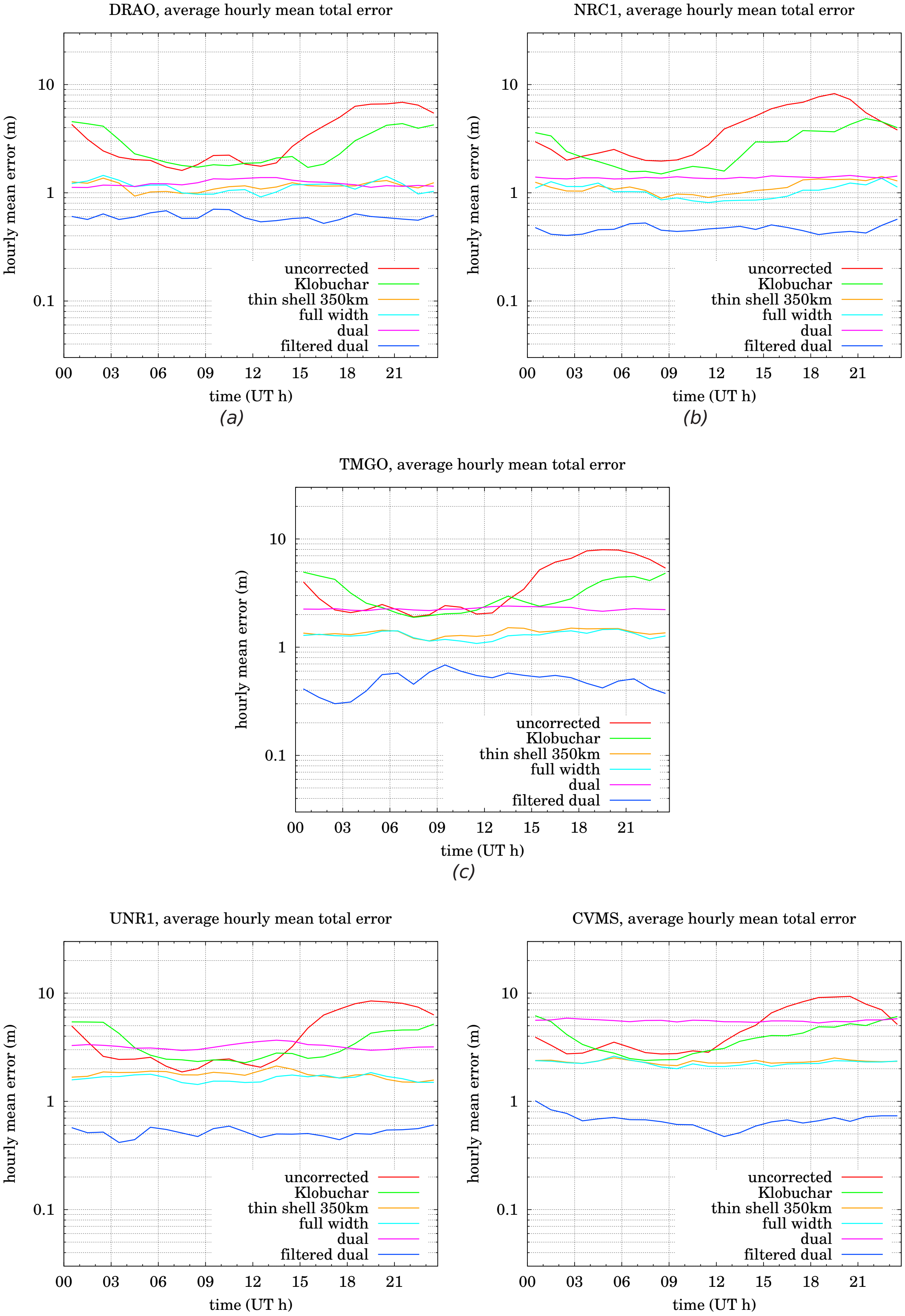

(a) *(b)*

(c)

(d) *(e)*

Figure 7.3: Average absolute positioning error

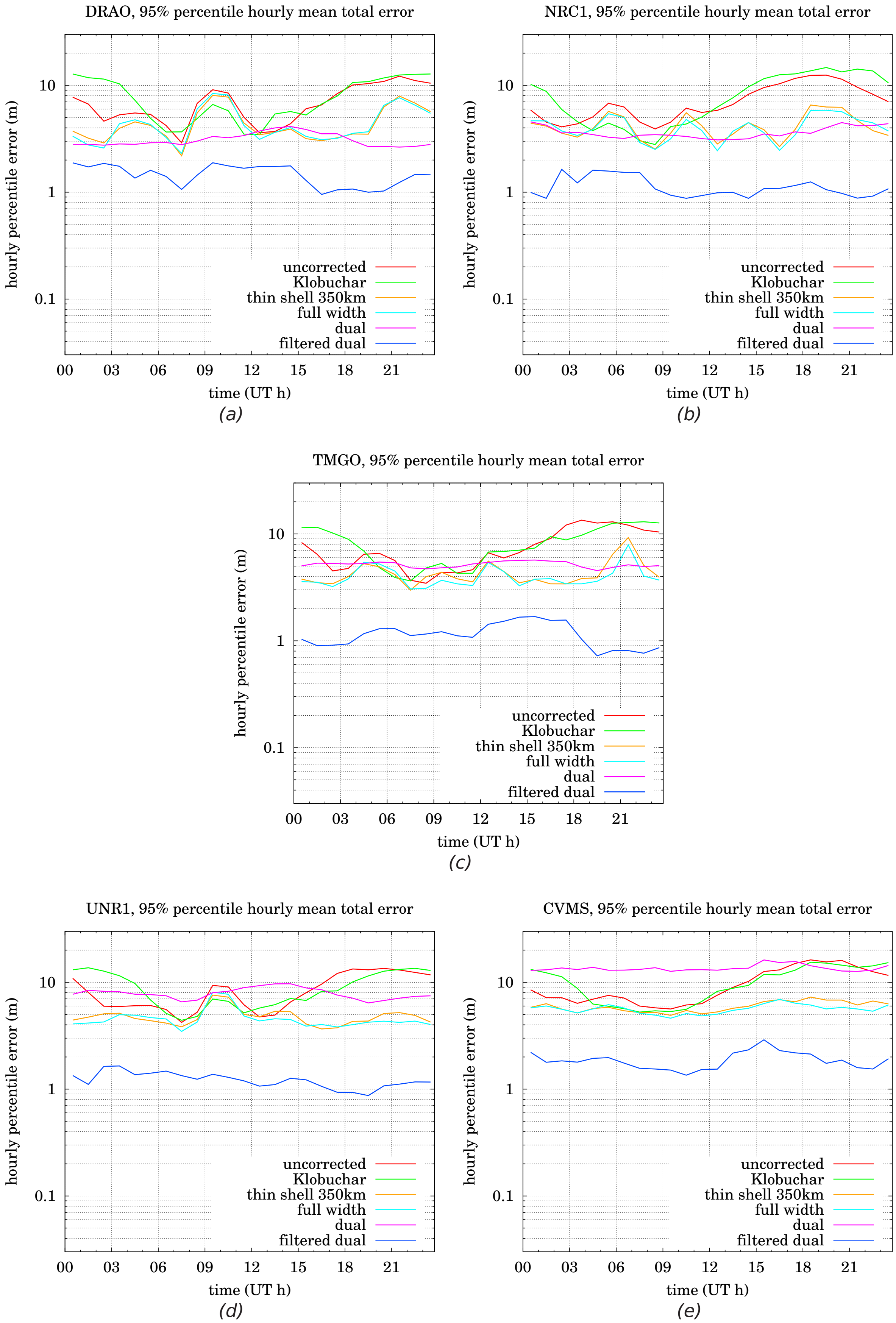

(a) (b) (c) (d) (e)

Figure 7.4: 95% percentile absolute positioning error

error superior to 4 m. The thin-shell and full-height corrections perform equally for the first 80% of their positions, all within 3 m. Further up, the full-height images give a better performance. The filtered dual-frequency correction shows the best performance for all percentiles. At the 95th percentile and for this station, the errors on the positions are less than 1 m for the filtered dual-frequency method, 5 m for the full-height and unfiltered dual-frequency methods, 9 m for the thin-shell and 13 m for both Klobuchar and uncorrected positions.

7.2 October storm

Figures 7.6 to 7.10 show the positioning errors for all 5 test sites from 27 October to 2 November 2003. The scale is different whether the values are below or above 10 m. Each curve shows positioning error calculated on a point-by-point basis then averaged (mean) over all of the points for the hour. At all times and for all stations, the dual-frequency positions are similar. All stations have a phase-filtered dual-frequency position and an unfiltered dual-frequency position similar to their seasonal averages, within 1 m for the phase-filtered dual-frequency and around 1, 1.5, 2.5, 3 and 6 m respectively for DRAO, NRC1, TMGO, UNR1 and CVMS. This shows that the dual-frequency positions were unaffected by this storm. The accuracy is similar on all days shown but the 29-30 October for all stations and for all single-frequency positions. The uncertainties on the thin-shell and full-height positions are both around 1.5 m for all stations but for CVMS at around 2 m, showing positioning performances close to phase-filtered dual-frequency for both. The uncertainty on the uncorrected position shows the diurnal cycle of the Sun-driven ionosphere with a local mid-day peak around 12 m. The uncertainty on the Klobuchar position is similar to the uncorrected position, showing the correction has, on these days, little effect on the quality of the positioning.

The 29-30 October was one of the strongest storms ever recorded. Figure 7.11 and Fig. 7.12 represent respectively the full-height and thin-shell images of the

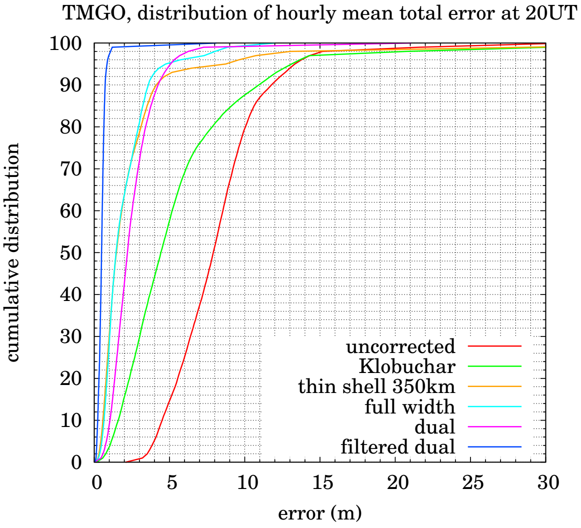

Figure 7.5: Cumulative distribution of total errors for TMGO at 20UT

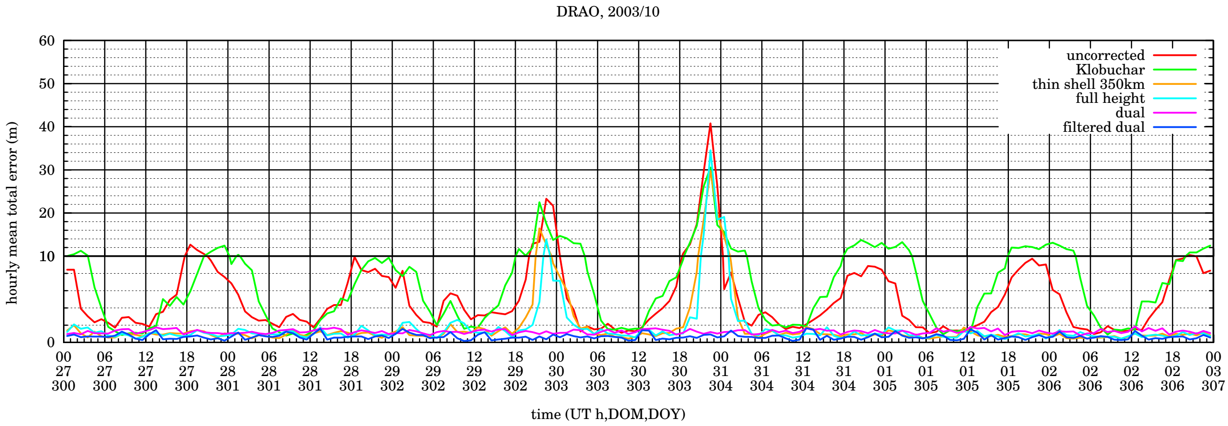

Figure 7.6:

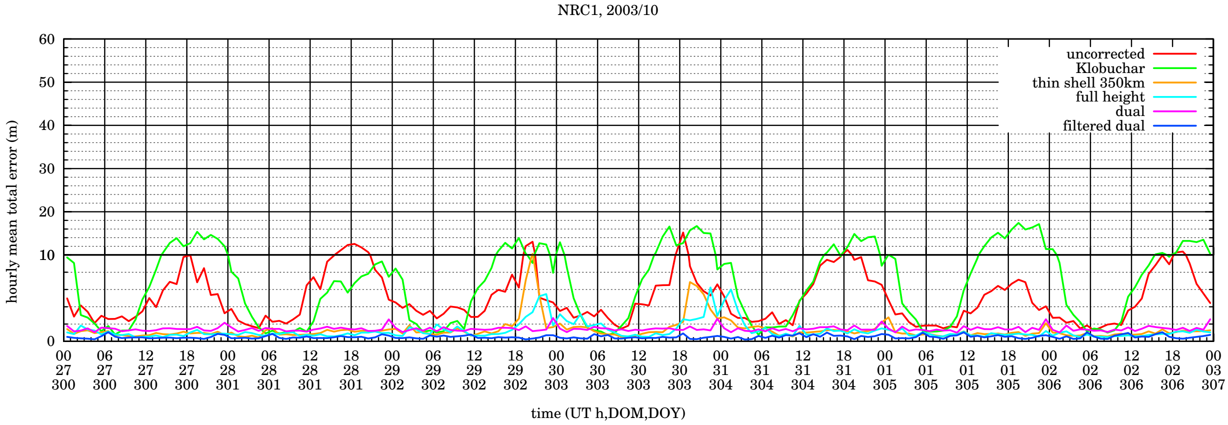

Figure 7.7:

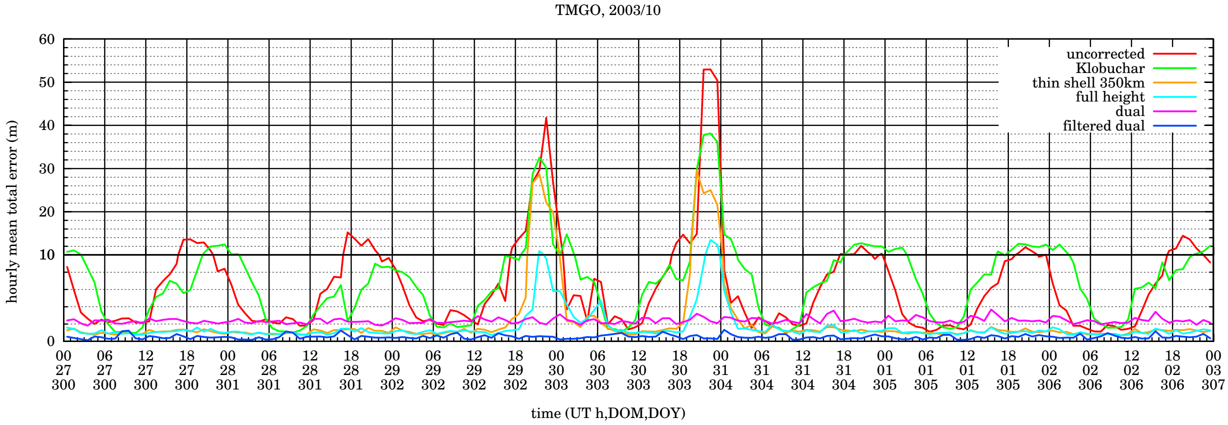

Figure 7.8:

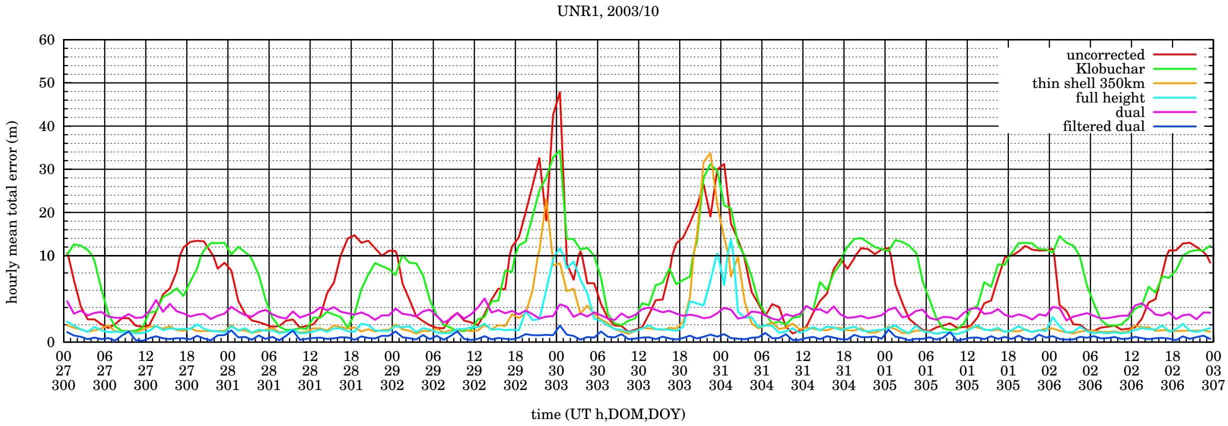

Figure 7.9:

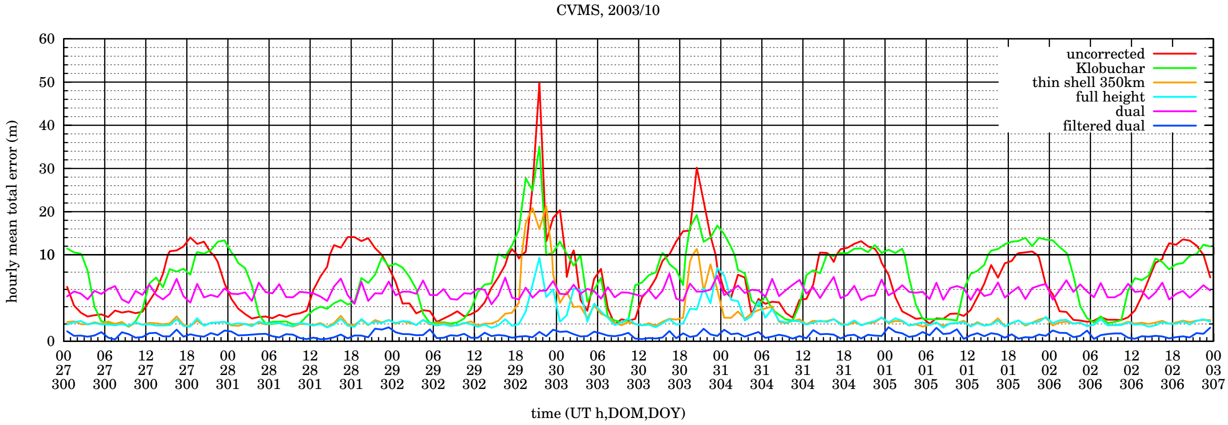

Figure 7.10:

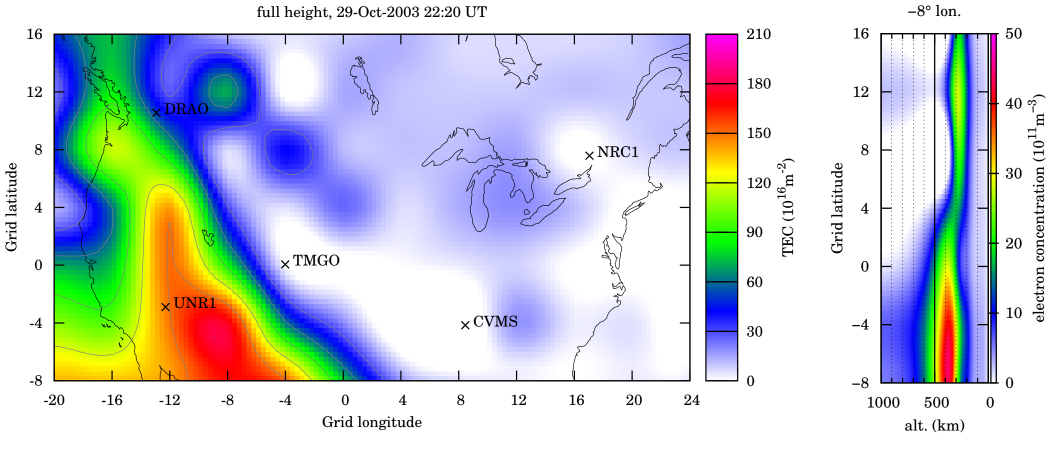

(a) TEC from a vertical integration

(b) Cross-section of the free electron density on the -8° grid longitude plane

Figure 7.11: Full-height image of 29 October 2003 22:20 UT

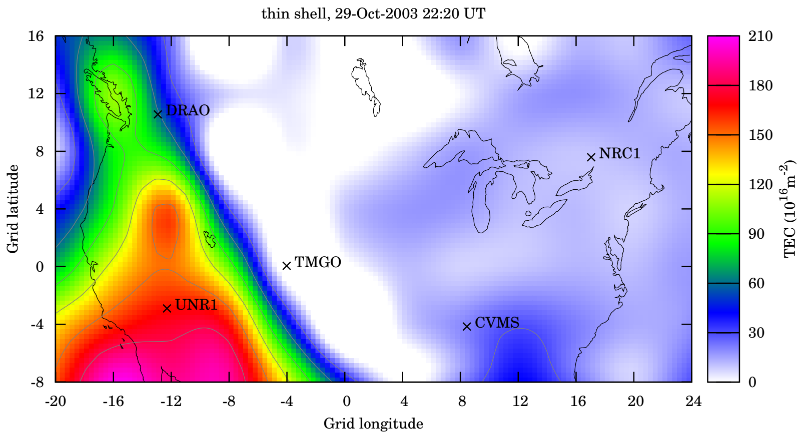

Figure 7.12: Thin-shell image of 29 October 2003 22:20 UT

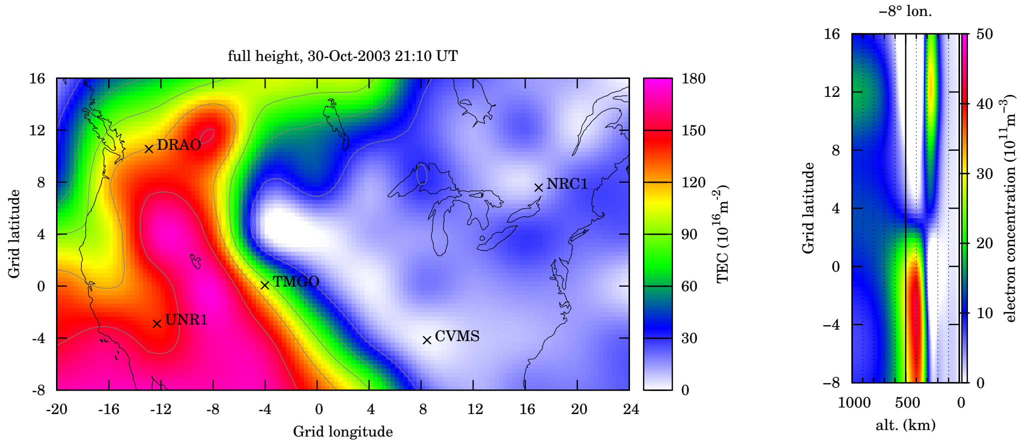

(a) TEC from a vertical integration

(b) Cross-section of the free electron density on the -8° grid longitude plane

Figure 7.13: Full-height image of 30 October 2003 21:10 UT

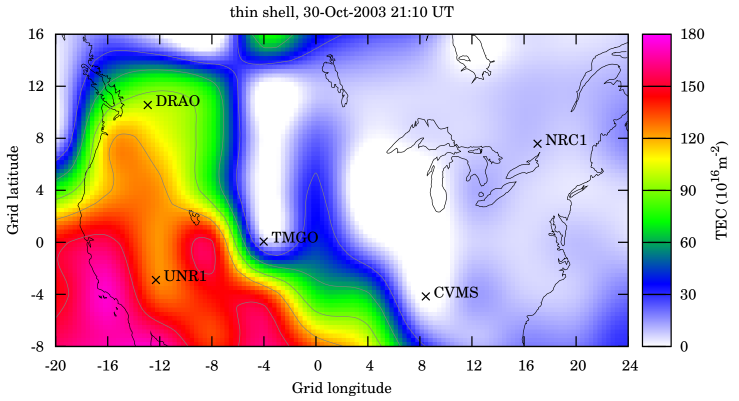

Figure 7.14: Thin-shell image of 30 October 2003 21:10 UT

station	uncorrected		Klobuchar		thin-shell		full-height	
DRAO	23	41	23	31	16	30	14	35
NRC1	13	15	14	17	10	7	5	6
TMGO	42	53	33	38	29	29	11	13
UNR1	48	31	34	31	23	34	12	14
CVMS	50	30	35	19	21	11	10	8

Table 7.1: Maximum positioning errors (m) for all stations on local 29-30 October

ionosphere at 22:20 UT on 29th October 2003 and Fig. 7.13 and Fig. 7.14 represent respectively the full-height and thin-shell images of the ionosphere at 21:10 UT on 30th October 2003. All four TEC maps show that the ionosphere was very disturbed on these days, showing strong variations over small distances, with a overall gradient to the south west reaching TEC values of almost 180 TEC units at these times. For both full-height images a cross section of the free electron density at grid longitude -8° is shown on Fig. 7.11b and Fig. 7.13b. Both cross sections show that the peak height was the same between -8° and 0° grid latitude and between 8° and 16° grid latitude, with strong changes around 4° grid latitude. On the 29th the peak height was just below 300 km around 12° grid latitude and just below 400 km around -4° grid latitude. This explains a difference in TEC of up to about 70 TEC units at -4° grid latitude -16° grid longitude between the full-height and the thin-shell images. On the 30th the change in peak height are even more important, about 250 km around 12° grid latitude and above 400 km around -4° grid latitude. There is also a very high electron density, about half the value of the maximum, in the top side of the ionosphere at 12° longitude, giving the electron density profile two strongly separated maxima. This explains differences between the full-height and the thin-shell images of around 60 TEC units in several locations, up to 70 TEC units at 12° grid latitude -8° grid longitude.

The very complex structure of the ionosphere on these days means it was difficult to correct for. Table 7.1 summarizes the maximum positioning errors for all stations on both days. NRC1, in the north east, is the station least affected by the disturbances as they occurred mainly in the south west : the uncertainties on the uncorrected and Klobuchar positions are only slightly higher than that of the surrounding days and the uncertainties on the thin-shell and full-height positions

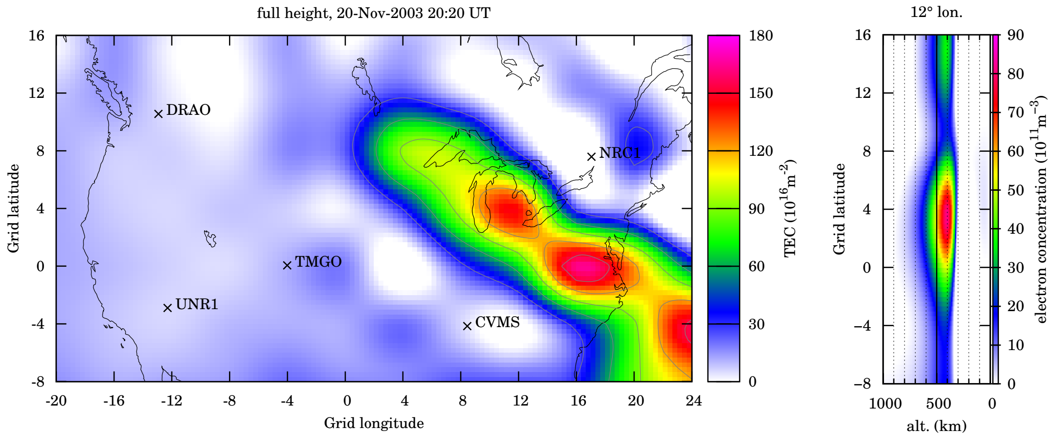

(a) TEC from a vertical integration

(b) Cross-section of the free electron density on the 12° grid longitude plane

Figure 7.15: Full-height image of 20 November 2003 20:20 UT

both reach up to around 10 and 6 m respectively. All other remaining stations are significantly more affected. For these stations and for both days all uncorrected positioning errors reach values between 30 and 53 m, but for DRAO on the 29th at 23 m. For these stations and for both days the Klobuchar positioning errors remain within values lower than the worse uncorrected positions, all between 30 and 45 m, but for DRAO on the 29th at 23 m and for CVMS on the 30th at 19 m. For these stations and for both days the thin-shell positions remain within 20 to 41 m but for CVMS on the 30th at 9 m. The thin-shell positions are an improvement over the Klobuchar position on most occasions but for TMGO on the 29th, 2 m worse, and for UNR1 on the 30th, 10 m worse. All full-height values remain within 15 m, showing an improvement over the thin-shell positions on most occasions but for DRAO on the 30th, 12 m worse, reaching 34 m. This can be explained by the fact that it was both below a region of the ionosphere particularly difficult to image and at the edge of the main group of receivers used for the inversion.

7.3 November storm

The 20 November was a moderate storm day. Figure 7.15 and Fig. 7.16 represent respectively the full-height and thin-shell images of the ionosphere at 20:20 UT on that day. Both TEC maps show that the ionosphere was relatively disturbed on that day, showing again strong variations over small distances, with a line of enhancement from grid latitude -4° grid longitude 24° to grid latitude 8° grid longitude 4° with TEC values reaching 180 TEC units. A cross section of the free electron density at grid latitude 12° is shown on Fig. 7.15b, showing that the peak height was more or less around 400 km for all grid latitudes shown. This explains a difference in TEC of up to about 40 TEC units at 4° grid latitude 12° grid longitude between the

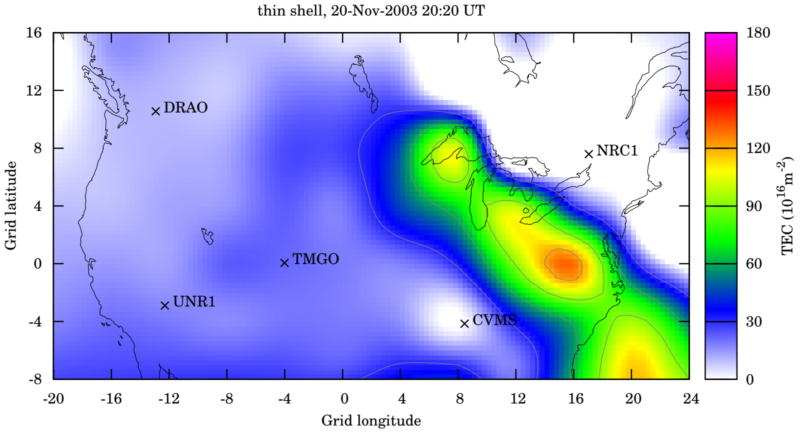

Figure 7.16: Thin-shell image of 20 November 2003 20:20 UT

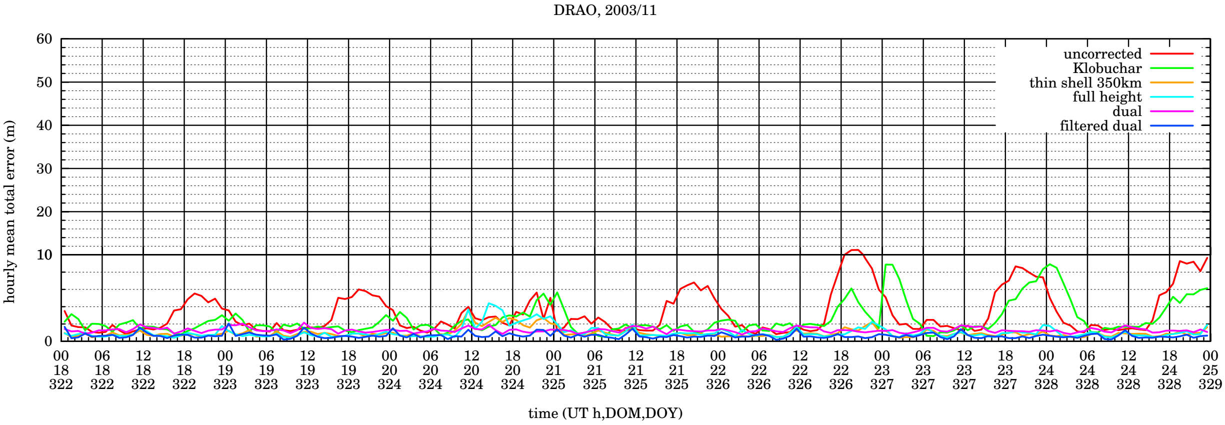

Figure 7.17:

full-height and the thin-shell images.

Figures 7.17 to 7.21 show the positioning errors for all 5 stations from 18 Novem-

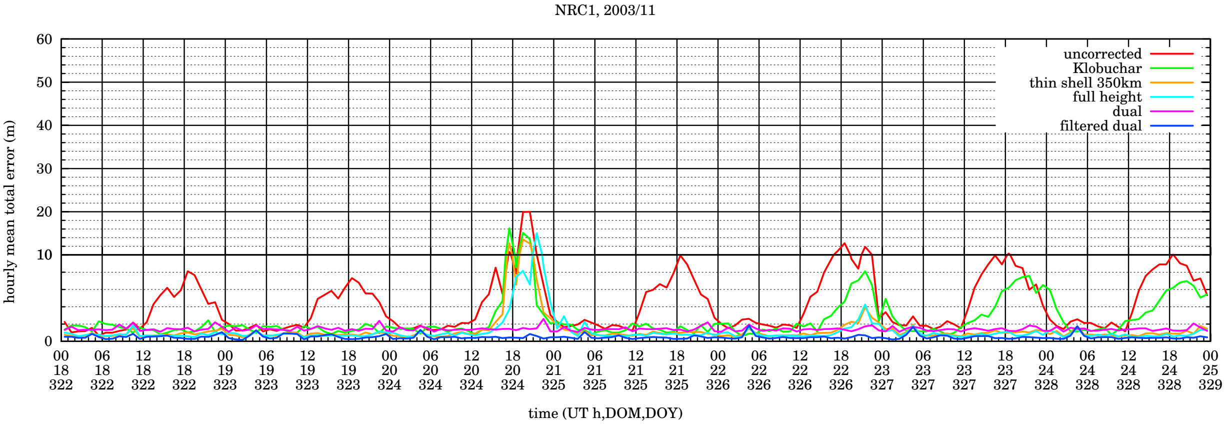

Figure 7.18:

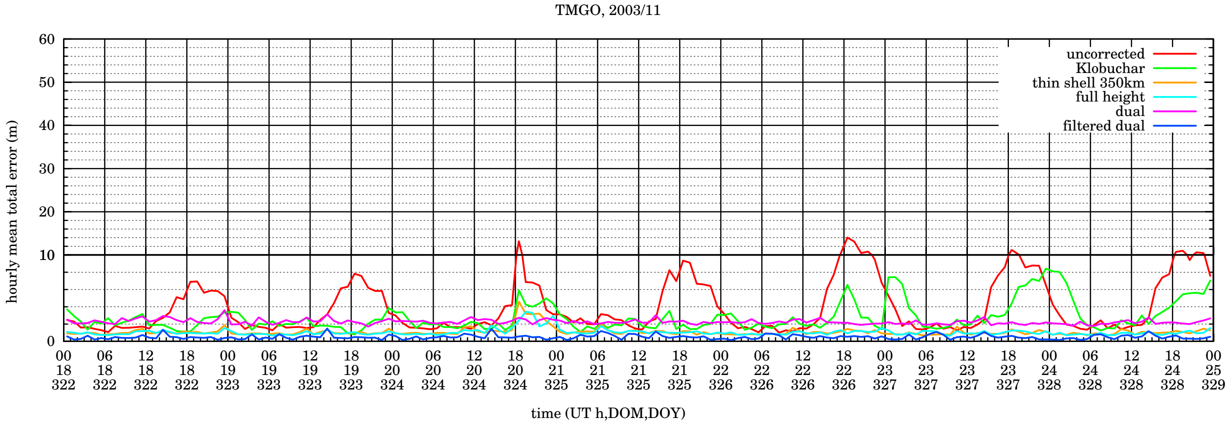

Figure 7.19:

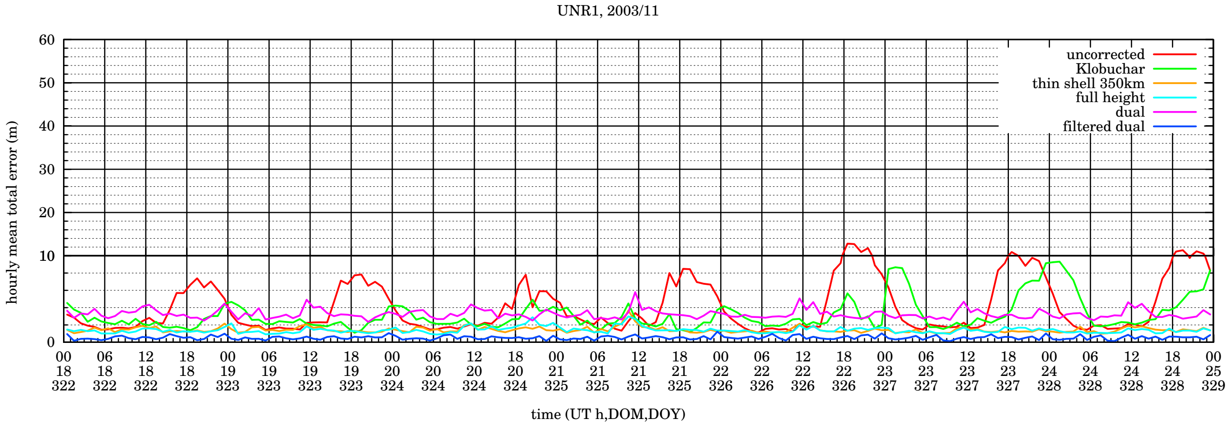

Figure 7.20:

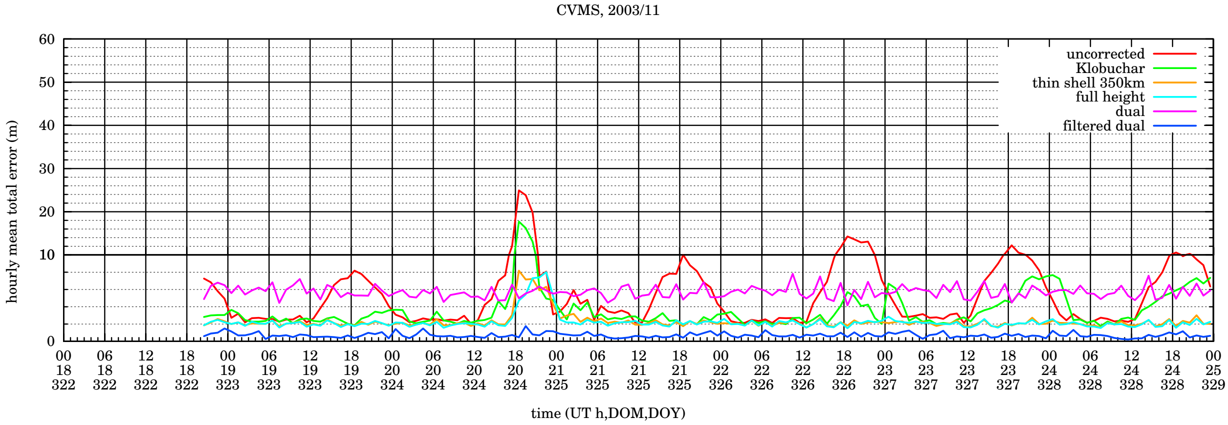

Figure 7.21:

ber to 24 November. No observations were available for CVMS on the 18th until 20:03:30 UT, which explains the blank before then on Fig. 7.21. All stations have a phase-filtered dual-frequency position and an unfiltered dual-frequency position similar to their seasonal averages. This shows that the dual-frequency positions were again unaffected by this storm. The uncorrected positioning errors give a good estimate of the ionisation : on the 18th and 19th, they reach up to around 6 m for DRAO and 7 m for the other stations; on the 20th ionisation enhancement are shown, negative for DRAO with almost no day-time peak, limited for UNR1, again reaching up to 7 m, and strong for NRC1, TMGO and CVMS, reaching up to 20, 13 and 25 m respectively; and slowly settling on the 21st and 22nd with maxima above average on the 23rd and 24th around 11 m for all stations but DRAO around 9 m. Of particular interest on the 18th, 19th and 21st were the good performances of the Klobuchar positions, all well within 5 m, even 2 m for NRC1. It however went back to normal on the following three days with maximum errors above average around 8 m. All stations have the full-height and thin-shell positions similar to their seasonal averages on all days but the 20 November. They perform similarly on that day, with maximum errors around 14 and 8 m for NRC1 and CVMS and around 3 m for all other stations.

7.4 Conclusion

In this Chapter, different methods of correcting for the ionospheric delay have been compared for 5 stations around North America from October to December 2003. The first method uses no correction; the second uses the (Klobuchar, 1987) model; the third and fourth use respectively thin-shell and full-height real-time images from a four-dimensional inversion algorithm called MIDAS ; the fifth method uses unfiltered dual-frequency corrections, the benchmarks uses phase-filtered dual-frequency corrections. The results have been presented as hourly mean and hourly 95% percentile of the absolute error. It was shown that, while the Klobuchar model compensates for most of the ionospheric delay, the thin-shell and full-height MIDAS images perform almost as well as the dual-frequency carrier-smoothed benchmark and for most receivers better than the unfiltered dual-frequency benchmark. Above the 80th percentile, the full-height images give a better correction than the thin-shell images.

Using MIDAS thin-shell and full-height images gives a position on average within 1.5 m and 95% of the time within 5 m, when the values are 0.5 and 1.5 m for the phase-filtered dual-frequency, 4 and 13 m for the Klobuchar model and up to 6 and 16 m for the unfiltered dual-frequency benchmark. The full-height corrections perform well and are considerably better than thin-shell corrections under extreme storm conditions : the positions of all but one receivers remained within 15 m during the 29-30 October 2003 storm. These results confirm those from Chapter 6, where Klobuchar model, full-height imaging and carrier-smoothed dual-frequency corrections were also compared for Europe. The main differences are that the storm enhancements were mainly positive and strong over North America rather than negative over Europe and that no significant losses of lock on the carrier-smoothed dual-frequency positioning were detected for this North America set of receivers. The unfiltered dual-frequency positioning error is particularly site dependent, with an average from 1.5 to 6 m and a 95% percentile from 3 to 16 m. This is unlike the phase-filtered dual-frequency benchmark, because the noise, which includes multipath, for the same satellite and the same receiver is very different on separate frequencies. This difference is greatly amplified by the dual-frequency calculation and makes the unfiltered dual-frequency pseudorange and positioning very noisy. A more thorough study on this point, i.e. the effect of multipath on dual-frequency pseudorange, would be valuable in the future.

The greatest error appears to be for a location at the edge of the network used for the MIDAS inversion while there was an important ionospheric structure above. This was probably due to the generally lower accuracy of the MIDAS images in these areas and to the intrinsic, numerical and computational difficulties of imaging certain features.

This study has shown the following : the full-height and thin-shell images both allow very good corrections of a quiet ionosphere; they even give a better positioning than unfiltered dual-frequency as they do not amplify the noise on the observations; the full-height images allow significantly better corrections of the ionospheric delay than the thin-shell images during extreme storms and at high percentiles.

Chapter 8

Conclusion

The main factors that affect GPS positioning have been detailed in Chapter 2. It was shown there that the uncertainty on the positioning depends on the PDOP and on the quality of the pseudorange measurement. The PDOP itself depends on the constellation, which is given and limited. All errors on the pseudorange measurement can be precisely compensated for, apart from the ionospheric delay.

The ionosphere has been described and several ionospheric correction methods have been reviewed in Chapter 3. Among them the currently and widely broadcast ionospheric correction systems, Klobuchar and SBASs, approximate the ionosphere to a thin shell, even though this approximation is not adequate neither at high latitudes nor at the equatorial regions nor on geomagnetic storm days. However the tomography of the ionosphere along all its height can be carried out. Several algorithms of ionospheric tomography were reviewed. One of them, MIDAS has been described as it is used in this project. A new method using a linear integration through maps produced with MIDAS in near real-time or in forecast mode has been proposed. The use of observations on two frequencies enables a precise measurement of the ionospheric delay. This is ideal but only possible with expensive receivers. As it has been used as a benchmark, it has also been presented. Its analysis has shown that the unfiltered dual-frequency measurement of the ionospheric delay has a typically 1 m peak-to-peak noise associated with it.

Based on the factors given in the previous chapters, methods to obtain the positions of the satellites and the absolute pseudorange have been designed. They have been explained and evaluated in Chapter 4. The evaluation of the interpolation of the positions of the satellites has shown it leaves an uncertainty only of around 0.04 m RMS. The evaluation of the phase-filtered dual-frequency pseudorange processing has shown it leaves a residual of around 1.5 m, induced by the noise of the unfiltered dual-frequency pseudorange. Because of the ways the ionospheric delay varies it has been decided to carry out the comparisons of the ionospheric corrections over long periods during the last Solar maximum. Because of the noise and the outliers on the dual-frequency positionings, it has been found that Root Mean Square (RMS) is not appropriate for this project. Averages and percentiles on the absolute errors have thus been chosen instead. These methods and choices have been the same to compare the positionings with the different ionospheric correction methods in the subsequent chapters.

Among the compared ionospheric corrections is one based on a compressed forecast MIDAS map. The method to produce it is given in Chapter 5. It has been designed to give a minimum of information losses, keeping in this way the impact on the positioning to a minimum.

Study	component	uncorrected		Klobuchar		MIDAS		filtered dual	
Europe	horizontal	2	5	2	4	0.7	1.5	0.4	0.7
	vertical	12	20	3	8	0.8	2	0.5	1.5
	total	12	20	4	9	1.2	2.5	0.6	1.5
North America	horizontal	1.5	4	1.5	4	1	3	0.4	0.7
	vertical	7	15	4	15	1	4	0.4	1.5
	total	8	15	5	15	1.5	4	0.5	1.5

Table 8.1: Typical errors (m, average and 90% or 95% percentile) with their components (see Appendix A)

The results of the evaluation has been presented in Chapter 6 and Chapter 7 and are summarised in Table 8.1. The proposed method compensates the ionospheric delay better than the Klobuchar or IRI models. It compensates almost as well as phase-filtered dual-frequency, and sometimes gives an even better positioning as it is not vulnerable to losses of lock. Both full-height and thin-shell images allow very good corrections of a quiet ionosphere, even giving a better positioning than unfiltered dual-frequency as they do not amplify the noise on the observations. However the full-height images allow significantly better corrections of the ionospheric delay than the thin-shell images during extreme storms and at high percentiles. The unfiltered dual-frequency positioning error is particularly noisy and site dependent, with an average from 1.5 to 6 m and a 95% percentile from 3 to 16 m. This is because the noise, which includes multipath, for the same satellite and the same receiver is very different on separate frequencies and because the dual-frequency calculation greatly amplifies the noise difference.

8.1 Implications and future work

These results raise very serious doubts about the use of dual-frequency for receivers operating in conditions when phase-filtering is not feasible and where multipath is high, e.g. for a vehicle moving through sky-obstructing features like buildings or trees. A more thorough study on the effect of multipath on dual-frequency pseudorange would be valuable. Indeed, almost all GNSSs are currently introducing multiple frequencies : for example GPS (Engel, 2008; IS-GPS-200D) and GALILEO (Hein and Pany, 2002). However, the effect of multipath on multiple-frequency pseudorange is not even mentionned in these studies. It is otherwise explicitly neglected by Benedicto et al. (2000). Also, more and more receivers are able to process signals from at least GPS and GLONASS, and almost all GNSSs are incresasing their constellation. Each GNSS has slightly different orbital characteristics for its satellites. Using more satellites gives a better PDOP, especially when the satellites have different kinds of orbits. However, because of the correlation between the ionospheric delay and the position of the satellite in the sky, a better coverage could only reduce the horizontal component of the positioning error from the ionospheric delay, and then only where and when there are no strong gradient in the ionosphere. This condition is met neither always nor everywhere as there are strong gradients even on geomagnetically quiet days, in particular with Sun rises and Sun sets and with the equatorial anomaly. So ionospheric correction will still be necessary in the future for all mass market receivers, those that can take into account signals from several GNSSs as well as dual-frequency receivers, which will need ionospheric correction to stabilise their very noisy dual-frequency positioning solution.

These results also confirm the suitability of thin-shell or full-height images on geomagnetically quiet days and at mid-latitudes. Other results (Rose et al., 2009) show the advantages of using MIDAS images in timing computation. The full-height images should be preferred when possible as they allow significantly better corrections of the ionospheric delay than the thin-shell images during extreme storms and at high percentiles. The transmission of the navigation correction requires a forecast and an image compression adapted to the available broadcast system. The feasibility of this is demonstrated for Europe. High rate compression looses some significant information when the ionosphere is particularly complex. Therefore a broadcast system with a wider bandwidth than the very narrow one currently available, allowing much less information losses, should be considered if more reliable corrections during extreme storms are needed. This could be done by upgrading the SBASs, which currently give thin-shell informations, to broadcast full-height images.

The greatest error appears to be for a location at the edge of the network used for the MIDAS inversion and are probably due to the lower accuracy of the MIDAS images in these areas. It has been found that using a higher receiver density with a larger grid resolution does not give better results. This may be because observations from nearby stations does not give significantly more relevant information. Also, this enlarges the matrices and makes the computation of the inversion so difficult the solution is not more reliable. What would give more relevant information would be to make use of more satellites with different kinds of orbit by including data from GNSSs other than GPS, e.g. GLONASS and, when it will be operational, GALILEO.

The area of the studies was generally under mid-latitude regions of the ionosphere. Future work should be carried out for a region under the equatorial anomaly, where the TEC is much higher and where the thin shell approximation becomes invalid as the ED peak has a height varying from 500 to 250 km in 5° of latitudes.

References

Damien J. Allain. Evaluation of a Set-Up and a Method to Achieve Pseudo-Range 3D Positioning with 3 Emitters. Master's thesis, University of Plymouth, September 2005. 2.1

Damien J. Allain and Cathryn N. Mitchell. Comparison of 4D tomographic mapping vs. thin shell approximation for ionospheric delay corrections for single-frequency GPS receivers over North America. *GPS Solutions*, conditionally accepted, August 2009a. 3.6.2, 4, 7

Damien J. Allain and Cathryn N. Mitchell. Ionospheric delay corrections for single-frequency GPS receivers over Europe using tomographic mapping. *GPS Solutions*, 13(2):141–151, March 2009b. ISSN 1080-5370 (Print) 1521-1886 (Online). doi: 10.1007/s10291-008-0107-y. URL `http://www.springerlink.com/content/7n65681111437377/`. Downloaded 3 Nov 2008. 4, 6

E. S. Andreeva, S. J. Franke, K. C. Yeh, and V. E. Kunitsyn. Some features of the equatorial anomaly revealed by ionospheric tomography. *Geophysical Research Letters*, 27(16):2465–2468, 2000. doi: 10.1029/1999GL003725. URL `http://dx.doi.org/10.1029/1999GL003725`. Downloaded 1 August 2009. 3.1.1, 3.5.2

Marcio Aquino, Fabiano S. Rodrigues, Jock Souter, Terry Moore, Alan Dodson, and Sam Waugh. Ionospheric scintillation and impact on GNSS users in Northern Europe: Results of a 3 year study. *Space Communications*, 20(1-2):17–29, 2005. URL `http://iospress.metapress.com/index/8U0H3Q5JYYJ982YJ.pdf`. Downloaded 20 Jul 2009. 3.5.2

N. Ashby and James J. Spilker. Introduction to relativistic effects on the Global Positioning System. In Bradford W. Parkinson and James J. Spilker, editors, *Global Positioning System: Theory and applications, Vol. 1*, pages 623–697. AIAA, 1995. ISBN 1-56347-106-X. 2.2, 2.2.4, 2.2.5, 4.2.2

N. Balan, Y. Otsuka, T. Tsugawa, S. Miyazaki, T. Ogawa, and K. Shiokawa. Plasmaspheric electron content in the gps ray paths over japan under magnetically quiet conditions at high solar activity. *Earth Planets Space*, 54(1):71–79, 2002. URL `http://www.terrapub.co.jp/journals/EPS/pdf/2002/5401/54010071.pdf`. Downloaded 21 May 2009. 3.1.2

J. Benedicto, S.E.Dinwiddy, G. Gatti, R. Lucas, and M. Lugert. Galileo : Satellite system design and technology developments. *Galileo's World*, December 2000. URL `http://esamultimedia.esa.int/docs/galileo_world_paper_Dec_2000.pdf`. Downloaded 4 Feb 2010. 8.1

Robert F. Benson. Evidence for the stimulation of field-aligned electron density irregularities on a short time scale by ionospheric topside sounders. *Journal of Atmospheric and Solar-Terrestrial Physics*, 59(18): 2281–2293, December 1997. doi: 10.1016/S1364-6826(96)00122-8. URL `http://dx.doi.org/10.1016/S1364-6826(96)00122-8`. Downloaded 18 May 2009. 3.2.2

Dieter Bilitza. IRI 2000. *Radio Science*, 36(2):261–276, 2001. doi: 10.1029/2000RS002432. URL `http://www.agu.org/pubs/crossref/2001/2000RS002432.shtml`. Downloaded 9 May 2008. 3.4.1, 3.5.3

Dieter Bilitza and Bodo W. Reinisch. International Reference Ionosphere 2007: Improvements and new parameters. *Advances in Space Research*, 42(4):599–609, August 2008. doi: 10.1016/j.asr.2007.07.048. URL `http://dx.doi.org/10.1016/j.asr.2007.07.048`. Downloaded 14 Aug 2009. 3.5.3

Michael S. Braasch. Multipath Effects. In Bradford W. Parkinson and James J. Spilker, editors, *Global Positioning System: Theory and applications, Vol. 1*, pages 547–568. AIAA, 1994. ISBN 1-56347-106-X. 2.2, 4.2.1

G. S. Bust and G. Crowley. Tracking of polar cap ionospheric patches using data assimilation. *Journal of Geophysical Research*, 112(A05307), May 2007. doi: 10.1029/2005JA011597. URL `http://dx.doi.org/10.1029/2005JA011597`. Downloaded 12 Aug 2009. 3.4.2

G. S. Bust and Cathryn N. Mitchell. History, current state, and future directions of ionospheric imaging. *Reviews of Geophysics*, 46, February 2008. doi: 10.1029/2006RG000212. URL `http://www.agu.org/pubs/crossref/2008/2006RG000212.shtml`. 3.4.2

G. S. Bust, T. W. Garner, and T. L. Gaussiran II. Ionospheric Data Assimilation Three-Dimensional (IDA3D): A global, multisensor, electron density specification algorithm. *Journal of Geophysical Research*, 109(A11312), November 2004. doi: 10.1029/2003JA010234. URL `http://dx.doi.org/10.1029/2003JA010234`. Downloaded 4 Aug 2009. 3.4.2

G. S. Bust, G. Crowley, T. W. Garner, T. L. Gaussiran, Robert W. Meggs, Cathryn N. Mitchell, Paul S. J. Spencer, Ping Yin, and Bettina Zapfe. Four-dimensional GPS imaging of space weather storms. *Space Weather*, 5, February 2007. doi: 10.1029/2006SW000237. URL `http://www.agu.org/pubs/crossref/2007/2006SW000237.shtml`. 3.1.2, 3.4.2

S. Chapman. The absorption and dissociative or ionizing effect of monochromatic radiation in an atmosphere on a rotating earth. *Proceedings of the Physical Society*, 43(1):26–45, January 1931. doi: 10.1088/0959-5309/43/1/305. URL `http://dx.doi.org/10.1088/0959-5309/43/1/305`. Downloaded 26 May 2009. 3.1.2

K. Choi, K. M. Larso, and P. Axelrad. Modified sidereal filtering: Implications for high-rate GPS positioning. *Geophysical Research Letters*, 2004. doi: 10.1029/2004GL021621. URL `http://www.colorado.edu/engineering/GPS/Papers/2004GL021621.pdf`. Downloaded 16 Aug 2006. 2.2.3

Kenneth Davies. *Ionospheric Radio*. Peter Peregrinus Ltd., 1989. ISBN 0 86341 186 X. 3.2.1, 3.2.1

Richard M. Dear and Cathryn N. Mitchell. GPS interfrequency biases and total electron content errors in ionospheric imaging over Europe. *Radio Science*, 41(RS6007), 2006. doi: 10.1029/2005RS003269. URL `http://dx.doi.org/10.1029/2005RS003269`. Downloaded 4 Aug 2009. 3.2.3

Richard Mark Dear. *Wide Area Forecasting of Total Electron content over Europe*. PhD thesis, University of Bath, 2007. 3.5.4

J. M. Dow, R. E. Neilan, and G. Gendt. The International GPS Service: Celebrating the 10th anniversary and looking to the next decade. *Advances in Space Research*, 36:320–326, 2005. doi: 10.1016/j.asr.2005.05.125. URL `http://linkinghub.elsevier.com/retrieve/pii/S0273117705007684`. 2.2.4

U. Engel. A theoretical performance analysis of the modernized gps signals. In *Position, Location and Navigation Symposium, 2008 IEEE/ION*, pages 1067–1078, May 2008. doi: 10.1109/PLANS.2008.4570114. URL `http://dx.doi.org/10.1109/PLANS.2008.4570114`. Downloaded 2 Feb 2010. 8.1

FAA. *Specification for the WAAS*, August 2001. URL `http://www.faa.gov/about/office_org/headquarters_offices/ato/service_units/tec` Downloaded 25 Mar 2008. 3.5.2

Rafael C. Gonzalez and Richard E. Woods. *Digital image processing*. Prentice-Hall, 2nd edition, 2002. ISBN 0-201-18075-8. 5.2

T. L. Gulyaeva. International standard model of the earth's inosphere and plasmasphere. *Astronomical and Astrophysical Transactions*, 22(4-5):639–643, aug 2003. doi: 10.1080/10556790310001722410. URL `http://images.astronet.ru/pubd/2008/09/29/0001231158/639-643.pdf`. Downloaded 21 May 2009. 3.1.2

Werner Gurtner. *RINEX: The Receiver Independent Exchange Format Version 2.10*, June 2001. URL `http://www.ngs.noaa.gov/CORS/rinex210.txt`. Downloaded 7 Nov 2006. 2.2.5, 3.2.3, 4.3.2

D. A. Hardy, M. S. Gussenhoven, R. Raistrick, and W. J. McNeil. Statistical and functional representations of the pattern of auroral energy flux, number flux, and conductivity. *Journal of Geophysical Research*, 92(A11): 12,275–12,294, November 1987. doi: 10.1029/JA092iA11p12275. URL `http://www.agu.org/journals/ABS/1987/JA092iA11p12275.shtml`. Downloaded 27 May 2009. 3.1.2

John Keith Hargreaves. *The solar-terrestrial environment*. Cambridge University Press, 1992. ISBN 9780521427371. 3.1, 3.2.2

Guenter W. Hein and Thomas Pany. Architecture and signal design of the european satellite navigation system galileo - status dec. 2002. *Journal of Global Positioning Systems*, 1(2):73–84, December 2002. URL `http://forschung.unibw-muenchen.de/berichte/2002/gxvmhzp2xtufymyohtpnufxxdji61` Downloaded 4 Feb 2010. 8.1

ICD 200c. *Interface Control Document (ICD 200c)*, April 2000. URL `http://www.navcen.uscg.gov/pubs/gps/icd200/icd200cw1234.pdf`. Downloaded 29 Sep 2006. 2.2.4, 3.5.1

IGS. IGS Products, Nov 2005. URL `http://igscb.jpl.nasa.gov/components/prods.html`. 2.2.6, 4.3

IS-GPS-200D. *Navstar GPS Interface Specification (IS-GPS-200, Revision D)*, December 2004. URL `http://www.navcen.uscg.gov/gps/geninfo/IS-GPS-200D.pdf`. Downloaded 4 Feb 2010. 8.1

David C. Jefferson and Yoaz E. Bar-Sever. Accuracy and consistency of broadcast GPS ephemeris data. In *ION GPS 2000*, 2000. URL `http://hdl.handle.net/2014/16120`. Downloaded 7 Feb 2007. 4.3

Elliott D Kaplan, J L Leva, and M S Pavloff. Fundamentals of satellite navigation. In Elliott D Kaplan, editor, *Understanding GPS - Principles and applications*, pages 15–57. Artech House, 1996. ISBN 0-89006-793-7. 2.1

Michael C Kelley. *The Earth's Ionosphere: Plasma Physics and Electrodynamics*. Academic Press, Inc, 2nd revised edition, 2007. ISBN 0120884259. 3.1

John A. Klobuchar. Ionospheric effects on GPS. In Bradford W. Parkinson and James J. Spilker, editors, *Global Positioning System: Theory and applications, Vol. 1*, pages 485–515. AIAA, 1996. ISBN 1-56347-106-X. 3.6, 3.2.3

John A. Klobuchar. Ionospheric time-delay algorithm for single-frequency gps users. *IEEE Transactions on Aerospace and Electronic Systems*, AES-23(3):325–331, May 1987. URL `http://ieeexplore.ieee.org/iel5/7/4104338/04104345.pdf`. Downloaded 23 Jul 2007. 3.5, 3.5.1, 6.5, 7.4

A. Komjathy, R. B. Langley, and D. Bilitza. Ingesting GPS-derived TEC data into the International Reference Ionosphere for single frequency radar altimeter ionospheric delay corrections. *Advances in Space Research*, 22(6):793–801, 1998. doi: 10.1016/S0273-1177(98)00100-8. URL `http://gauss.gge.unb.ca/papers.pdf/asrpaper.pdf`. Downloaded 26 Mar 2009. 3.5.3

Attila Komjathy, Lawrence Sparks, Anthony J. Mannucci, and Anthea Coster. The ionospheric impact of the october 2003 storm event on wide area augmentation system. *GPS Solutions*, 9(1):41–50, April 2005. doi: 10.1007/s10291-004-0126-2. URL `http://www.springerlink.com/content/egfft22urdkc3aut/`. Downloaded 27 Oct 2008. 3.5.2

Jan Kouba. *A guide to using International GPS Service (IGS) products*, February 2003. URL `http://igscb.jpl.nasa.gov/igscb/resource/pubs/GuidetoUsingIGSProducts.pdf`. Downloaded 26 Oct 2006. 2.2.4, 2.2.4, 4.3.1

Jan Kouba and Pierre Héroux. Precise Point Positioning Using IGS Orbit and Clock Products. *GPS Solutions*, 5(2):12–28, October 2001. doi: 10.1007/PL00012883. URL `http://www.springerlink.com/content/p910059hq4h618t0/`. Downloaded 17 Dec 2007. 2.2.4, 4.3.1

Joseph L Leva, Maarteen Huijt de Haag, and Karen Van Dyke. Performance of standalone gps. In Elliott D Kaplan, editor, *Understanding GPS - Principles and applications*, pages 237–320. Artech House, 1996. ISBN 0-89006-793-7. 2.1.4, 2.1.4

M. Materassi, C. N. Mitchell, and P. S. J. Spencer. Ionospheric imaging of the northern crest of the Equatorial Anomaly. *Journal of Atmospheric and Solar-Terrestrial Physics*, 65(16–18):1393–1400, November 2003. doi: 10.1016/j.jastp.2003.06.001. URL `http://dx.doi.org/10.1016/j.jastp.2003.06.001`. Downloaded 6 Aug 6 2009. 3.1.1

Robert W. Meggs. *Mapping of ionospheric total electron content using global navigation satellite systems*. PhD thesis, University of Bath, 2005. 3.4

Robert W. Meggs and Cathryn N. Mitchell. A study into the errors in vertical total electron content mapping using gps data. *Radio Science*, 41:RS1008, February 2006. doi: 10.1029/2005RS003308. URL `http://www.agu.org/pubs/crossref/2006/2005RS003308.shtml`. Downloaded 11 Apr 2008. 3.1.2, 3.4.1, 3.5.2, 4.1

Robert W. Meggs, Cathryn N. Mitchell, and V. S. C. Howells. Simultaneous observations of the main trough using GPS imaging and the EISCAT radar. *Annales Geophysicae*, 23(3):753–757, March 2005. URL `http://www.ann-geophys.net/23/753/2005/`. Downloaded 16 Apr 2008. 3.4.2

William Menke. *Geophysical Data Analysis: Discrete Inverse Theory*, volume 45 of *International Geophysics Series*. Academic Press, Inc, revised edition, 1989. 2.1.4, 3.3

Cathryn N. Mitchell and Paul S. J. Spencer. A three dimensional time-dependent algorithm for ionospheric imaging using GPS. *Annals of Geophysics*, 46(4):687–696, August 2003. URL `http://hdl.handle.net/2122/977`. Downloaded 26 May 2009. 3.3, 4.2.2, 6.5

NAVSTAR. *NAVSTAR GPS User Equipment Introduction - public release version*, September 1996. URL `http://www.navcen.uscg.gov/pubs/gps/gpsuser/gpsuser.pdf`. Downloaded 16 Jan 2007. 2.2.6

NPL Time & Frequency Services. *MSF 60 kHz Time and Date Code*, July 2007. URL `http://www.npl.co.uk/upload/pdf/MSF_Time_Date_Code.pdf`. Downloaded 10 Sep 2008. 5.1

R. Orús, M. Hernández-Pajares, J. M. Juan, J. Sanz, and M. García-Fernández. Performance of different TEC models to provide GPS ionospheric corrections. *Journal of Atmospheric and Solar-Terrestrial Physics*, 64(18):2055–2062, December 2002. doi: 10.1016/S1364-6826(02)00224-9. URL `http://dx.doi.org/10.1016/S1364-6826(02)00224-9`. Downloaded 22 Jul 2009. 3.5.3

Bradford W. Parkinson. GPS Error Analysis. In Bradford W. Parkinson and James J. Spilker, editors, *Global Positioning System: Theory and applications, Vol. 1*, pages 469–483. AIAA, 1996. ISBN 1-56347-106-X. 2.1.3

William H. Press, Saul A. Teukolsky, William T. Vetterling, and Brian P. Flannery. *Numerical Recipes In C*. Cambridge University Press, 2nd edition, 1992. ISBN 0 521 43720 2. 3.3, 3.3

S. E. Pryse, L. Kersley, C. N. Mitchell, P. S. J. Spencer, and M. J. Williams. A comparison of reconstruction techniques used in ionospheric tomography.

Radio Science, 33(6):1767–1779, 1998. doi: 10.1029/98RS01613. URL `http://dx.doi.org/10.1029/98RS01613`. Downloaded 6 Aug 2009. 3.4.2

T. D. Raymund, S. E. Pryse, L. Kersley, and J. A. T. Heaton. Tomographic reconstruction of ionospheric electron density with European incoherent scatter radar verification. *Radio Science*, 28(5):811–817, September 1993. doi: 10.1029/93RS01102. URL `http://dx.doi.org/10.1029/93RS01102`. Downloaded 13 Aug 2009. 3.4.2

Bodo W. Reinisch and Dieter Bilitza. Karl Rawer's life and the history of IRI. *Advances in Space Research*, 34(9):1845–1850, 2004. doi: 10.1016/j.asr.2004.09.002. URL `http://dx.doi.org/10.1016/j.asr.2004.09.002`. Downloaded 14 Aug 2009. 3.5.3

H. Rishbeth. Basic physics of the ionosphere: a tutorial review. *Journal of the Institution of Electronic and Radio Engineers*, 58(6 (Supplement)):S207–S223, September 1988. URL `http://cdsagenda5.ictp.trieste.it/askArchive.php?base=agenda\&categ=a02164\&id` Downloaded 16 Nov 2006. 3.1, 3.2

H. Rishbeth and P. J. S. Williams. The eiscat ionospheric radar: The system and its early results. *Quarterly Journal of the Royal Astronomical Society*, 26:478–512, 1985. 3.2.2

Julian A. R. Rose, Damien J. Allain, and Cathryn N. Mitchell. Reduction in the ionospheric error for a single-frequency GPS timing solution using tomography. *Annals of Geophysics*, 52(6):469–486, December 2009. 8.1

Mark Schenewerk. A brief review of basic GPS orbit interpolation strategies. *GPS Solutions*, 6(4):265–267, March 2003. ISSN 1080-5370 (Print) 1521-1886 (Online). doi: 10.1007/s10291-002-0036-0. URL `http://www.springerlink.com/content/vggfy3dcbp6kpdav/`. Downloaded 14 Nov 2006. 4.3.2

Ralf Schmid. URL `http://igscb.jpl.nasa.gov/igscb/station/general/igs05.atx`. Downloaded 19 Dec 2007. 4.3.1

Ralf Schmid, Peter Steigenberger, Gerd Gendt, Maorong Ge, and Markus Rothacher. Generation of a consistent absolute phase-center correction model for gps receiver and satellite antennas. *Journal of Geodesy*, 81(12):781–798, December 2007. ISSN 1432-1394. doi: 10.1007/s00190-007-0148-y. URL `http://www.springerlink.com/content/b311824250v40147/`. Downloaded 14 Feb 2008. 4.3.1

William S. Schreiner, Sergey V. Sokolovskiy, Christian Rocken, and Douglas C. Hunt. Analysis and validation of GPS/MET radio occultation data in the ionosphere. *Radio Science*, 34(4):949–966, 1999. doi: 10.1029/1999RS900034. URL `http://www.agu.org/pubs/crossref/1999/1999RS900034.shtml`. Downloaded 23 Jul 2009. 3.2.1

Dru A. Smith, Eduardo A. Araujo-Pradere, Cliff Minter, and Tim Fuller-Rowell. A comprehensive evaluation of the errors inherent in the use of a two-dimensional shell for modeling the ionosphere. *Radio Science*, 43:RS6008, December 2008. doi: 10.1029/2007RS003769. URL `http://www.agu.org/pubs/crossref/2008/2007RS003769.shtml`. Downloaded 23 Mar 2009. 3.5.2

Space and Missile Systems Center (SMC). Approved lexicon of signal abbreviations. URL `http://www.navcen.uscg.gov/gps/geninfo/gpslexicon.pdf`. Downloaded 19 Mar 2007. 3.2.3

L. Sparks, A. Komjathy, and A.J. Mannucci. Extreme ionospheric storms and their impact on WAAS. In *Ionospheric Effects Symposium 2005*, May 2005. URL `http://hdl.handle.net/2014/37807`. Downloaded 27 Mar 2008. 3.5.2

Paul S. J. Spencer and Cathryn N. Mitchell. Imaging of fast moving electron-density structures in the polar cap. *Annals of Geophysics*, 50(3):427–434, June 2007. ISSN 1593-5213. URL `http://www.earth-prints.org/bitstream/2122/3683/1/10spencer.pdf`. Downloaded 1 Jul 2008. 3.4.2, 4.1, 4.2.2

James J. Spilker. GPS navigation data. In Bradford W. Parkinson and James J. Spilker, editors, *Global Positioning System: Theory and applications, Vol. 1*, pages 121–176. AIAA, 1996. ISBN 1-56347-106-X. 2.2.5

James J. Spilker. Tropospheric effects on GPS. In Bradford W. Parkinson and James J. Spilker, editors, *Global Positioning System: Theory and applications, Vol. 1*, pages 517–546. AIAA, 1994. ISBN 1-56347-106-X. 2.2.1, 2.2.1, 4.2.2

James J. Spilker and Bradford W. Parkinson. Overview of GPS operation and design. In Bradford W. Parkinson and James J. Spilker, editors, *Global Positioning System: Theory and applications, Vol. 1*, pages 29–55. AIAA, 1994. ISBN 1-56347-106-X. 2.2.3, 2.2.3

I. K. Walker, J. A. T. Heaton, L. Kersley, C. N. Mitchell, S. E. Pryse, and M. J. Williams. EISCAT verification in the development of ionospheric tomography. *Annales Geophysicae*, 14(12):1413–1421, March 1996. URL `http://www.ann-geophys.net/14/1413/1996/`. Downloaded 16 Apr 2008. 3.4.2

K. C. Yeh and T. D. Raymund. Limitations of ionospheric imaging by tomography. *Radio Science*, 26(6):1361–1380, 1991. doi: 10.1029/91RS01873. URL `http://dx.doi.org/10.1029/91RS01873`. Downloaded 6 Aug 2009. 3.4.2

K. C. Yeh, S. J. Franke, E. S. Andreeva, and V. E. Kunitsyn. An investigation of motions of the equatorial anomaly crest. *Geophysical Research Letters*, 28(24):4517–4520, 2001. doi: 10.1029/2001GL013897. URL `http://dx.doi.org/10.1029/2001GL013897`. Downloaded 1 August 2009. 3.1.1, 3.5.2

Ping Yin and Cathryn N. Mitchell. Use of radio-occultation data for ionospheric imaging during the April 2002 disturbances. *GPS Solution*, 9(2):156–163, July 2005. doi: 10.1007/s10291-005-0143-9. URL `http://www.springerlink.com/content/xv630931w6670773/`. Downloaded 18 Oct 2006. 3.3, 3.4.2

Ping Yin, C. N. Mitchell, P. S. J. Spencer, and J. C. Foster. Ionospheric electron concentration imaging using GPS over the USA during the storm of July 2000. *Geophysical Research Letters*, 31(L12806), 2004. doi: 10.1029/2004GL019899. URL `http://dx.doi.org/10.1029/2004GL019899`. Downloaded 6 Aug 2009. 3.4.2

Appendix A

Statistics for all test stations

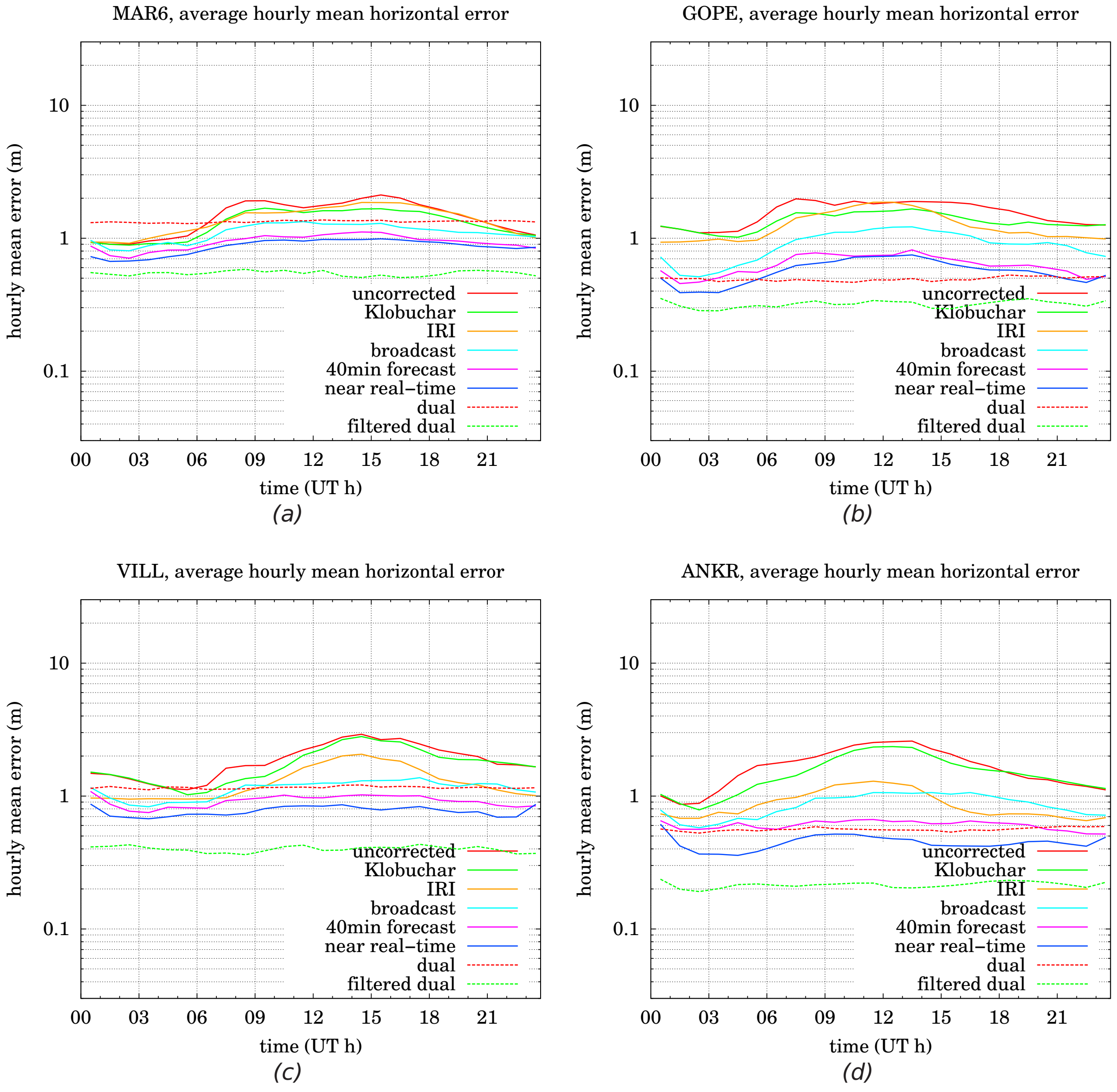

(a) (b)

(c) (d)

Figure A.1: Average absolute horizontal error for Europe stations : MAR6, GOPE, VILL and ANKR

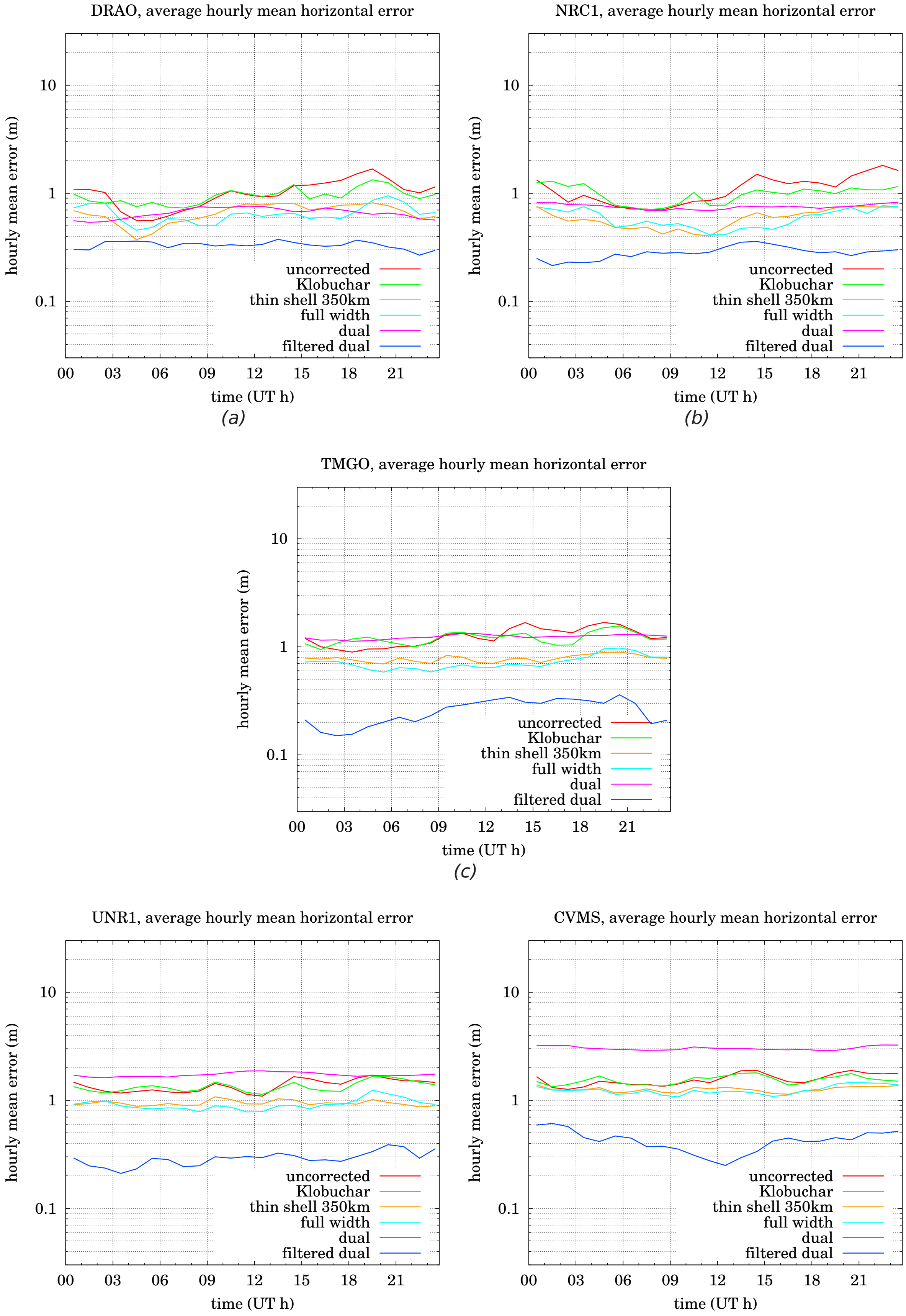

(a) (b) (c) (d) (e)

Figure A.2: Average absolute horizontal error for North America stations : DRAO, NRC1, TMGO, UNR1 and CVMS

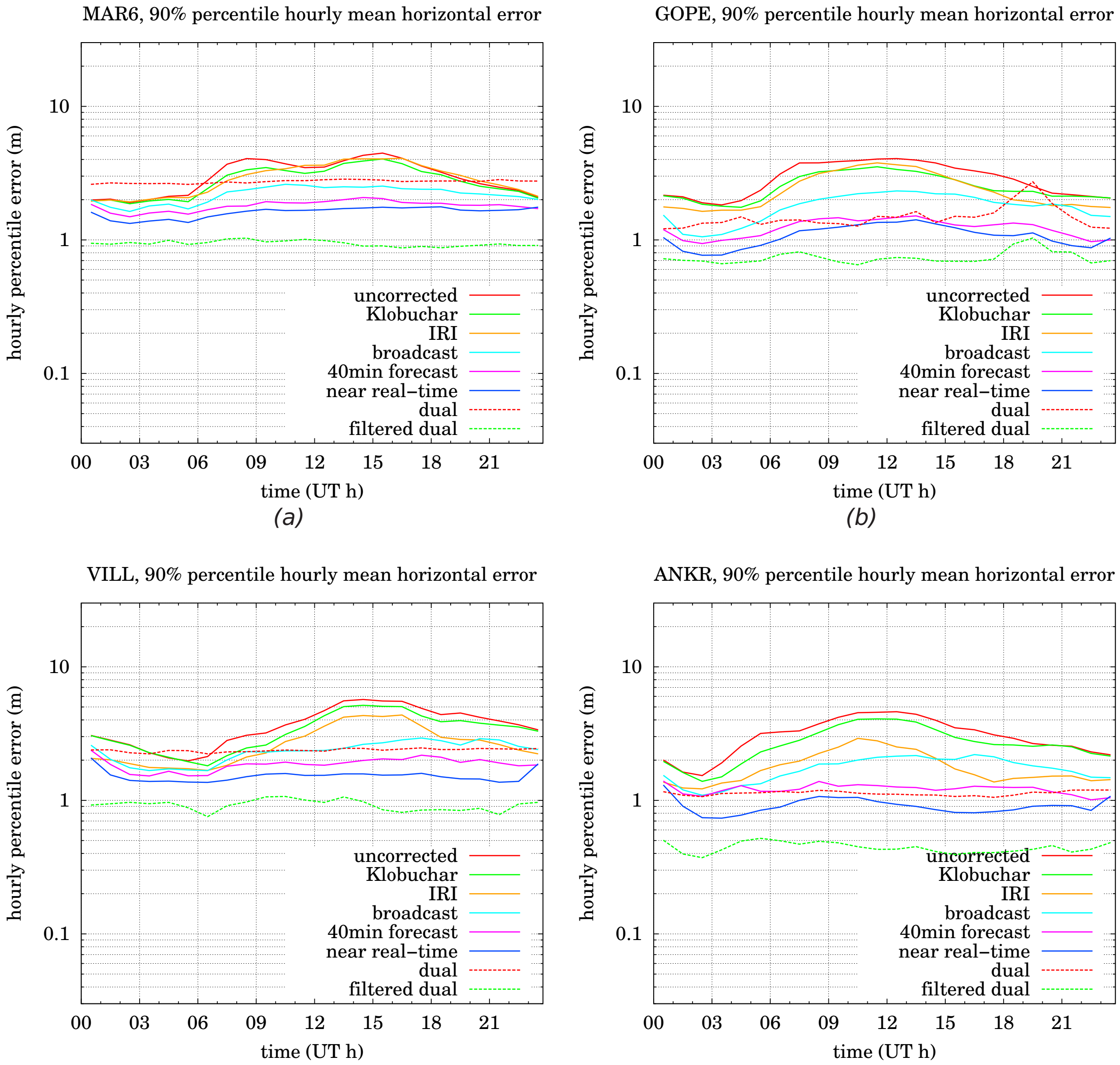

(a) (b) (c) (d)

Figure A.3: 90% percentile absolute horizontal error for Europe stations : MAR6, GOPE, VILL and ANKR

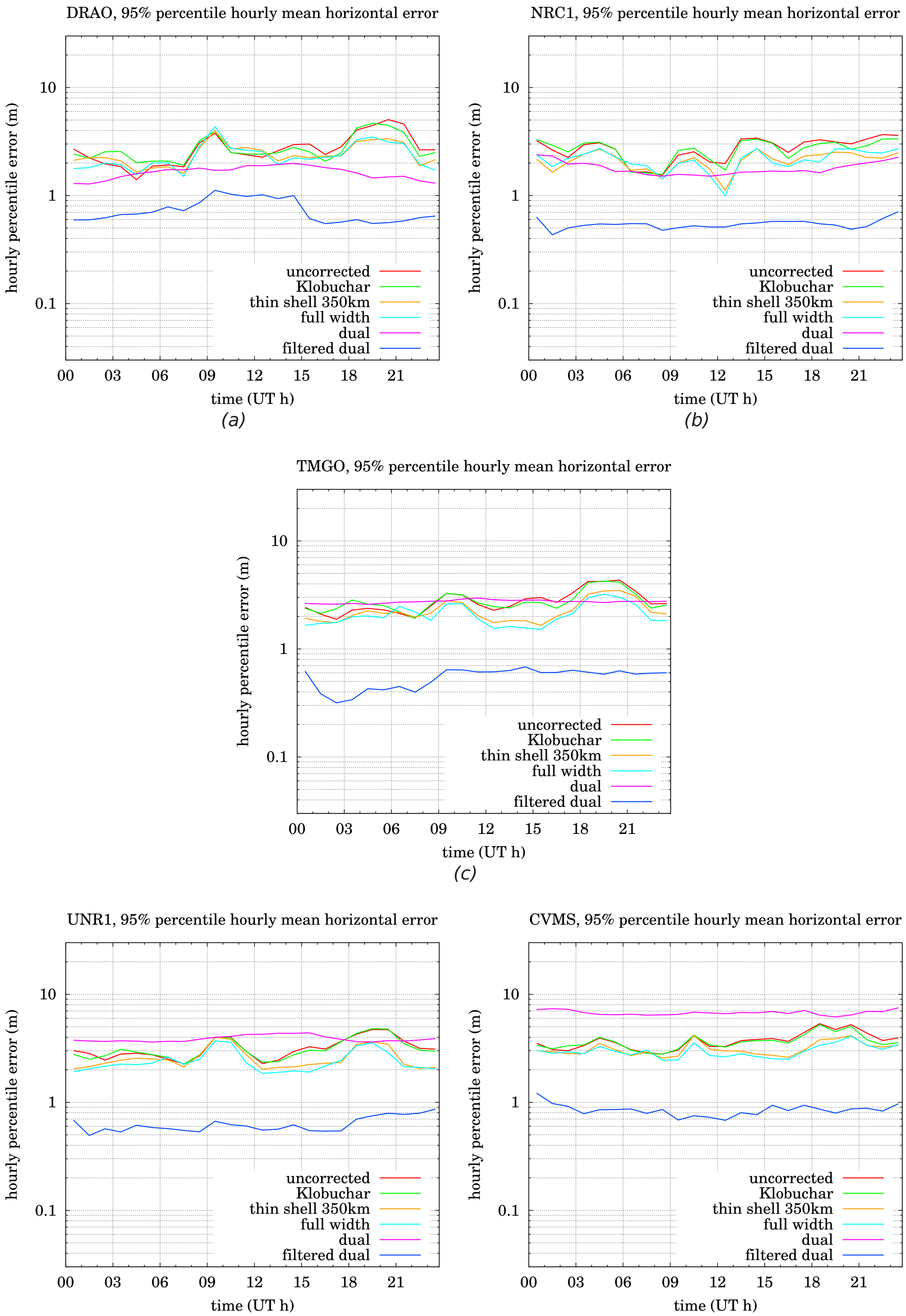

(a)

(b)

(c)

(d)

(e)

Figure A.4: 95% percentile absolute horizontal error for North America stations : DRAO, NRC1, TMGO, UNR1 and CVMS

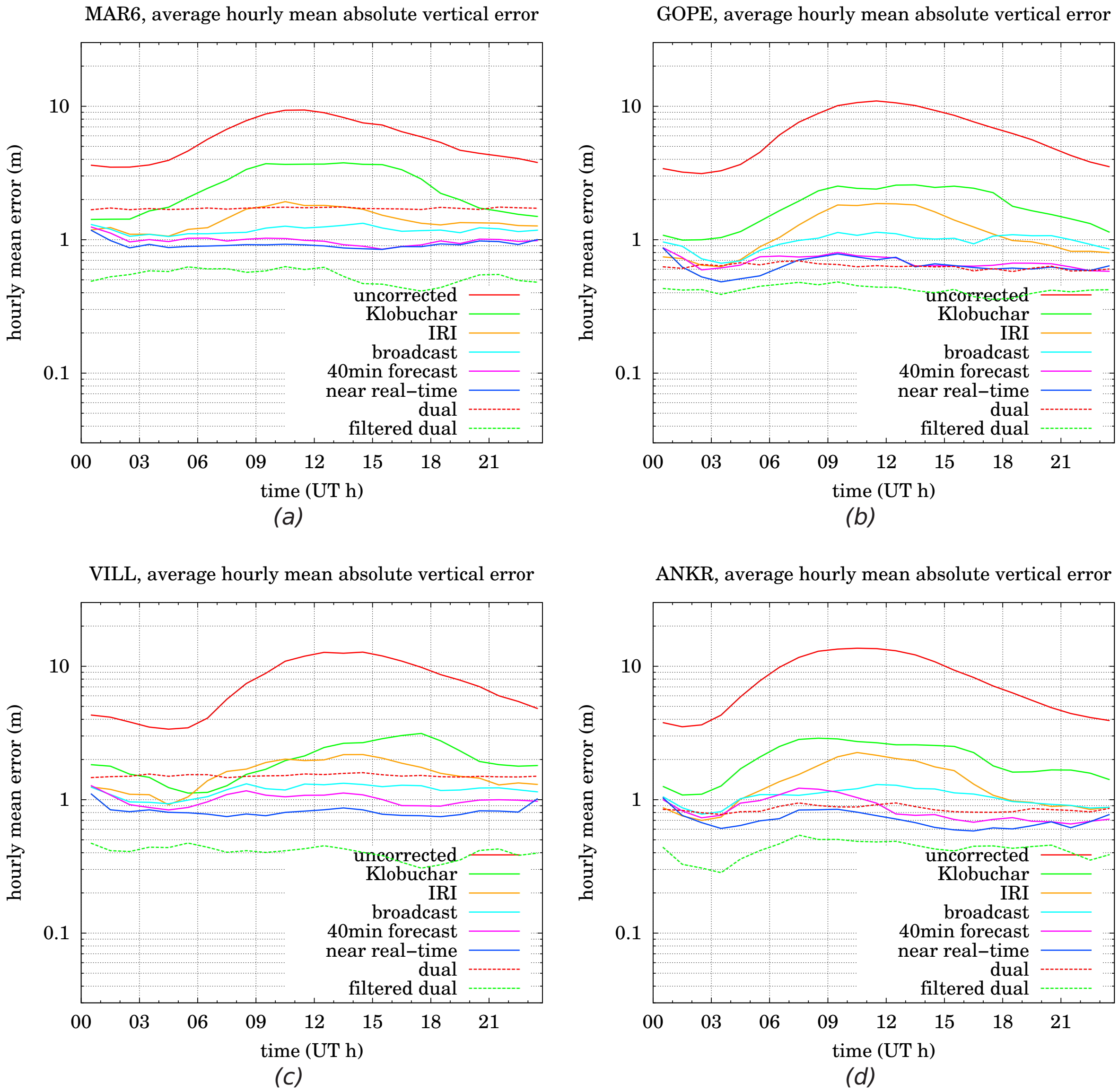
MAR6, average hourly mean absolute vertical error

GOPE, average hourly mean absolute vertical error

VILL, average hourly mean absolute vertical error

ANKR, average hourly mean absolute vertical error

(a) *(b)* *(c)* *(d)*

Figure A.5: Average absolute vertical error for Europe stations : MAR6, GOPE, VILL and ANKR

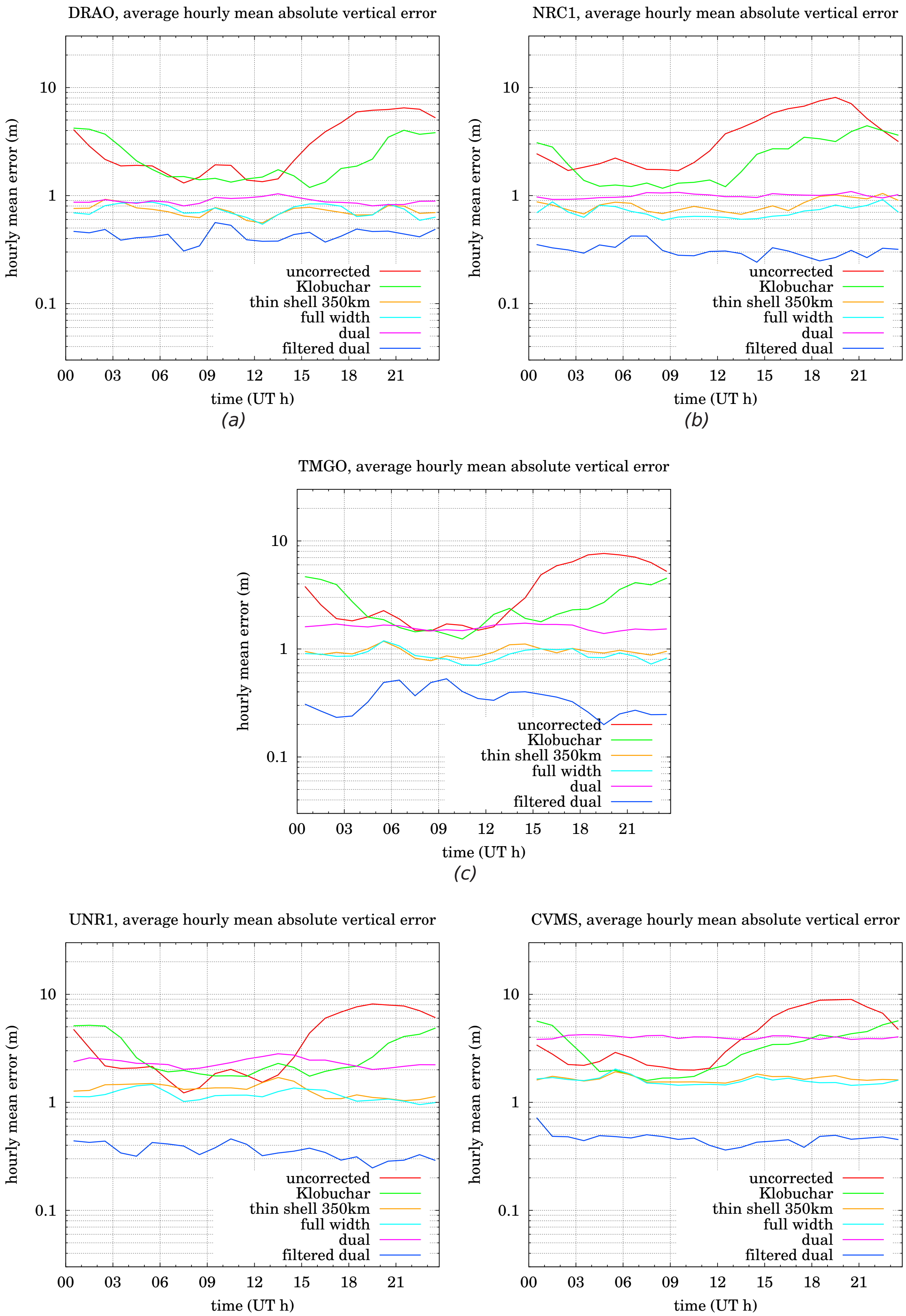

(a) *(b)* *(c)* *(d)* *(e)*

Figure A.6: Average absolute vertical error for North America stations : DRAO, NRC1, TMGO, UNR1 and CVMS

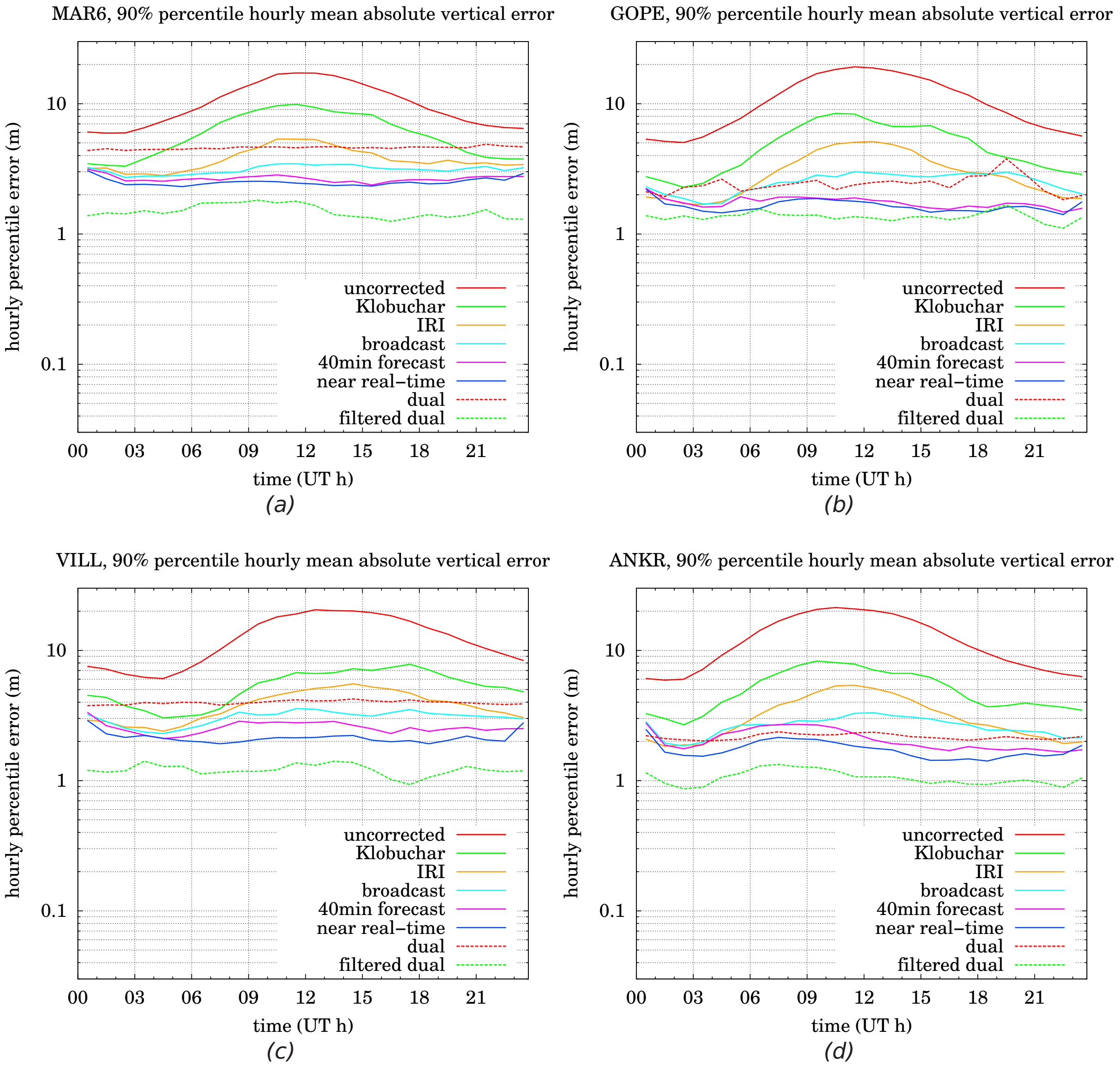
(a) (b) (c) (d)

Figure A.7: 90% percentile absolute vertical error for Europe stations : MAR6, GOPE, VILL and ANKR

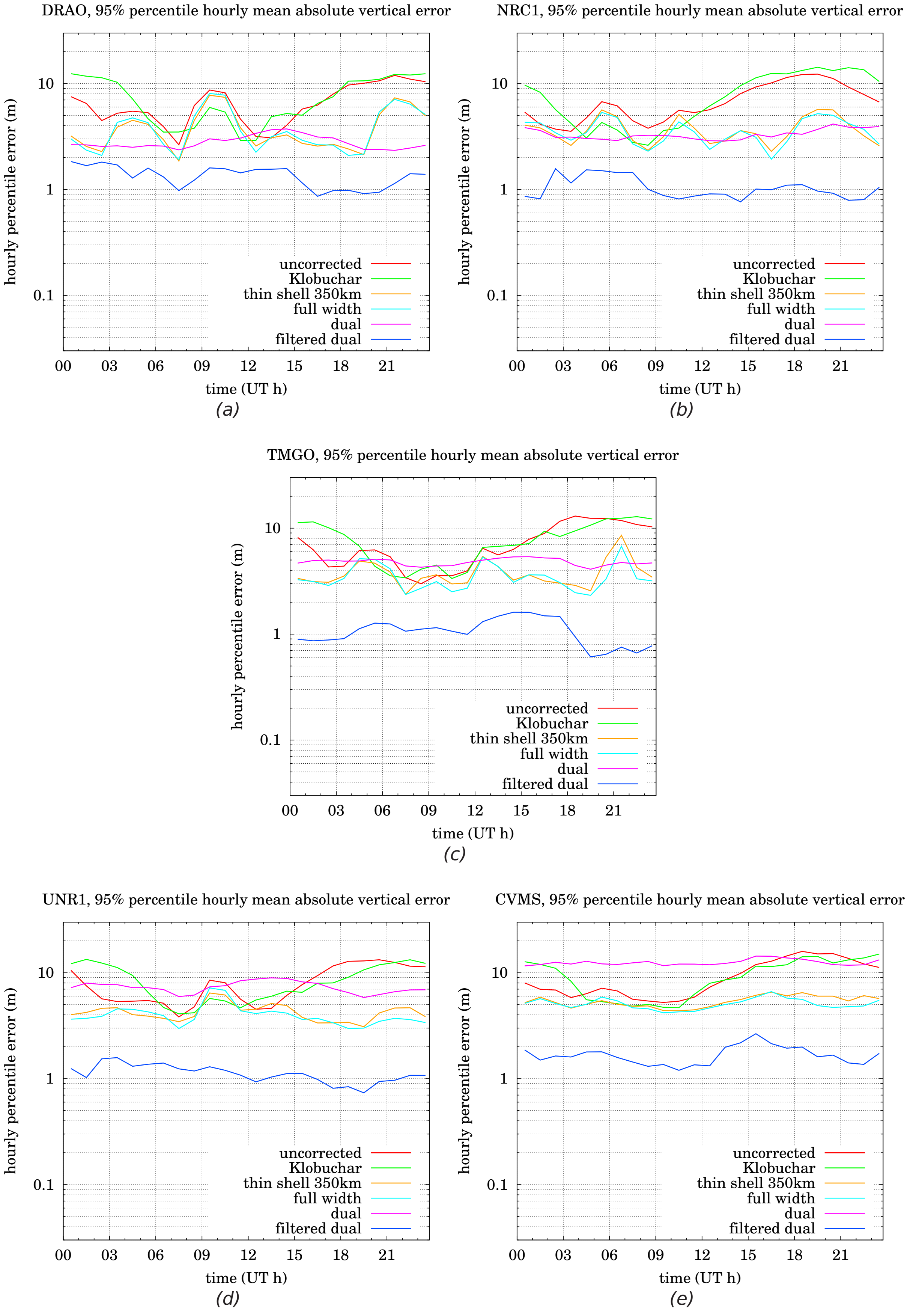

(a) (b) (c) (d) (e)

Figure A.8: 95% percentile absolute vertical error for North America stations : DRAO, NRC1, TMGO, UNR1 and CVMS

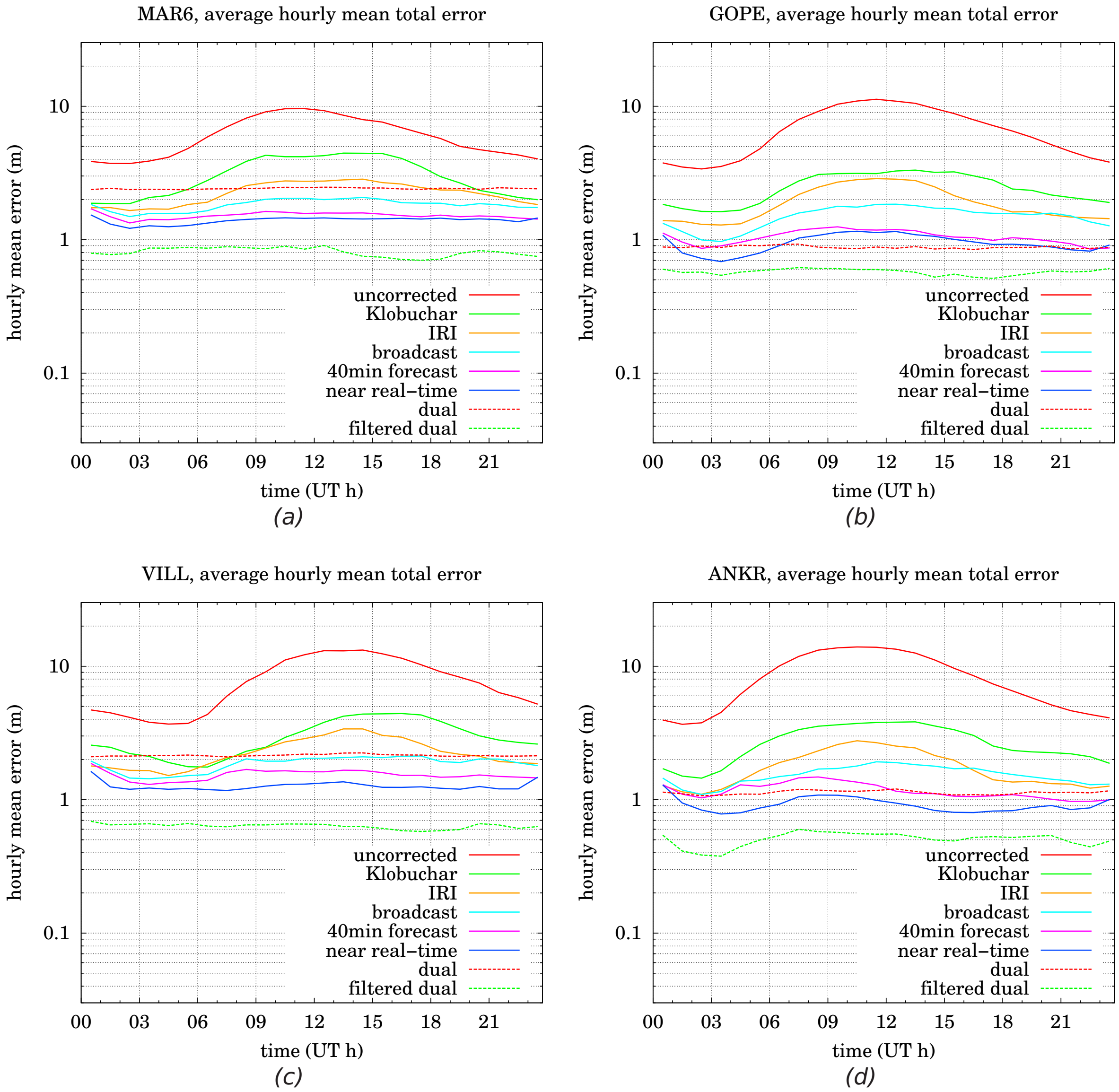

Figure A.9: Average absolute total error for Europe stations : MAR6, GOPE, VILL and ANKR

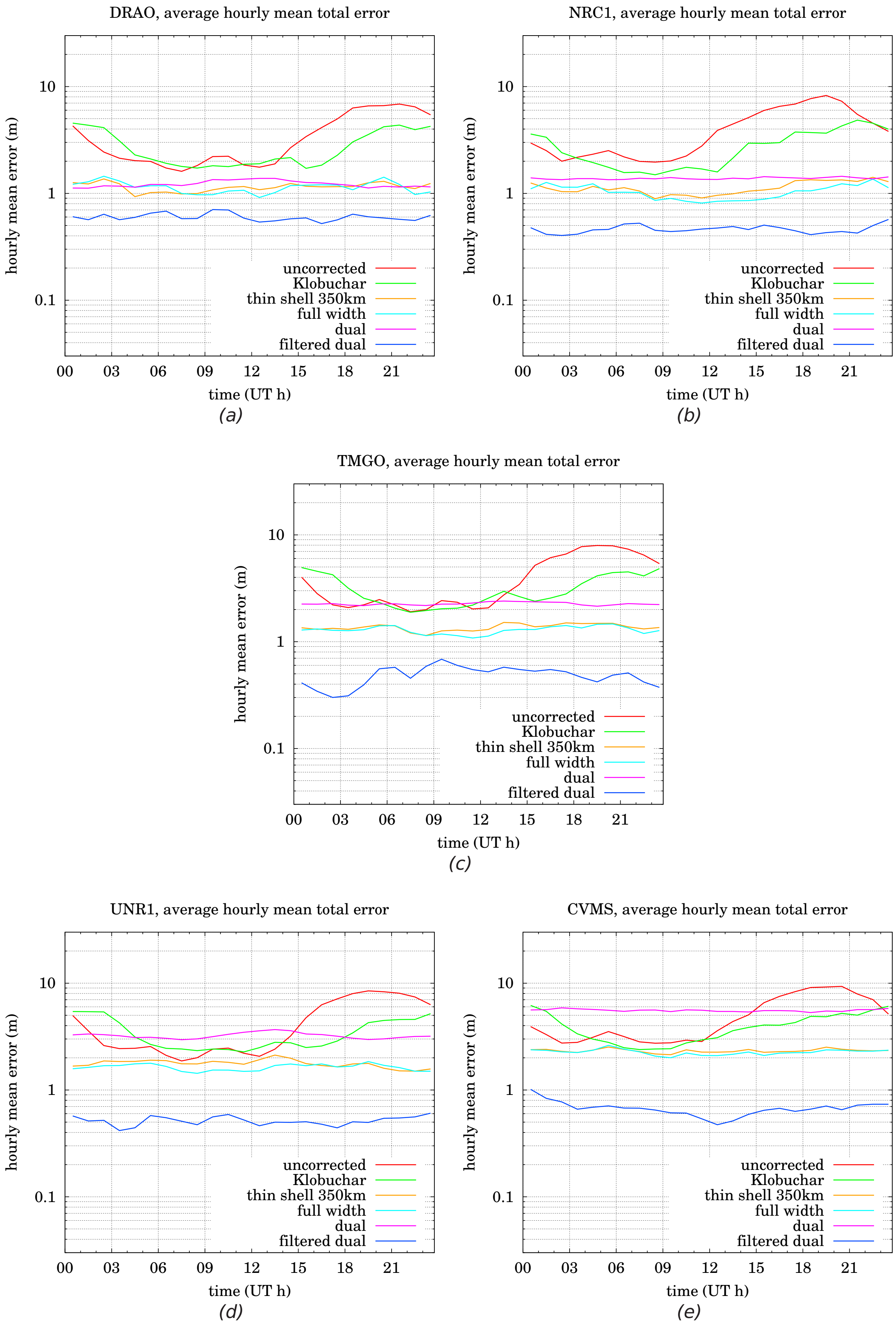

(a) (b) (c) (d) (e)

Figure A.10: Average absolute total error for North America stations : DRAO, NRC1, TMGO, UNR1 and CVMS

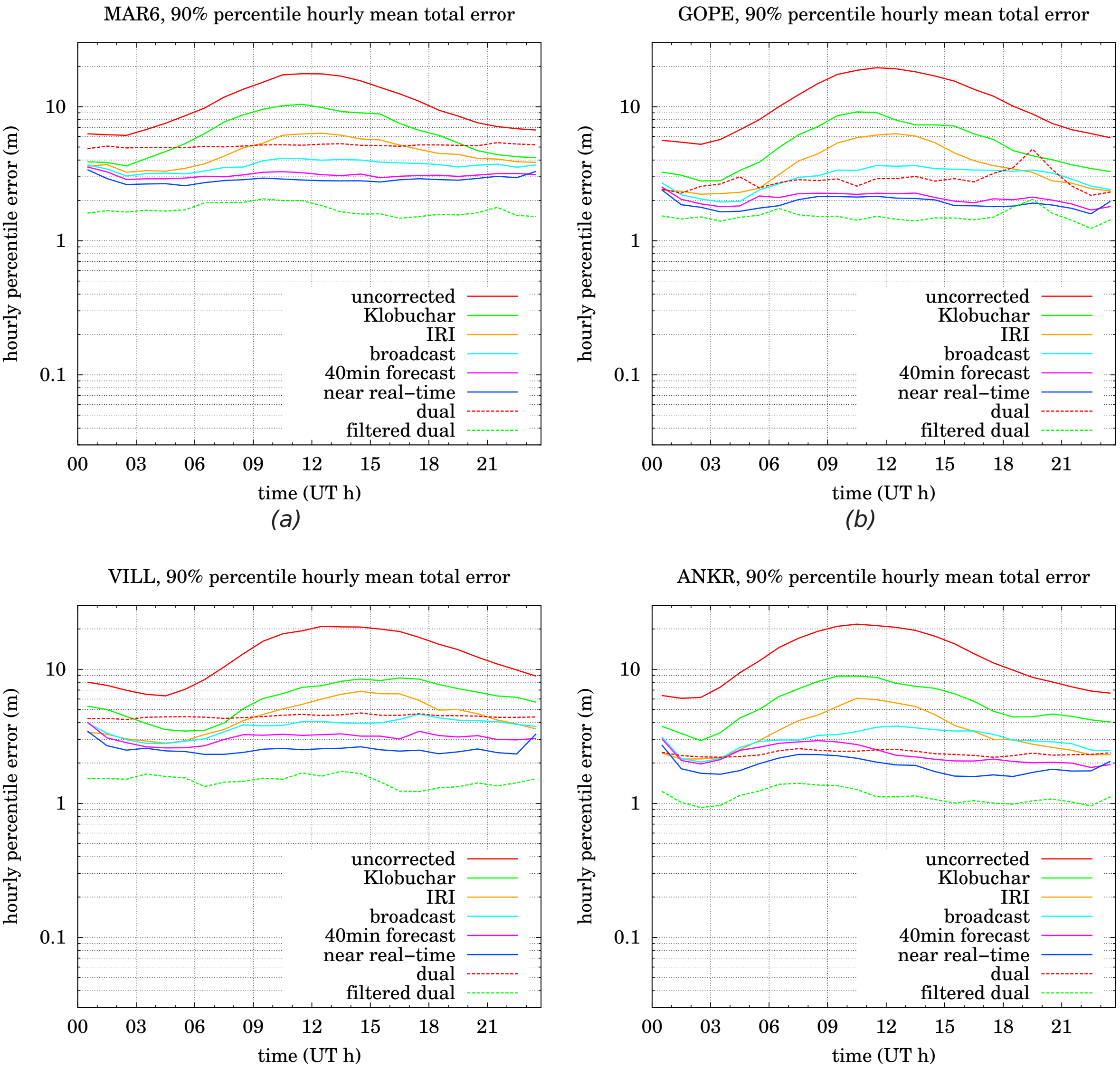

(a) (b) (c) (d)

Figure A.11: 90% percentile absolute total error for Europe stations : MAR6, GOPE, VILL and ANKR

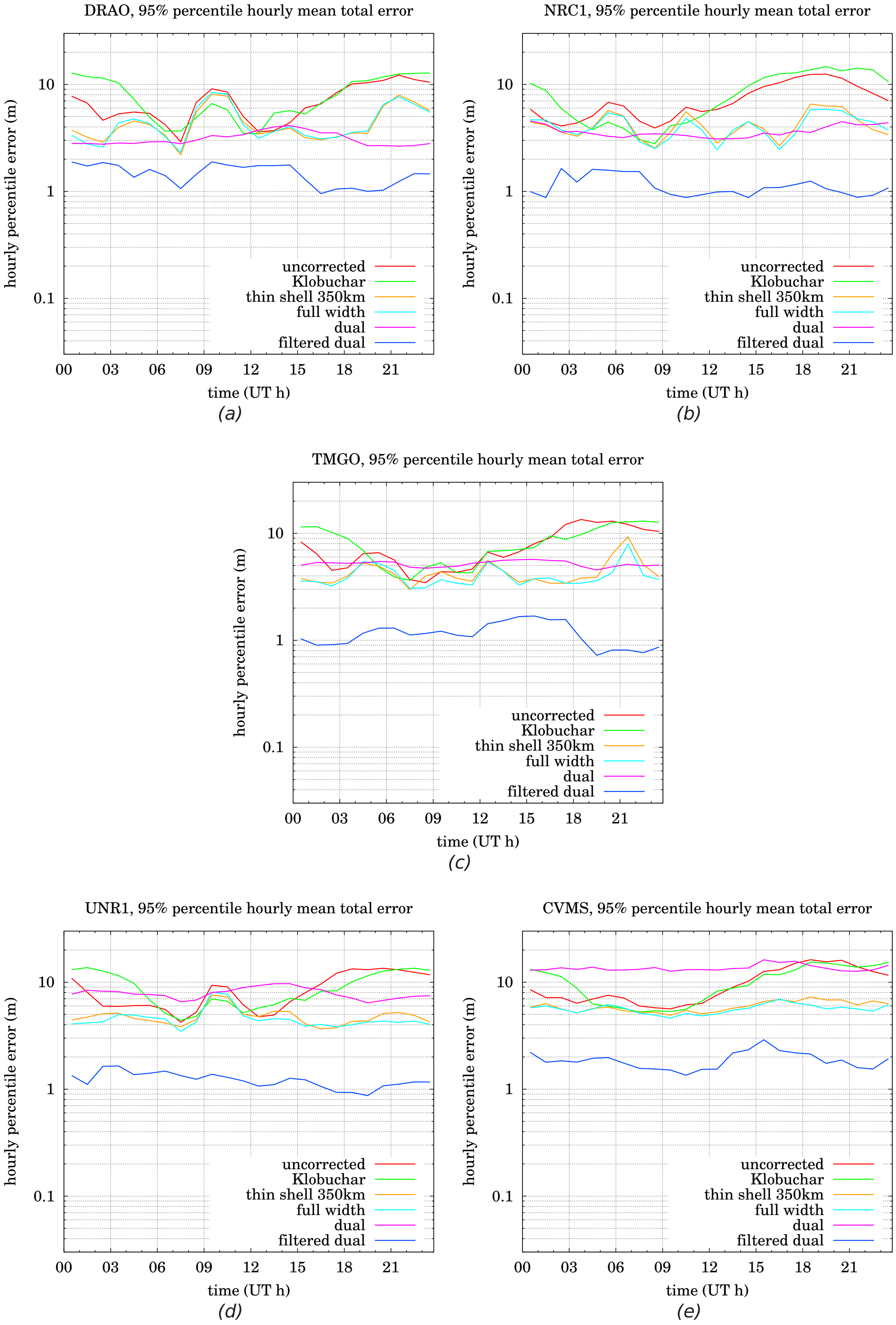

(a) (b) (c) (d) (e)

Figure A.12: 95% percentile absolute total error for North America stations : DRAO, NRC1, TMGO, UNR1 and CVMS

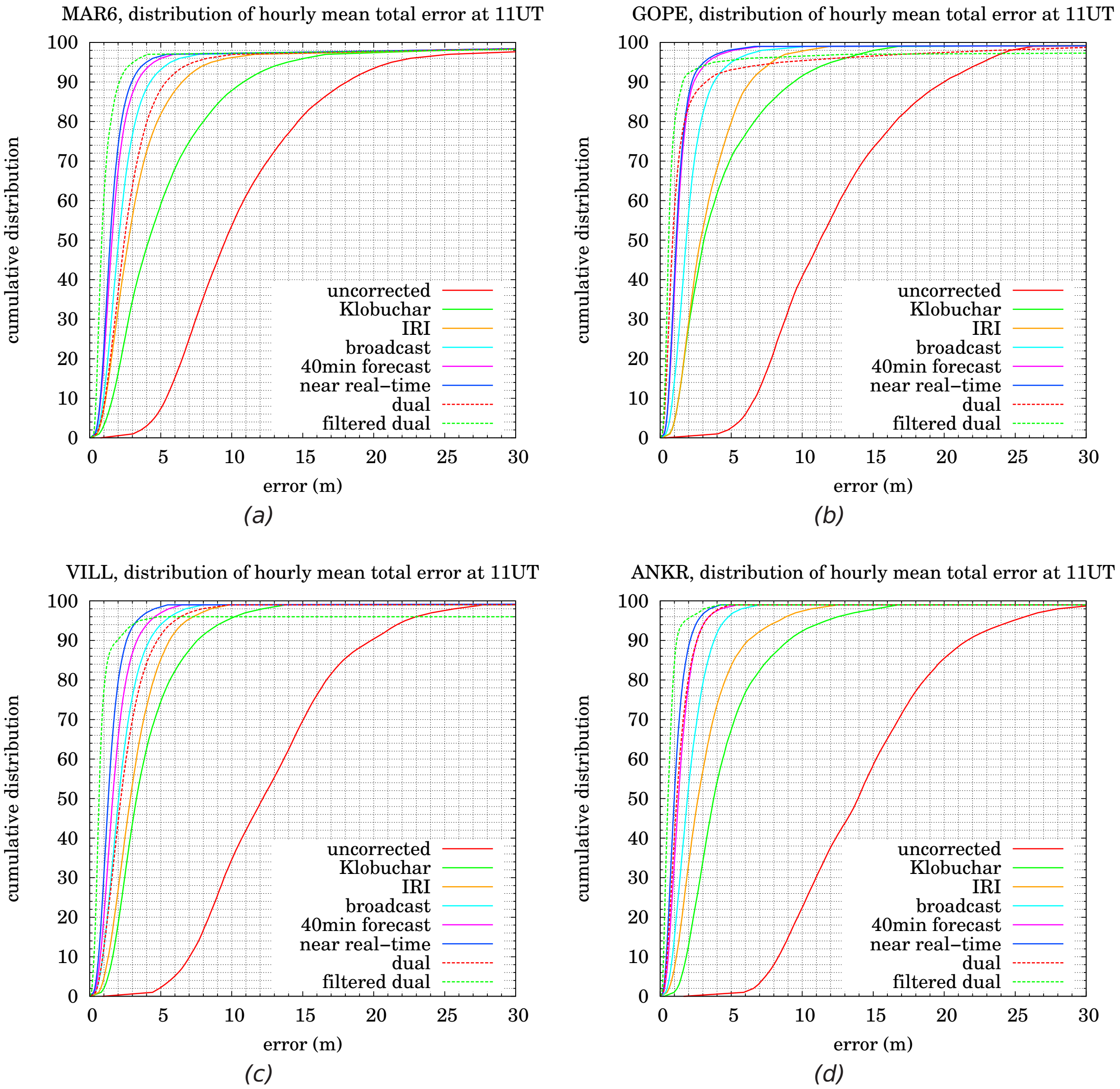

(a)

(b)

(c)

(d)

Figure A.13: Cumulative distribution of total errors for Europe stations at 11UT : MAR6, GOPE, VILL and ANKR

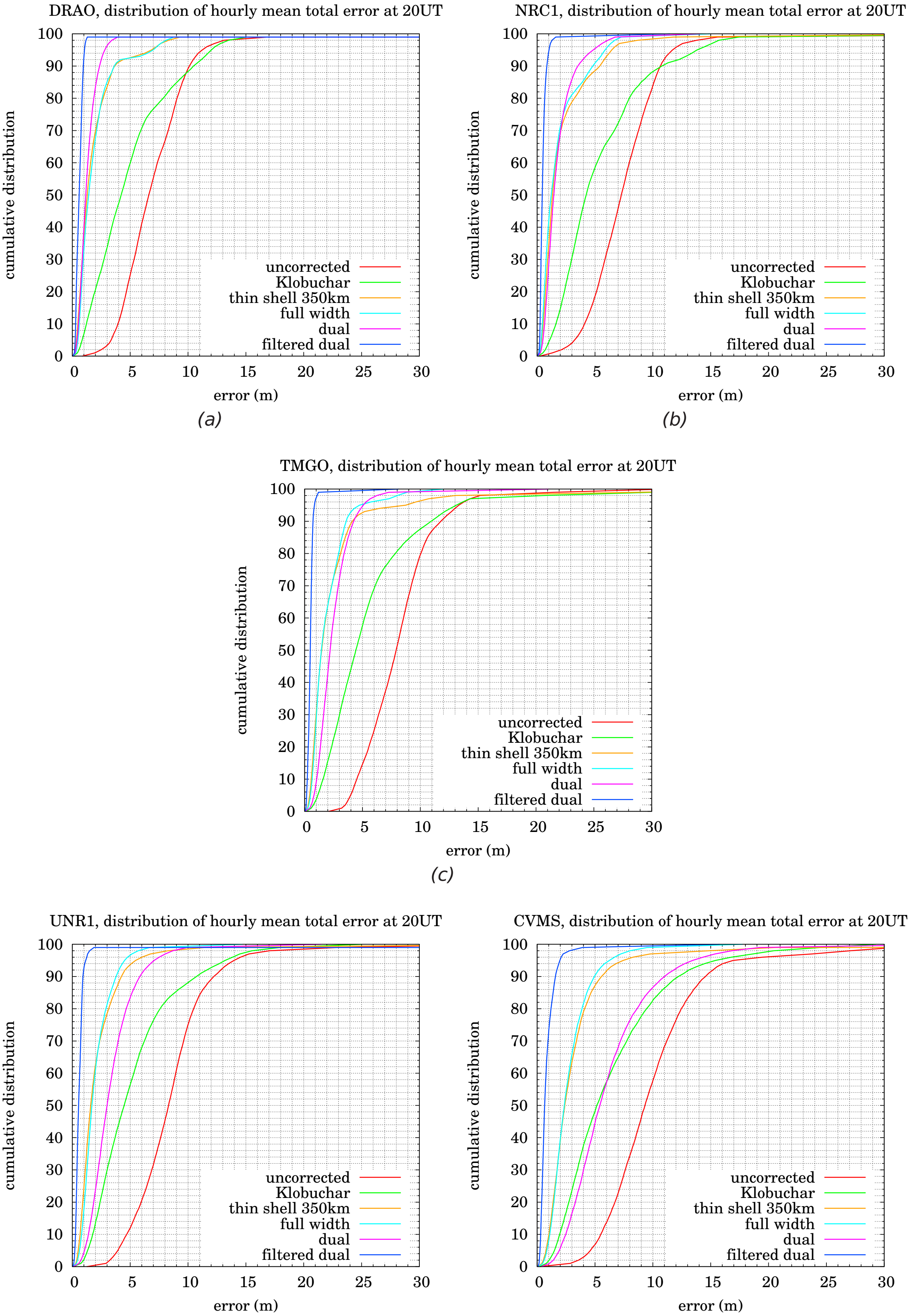

(a) (b) (c) (d) (e)

Figure A.14: Cumulative distribution of total errors for North America stations at 20UT : DRAO, NRC1, TMGO, UNR1 and CVMS